LASER ABLATION-INDUCTIVELY COUPLED PLASMA MASS SPECTROMETRY (LA-ICPMS)- FUNDAMENTAL STUDY OF ABLATION AND DEPOSITION PROCESSES

MERSIDA JANEVA AZDEJKOVIĆ

Doctoral Dissertation
Jožef Stefan International Postgraduate School
Ljubljana, Slovenia, September 2012

Evaluation Board:

doc. dr. Paul McGuiness, Chairman, Jožef Stefan Institute, Ljubljana
prof. dr. Marjan Veber, Member, University of Ljubljana, Ljubljana
dr. Božidar Ogorevc, Member, National Institute of Chemistry, Ljubljana

MEDNARODNA PODIPLOMSKA ŠOLA JOŽEFA STEFANA
JOŽEF STEFAN INTERNATIONAL POSTGRADUATE SCHOOL

Mersida Janeva Azdejković

Laser Ablation−Inductively Coupled Plasma Mass Spectrometry (LA−ICPMS)−Fundamental Study of Ablation and Deposition Processes

Doctoral Dissertation

Laserska ablacija−elementna masna spektrometrija z induktivno sklopljeno plazmo−temeljna raziskava procesov ablacije in depozicije

Doktorska disertacija

Supervisor: Prof. Dr. Spomenka Kobe

Co-Supervisor: Prof. Dr. Alkiviadis Constantinos Cefalas

Co-Supervisor: Dr. Johannes van Teun Elteren

Ljubljana, Slovenia, September 2012

Most important for the scientist are not his diploma or the number of years of his scientific work, not experiences, but quite simply – HIS INTUITION.

Albert Einstein

Najbolj pomembno za znanstvenika niso negova diploma ali število let njegovega znanstvenega dela, niti iskušenj, ampak preprosto – NJEGOVA INTUICIJA.

Albert Einstein

To my son Alexander

Index

Abstract

Laser ablation (LA) is a versatile technique that can be used for the elemental analysis of diverse materials as well as for synthesis purposes, i.e. for pulsed laser deposition (PLD) of a wide range of materials. Analysis and synthesis will only be successful if the ablated material can be stoichiometrically transferred to a detector or a substrate, respectively. Although LA and PLD are conceptually simple techniques, the ablation and deposition processes involved are very complex and not yet completely understood.

The main goal of this thesis is to implement a fundamental study of ablation and deposition processes, i.e. to understand the ejection of the target material in the plume and eventual deposition of the ablated species onto the substrate using two different PLD setups: a commercial laser (213 nm solid state Nd:YAG laser) and a 157 nm molecular F_2 laser. A Fe-Sm-Ta alloy ($Sm_{13.8}Fe_{82.2}Ta_{4.0}$) was used as a target material to study PLD; this material was obtained through induction melting of Fe (13.8 at. %), Sm (82.2 at. %) and Ta (4.0 at. %) via a number of phases ($SmFe_2$, $SmFe_3$, Sm_2Fe_{17}, and $TaFe_2$), each with clearly defined boundaries.

In this study, a 213 nm Nd-YAG commercial laser ablation-inductively coupled plasma mass spectrometer (LA-ICPMS) intended for microanalysis work was used for the first time for PLD under atmospheric pressure and in and ex situ ICPMS analysis for diagnosing the nanoparticle fabrication process. An actual PLD instrument, comprising a 157 nm molecular F_2 laser and a micro-controlled X-Y-Z-Θ translation stage in a 316 stainless-steel chamber was used parallel to this work for fabricating nanoparticles from the same targets. The products obtained at 213 nm were compared with the ones obtained at 157 nm using a suite of characterization techniques (scanning electron microscopy-energy dispersive X-ray spectroscopy [SEM-EDXS], a superconducting quantum interference device [SQUID], X-ray diffractometry [XRD], transmission electron microscopy [TEM] and atomic force microscopy [AFM]).

The results obtained indicate that the PLD diagnostics process indeed led to the fabrication of $Sm_{13.8}Fe_{82.2}Ta_{4.0}$ particles using the commercial LA-ICPMS instrument. In a helium atmosphere, under suitable PLD conditions, more than 95 % [*w*/*w*] of the particles generated had a diameter smaller than 0.75 μm (independently checked via multi-stage cascade impaction of particles leaving the laser ablation chamber) and an (average) stoichiometry indistinguishable from that of the target. Furthermore, element maps of the deposited particles showed that optimal target-substrate geometry (target and substrate positioned at an angle of 45° with respect to the incident beam direction and parallel to each other) can be achieved in a short time (< 1 day) for the appropriate layer density and spatial stoichiometry on a Si/Ta substrate. Detailed SEM-EDXS analysis revealed a deposition pattern which upon close inspection (zooming in) revealed random agglomerates of single spherical particles. In addition to very fine "dust", differently-sized spherical particles (10−50 nm) could also be seen. EDXS analysis proved that oxidation of the Fe-Sm-Ta particles was low and that the average composition of the particles ($N = 10$) reflected that of the target (Fe, 82.6 at. %; Sm, 12.6 at. %; Ta, 4.8 at. %). The Fe/Sm ratio measured in larger particles was, in general, somewhat higher than in the target. This is in accordance with cascade impactor findings for the fractions between 0.41 and 2.8 μm or higher and may be explained by ejection from the melted liquid due to plasma-initiated splashing leading to a melted residue that is rich in lower volatility Fe. The SQUID measurements of the magnetic properties showed that the deposited material, after annealing and thermal treatment in nitrogen, was ferromagnetic.

Experiments at 157 nm were used to unravel the mechanisms related to formation of magnetic nanoparticles from the $Sm_{13.8}Fe_{82.2}Ta_{4.0}$ target. The deposition parameters such as laser fluence and distance between the target and the substrate were optimized to ensure that the particles had the desired crystal structure, composition and ferromagnetic properties. The samples were thoroughly characterized by morphological, structural and magnetic measurements. More reliable information concerning the structural properties of the particles was obtained through high-resolution transmission electron microscopy. TEM images show bi-phase spherical nanodroplets (50−100 nm) consisting of a 5−10 nm crystalline nucleus surrounded by an external amorphous phase. These nanodroplets exhibit a ferromagnetic response with coercivity of 2.5 kOe, which could be further increased to 5.0 kOe through annealing and thermal treatment in nitrogen. The surrounding amorphous shell prevents the post-ablation oxidization of the crystalline magnetic nucleus of the nanodroplet due to oxidization being confined to the surface.

It appears that the commercial 213 nm Nd:YAG LA-ICPMS intended for microanalysis work can be used for PLD under atmospheric pressure and in and ex situ ICPMS analysis for diagnostics of the PLD process. In this way, the size distribution and elemental composition of particles in the plume may be probed in addition to fabricating the elemental density, homogeneity and stoichiometry of the deposited material.

On the other hand, a 157 nm PLD can contribute positively toward improving the properties of magnetic core-shell Sm-Fe-Ta-N nanodroplets. The results presented in this work form a good basis for further studies such as optimization of the PLD process (under atmospheric conditions) for all kinds of novel materials.

Povzetek

Laserska ablacija (LA) je vsestranska metoda, ki jo je mogoče uporabiti za elementno analizo raznovrstnih materialov, poleg tega pa tudi za sintezo, npr. pulzno lasersko depozicijo (PLD) širokega nabora materialov. Analiza in sinteza sta lahko uspešni samo, če je izbiti material mogoče stehiometrično prenesti do detektorja ali substrata. Čeprav sta metodi LA in PLD z vidika zasnove preprosti, sta tovrstna postopka ablacije in depozicije izjemno zapletena ter še vedno ne povsem pojasnjena.

Glavni cilj doktorske disertacije je temeljna raziskava procesov ablacije in depozicije, npr. razumevanje izbrizga ciljnega materiala v plazemskem oblaku in končna depozicija ablativnih zvrsti na substratu z dvema različnima sistema pulzne laserske depozicije: (1) komercialni laser (polprevodniški laser Nd:YAG, valovne dolžine 213 nm) in (2) molekularni laser F_2, valovne dolžine 157 nm. Za preiskavo s pulzno lasersko depozicijo je bila kot ciljni material uporabljena zlitina Fe-Sm-Ta ($Sm_{13.8}Fe_{82.2}Ta_{4.0}$). Ta material je bil pridobljen z indukcijskim taljenjem Fe (13.8 at. %), Sm (82.2 at. %) in Ta (4.0 at. %).

V tem delu, za pulzno lasersko depozicijo pri atmosferskem tlaku in »ex situ« in »in situ« ICP-MS analizo za diagnosticiranje procesa priprave nanodelcev, je bil prvič uporabljen Nd:YAG laser z valovno dolžino 213 nm in elementno masno spektrometrijo z induktivno sklopljeno plazmo. Vzporedno s tem delom je bil za pripravo nanodelcev iz istega ciljnega materiala uporabljen PLD instrument z valovno dolžino 157 nm in mikrokontrolirano X-Y-Z-Θ premikajočo platformo v komori iz nerjavnega železa 316. Produkte, dobljene pri valovni dolžini 213 nm, smo s sklopom naslednjih metod primerjali s tistimi, dobljenimi pri valovni dolžini 157 nm (z uporabo vrstičnega elektronskega mikroskopa z energijsko disperzijskim spektrometrom rentgenskih žarkov [SEM-EDXS], superprevodne kvantne interferenčne naprave [SQUID], rentgenske praškovne difrakcije [XRD], presevne elektronske mikroskopije [TEM] in mikroskopije na atomsko silo [AFM]).

Dobljeni rezultati kažejo, da je diagnostika s pulzno lasersko depozicijo dejansko učinkovita za pridobivanje delcev $Sm_{13.8}Fe_{82.2}Ta_{4.0}$ z aparaturo za lasersko ablacijo in masno spektrometrijo z induktivno sklopljeno plazmo. V helijevi atmosferi, v ustreznih razmerah pulzne laserske depozicije, ima več kot 95 odstotkov [utežni odstotek] nastalih delcev premer, manjši od 0.75 µm (neodvisno preverjeno z obdelavo delcev v večstopenjskem kaskadnem impaktorju, pri čemer delci zapuščajo komoro za lasersko ablacijo), in (povprečno) stehiometrijo, ki je podobna stehiometriji ciljnega materiala. Poleg tega, elementarno vzporejanje naloženih delcev kaže, da je optimalno geometrijo ciljnega materiala in substrata (položaj ciljnega materiala in substrata pod kotom 45° glede na naključno smer snopa in paralelno drug na drugega) mogoče doseči v zelo kratkem času (< 1 dan) ter zagotoviti ustrezno gostoto slojev in stehiometrično razmerje na substratu Ta/Si. Natančna analiza z vrstičnim elektronskim mikroskopom z energijsko disperzijskim spektrometrom rentgenskih žarkov je pokazala vzorec depozicije, ki ob temeljitem pregledu (približanju) pokaže naključno nakopičene posamezne sferične delce. Poleg izjemno finega »prahu« je mogoče opaziti tudi sferične delce različnih velikosti (10–50 nm). Analiza z energijsko disperzivno rentgensko spektrometrijo je pokazala nizko oksidacijo delcev Fe-Sm-Ta in tudi to, da povprečna sestava delcev (N = 10) nakazuje sestavo ciljnega materiala (Fe, 82.6 at. %; Sm, 12.6 at. %; Ta, 4.8 at. %). Razmerje Fe/Sm, izmerjeno pri velikih delcih, je bilo v splošnem nekoliko višje kot v ciljnem materialu. To se ujema z rezultati, pridobljenimi s kaskadnim impaktorjem za delce, velikosti med 0.4 in 2.8 µm ali več, kar je mogoče pojasniti z brizgom taline zaradi plazemsko sproženega brizganja, ki vodi v nastanek staljene usedline, bogate z železom ki ima nižjo hlapnost. Meritve magnetnih lastnosti kažejo, da ima naloženi material po kaljenju in toplotni obdelavi v dušiku feromagnetne lastnosti.

Za pojasnitev mehanizma nastanka magnetnih nanodelcev iz ciljne zlitine $Sm_{13.8}Fe_{82.2}Ta_{4.0}$, so bili uporabljeni preizkusi pri valovni dolžini 157 nm. Parametri depozicije, kot sta fluenca laserja ter razdalja med ciljnim materialom in substratom, so bili optimizirani, da bi imeli delci želeno kristalno strukturo, sestavo in feromagnetne lastnosti. Vzorci so bili temeljito opisani na podlagi morfoloških, strukturnih in magnetnih meritev. Zanesljivejše informacije glede strukturnih lastnosti delcev so bile pridobljene s presevnim elektronskim mikroskopom visoke ločljivosti. Slike, dobljene s presevnim elektronskim mikroskopom, kažejo dvofazne sferične nanokapljice (50–100 nm), sestavljene iz kristalnega jedra z velikostjo 5–10 nm, obdano z zunanjo amorfno fazo. Te nanokapljice kažejo feromagnetni odziv 2.5 kOe,

ki ga je mogoče s kaljenjem in toplotno obdelavo v dušiku dodatno povečati na 5.0 kOe. Okoliška amorfna ovojnica preprečuje oksidacijo kristalnega magnetnega jedra nanokapljice po ablaciji zaradi zamejitve oksidacije na površini.

Pokazali smo da je mogoče LA-ICPMS, ki je predvidena za mikroanalizo, uspešno uporabiti za pulzno lasersko depozicijo pri atmosferskem tlaku in »ex situ« in »in situ« ICP-MS analizo za diagnosticiranje procesa priprave nanodelcev. Na ta način je mogoče temeljito raziskati porazdelitev velikosti in elementarne sestave delcev v ablacijskem oblaku poleg elementarne gostote, homogenosti in stehiometrije dobljenega materiala.

Po drugi strani lahko pulzna laserska depozicija valovne dolžine 157 nm pozitivno prispeva k izboljšanju lastnosti magnetnih nanokapljic Sm-Fe-Ta-N sestavljene iz kristalnega jedra obdano z zunanjo amorfno fazo. Rezultati, predstavljeni v tem delu, omogočajo dobro osnovo za nadaljnje raziskave, kot je optimizacija procesa pulzne laserske depozicije (v atmosferskih razmerah) za vse vrste novih materialov.

Abbreviations

AFM = atomic force microscopy
AM = attritor milling
CI = cascade impactor
CS = core-shell
DC = direct current
EDS = energy dispersive spectroscopy
EDXS = energy dispersive X-ray spectroscopy
EELS = Electron Energy Loss Spectroscopy
FM = ferromagnetic, ferromagnet
FWHM = full width at half-maximum
GB = grain boundary
HRTEM = high-resolution transmission electron microscopy
HT = heat treatment
ICP−MS = inductively coupled plasma-mass spectrometry
INAA = instrumental neutron activation analysis
LA = laser ablation
LA−ICPMS = laser ablation-inductively coupled plasma mass spectrometry
MA = mechanical alloying
PEM = permanent magnet
PLD = pulsed laser deposition
PM = paramagnetic, paramagnet
SCM = superconducting magnet
SEI = secondary-electron image
SEM = scanning electron microscopy/microscope
STEM = scanning transmission electron microscopy/microscope
STEM/HAADF = scanning transmission electron microscopy with high-angle annular dark-field
SQUID = superconducting quantum interference device
VSM = vibrating-sample magnetometer
TEM = transmission electron microscopy/microscope
XPS = X-ray photoelectron spectroscopy
XRD = X-ray diffraction

1 Introduction

Since the invention of lasers in the 1960s, laser ablation has been widely used as a technique for processing materials. The first thin film was deposited in 1965 by Smith and Turner using a ruby laser [1]. The next generation of lasers used for research on laser-material interactions were solid state Nd:YAG (Neodymium-doped Yttrium Aluminum Garnet) lasers. With the development of pulse compression technology [2], solid state lasers with ultra short pulses (picoseconds and femtoseconds) became available and resulted in rapid progress in research and applications of laser-material interactions. Because of the shorter pulse duration, it is possible to generate a high power laser density and when a high-power pulsed laser beam irradiates a target material, melting, vaporization, ejection of atoms, ions, molecular species and plasma formation occur [3]. Laser ablation can be used for direct sampling for microanalysis, micromachining and nano-material fabrication. In other words, laser ablation is a powerful technology with applications in a variety of research areas.

Laser ablation for *microanalysis* requires minimal sample preparation, minimal sample removal and no generation of toxic waste. Hyphenation with inductively coupled plasma mass spectrometry (ICP-MS) can be used for the elemental analysis of solid samples. When the laser irradiates the solid sample, vaporization and removal of the material (atoms, molecules, particles) occurs, which are later transported to the ICP-MS, where ionization in the inductively coupled plasma takes place, followed by elemental analysis in the mass spectrometer. Laser ablation ICP-MS for microanalysis is widely used in numerous fields [4–6] where good precision and accuracy are necessary.

The traditional wet and dry etching methods dictate an expensive direct-write lithographic process, which can be substituted through laser *micromachining*. Almost all materials can be machined with a properly selected wavelength and fluence and by using laser micromachining, enabling a three-dimensional fabrication of microstructures. High-precision, sharp ablation and small thermal diffusion depth with minimal damage can be achieved [7, 8] using lasers with ultra short pulse duration (sub-picoseconds and femtoseconds) because the pulse duration is less than the typical thermal equilibrium characteristic time (a few picoseconds). In recent years, these lasers have been widely used in micromachining because the laser beam does not interact with the laser induced plasma and higher efficiencies of material ablation can be obtained [9].

Nanometer-sized materials (nano particles or nano wires) with new optical, electrical and mechanical properties can be also fabricated using laser ablation. As mentioned above, the laser irradiates the sample and vaporizes atoms from it, which condense into particles, wires or tubes, depending on the fabrication processes required to create these nanometer-sized materials [10]. Understanding the mechanisms and effects of the laser-generated material is crucial to the success of this pulse laser deposition technology.

The fundamentals of laser ablation and deposition processes will be discussed in the first part of this thesis, followed by a section laying out the motivation and objectives behind the choices and approaches taken for the research in this thesis.

1.1 Fundamental processes in PLD

Interest in the theoretical and experimental study of the ablation process has grown since the first high-power lasers became available. However, up until 1986, when high-temperature superconductivity was discovered, laser ablation was mainly used for the analysis of different kinds of materials with research in thin-film deposition progressing slowly. Research in PLD increased dramatically after Wu et al. [11], reported on the superconductivity of materials and soon after that, the first yttrium barium copper oxide (YBCO) film was successfully deposited [12]. In recent years, laser ablation has been the technique of choice for the deposition of a wide range of materials in the form of thin films. The basic idea of the PLD technique is to melt, evaporate and ionize material from the target surface aided by high-power laser pulses (typically ~10^8 Wcm^{-2}) from an excimer or a Nd:YAG laser. The laser energy absorbed in a small volume on the sample surface breaks all chemical bonds of the molecules within that volume and causes species emitting to form high-pressure particles, which after absorbing a significant amount of energy from the laser beam, transform to a plasma plume. The plasma plume expands in the direction normal to the target surface while the ablated particles condense on the substrate surface and form a thin film on this substrate. This PLD process takes place in a chamber where the different deposition parameters can be changed, controlled and optimized for different materials being ablated. One of the most important ablation parameters is laser fluence. If it is high enough the material will evaporate rapidly and transfer stoichiometrically what is essential in the case of a multicomponent target.

The film growth can be optimized by varying the laser parameters. By using the proper combination of deposition parameters, the film will grow epitaxially and with a stoichiometry, replicating that of the target. In order to understand the basic principle of the PLD process, laser-target interactions can be divided into two stages:

1. interaction of the laser beam with the target material resulting in evaporation of the surface layers,
2. interaction of the evaporated material with the incident laser beam resulting in plasma formation and expansion.

1.1.1 Interaction of the laser beam with target material

The mechanism of the laser light interaction with material depends on the laser beam parameters (wavelength, intensity, pulse duration, repetition rate), and the physical (absorption coefficient, melting, vaporization enthalpy) and chemical (composition, microstructure, homogeneity) properties of the material. The heating and melting effects of pulsed laser irradiation on materials are constituted by a three-dimensional heat flow problem, which can be solved in one dimension [13], because in nanosecond laser processing, the absorption length in the target is short (in the order of 10 nm) and is much smaller than the laser beam diameter (typically in the order of 100 μm),

$$\frac{\partial T(x,t)}{\partial t} = \frac{\partial}{\partial x}\left[\left(\frac{k}{\rho c_p}\right)\frac{\partial T(x,t)}{\partial x}\right] + \frac{\alpha}{\rho c_p} I_0(t)[1-R]e^{-\alpha x} \tag{1}$$

where T is the temperature inside the target, t the interacting time and x the direction perpendicular to the plane of the sample. The terms k, ρ, C_p, α and R respectively represent the thermal conductivity, mass density, heat capacity, absorption coefficient and surface reflectivity of the target material. The term I_0 (t) represents the time-dependent incident laser intensity.

In general, the interaction between the laser radiation and solid material begins with the absorption of photons by electrons with the absorbed energy causing electrons to occupy the excited states. The electron-phonon coupling then causes a transfer of the energy from the electron subsystem to the lattice within a few picoseconds. As a result, either the lattice is heated or the interaction leads to the evolution of defects and gradual decomposition of the target surface [14–17]. In the case of ceramics ablated with picosecond pulses, the absorption depth of the material, $1/\alpha$, is larger than the thermal diffusion length, ℓ,

$$\ell = \sqrt{2D\tau} \tag{2}$$

where D is the thermal diffusivity and τ the pulse duration [18]. The situation is reversed for metals with much smaller absorption depths (≈ 10 nm) than the thermal diffusion length and the laser energy is absorbed in a thin surface layer and then transported to a volume whose depth is of the order of one diffusion length. As a result, melting and vaporization take place inside the target and material starts to boil off [14, 19–21].

The transfer of energy to the lattice, in the nanosecond PLD case, occurs on the picoseconds timescale and therefore allows enough time for the target material to heat up to temperatures above its melting and boiling points, causing the formation of a large layer of molten material from which the evaporation of particles takes place. It is assumed that a melted zone exists around the vaporized volume (Figure 1) and that non-congruent ablation is based on fractionated evaporation. On the other hand, the deviation from the correct composition should be proportional to the melt, but not vaporized zone, because the molten surface can contain a composition different from that of the bulk, depending on the thermal and physical properties of the sample. The thermal properties would cause preferential vaporization and a residual melt with a different composition [22]. The melt will remain enriched in the less volatile species until either the more volatile components are lost or a congruently evaporating liquid mixture is reached. This process depends on the presence of a diffusive equilibrium in both the liquid and the vapour. If the liquid/vapour interface is rapid enough, only a surface layer of the liquid is depleted and soon congruent vaporization is achieved. If the melt consists predominantly of more volatile species, the less volatile ones will be dragged along. In the reversed case, the more volatile species are trapped by the less volatile ones. In the absence of a diffusive equilibrium, the vapour composition approaches the composition of the liquid [22].

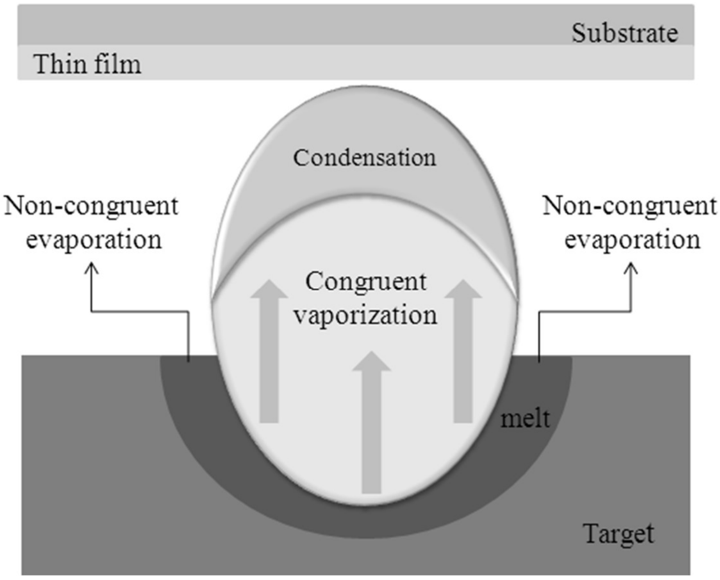

Figure 1: Congruent vaporization and non-congruent evaporation in the PLD process.

A sequence of events takes place which may lead to elemental fractionation due to (a) formation of non-stoichiometric aerosol particles, (b) selective particle transport phenomena as a result of diffusion, gravitational settling and inertial deposition and (c) incomplete atomization of particles as a result of particle size distribution [23]. When a target is ablated, material gets heated far above the melting and boiling point and evaporates into the surrounding atmosphere. Small aerosol particles with a size up to 100 nm can be produced by gas-to-particle conversion processes such as nucleation and condensation followed by coarsening due to the particle collision and coalescence causing the total number of particles to reduce and the average size to increase [24]. Additionally, a certain amount of material remains melted and may act as a source for larger particles produced by hydrodynamic sputtering, a sort of plasma-initiated splashing [25]. Fractionated evaporation causes an enrichment of the more volatile components in the condensable vapour phase and a depletion in the mechanically removed droplets from the melt.

Fractionation appears on the outside of the melted zone and congruent vaporization in the centre of the laser-produced crater. The total mass removed from the sample can be subdivided into the congruent vaporized part, evaporated without fractionation, and the non-congruent evaporated part, evaporated from the edge of the crater.

When the particles are formed from the vapour species (congruent vaporization) their composition is identical to the target composition and when the particles are formed from the nucleation and growth of the evaporants (non-congruent evaporation), they are enriched in the elements with lower volatility. The composition of the particles formed from vapour species is independent of their size. The situation is totally different when the particles are formed from the expelled liquid droplets. Here the laser fluence is much higher and the elements with lower melting temperatures (higher volatility) among the constituent elements in the liquid droplets are lost during transport from the target to the substrate, resulting in the deposition of particles enriched in the elements with higher melting temperatures (lower volatility). In this case, the composition of particles depends on their size, since the larger liquid droplets have a greater loss of elements with higher volatility than the smaller droplets.

However, a high fluence can result in the ejection of droplets or large particles from the target while an excessively high fluence may lead to the sputtering of unwanted debris from the target.

1.1.2 Interaction of the evaporated material with the incident laser beam - plasma formation and expansion

Laser plasma plumes are the focus of intensive research as their formation is still not completely understood. The ablation process results in the formation of a reaction zone in the ablated material, consisting of an energetic plasma, gas and solid debris mixture. The target surface begins to vaporize after approximately 100 ps and the material under the evaporated cloud becomes screened off from the rest of the laser energy, which is absorbed from the ejected material so that there is little or no thermal damage to the surrounding target material. The absorption of the laser energy by the plasma reduces its efficiency onto the sample and increases the plume ionization degree. The absorption of the laser light by the plasma depends on the electron-ion density, temperature and laser wavelength. The primary absorption mechanism for the plasma is the electron-ion collisions. The absorption process involves absorption of a photon by a free electron. The absorption coefficient α_p of the plasma is given by [18],

$$\alpha_p = 3.69 * 10^8 \left(\frac{z^3 n_i^2}{T^{0.5}\,\nu^3}\right)\left[1 - e^{-\frac{h\nu}{kT}}\right] \tag{3}$$

where z, ni and T are the average charge, ion density and temperature of the plasma, respectively; h, k, and ν are the Planck's constant, Boltzmann's constant and frequency of the laser light, respectively.

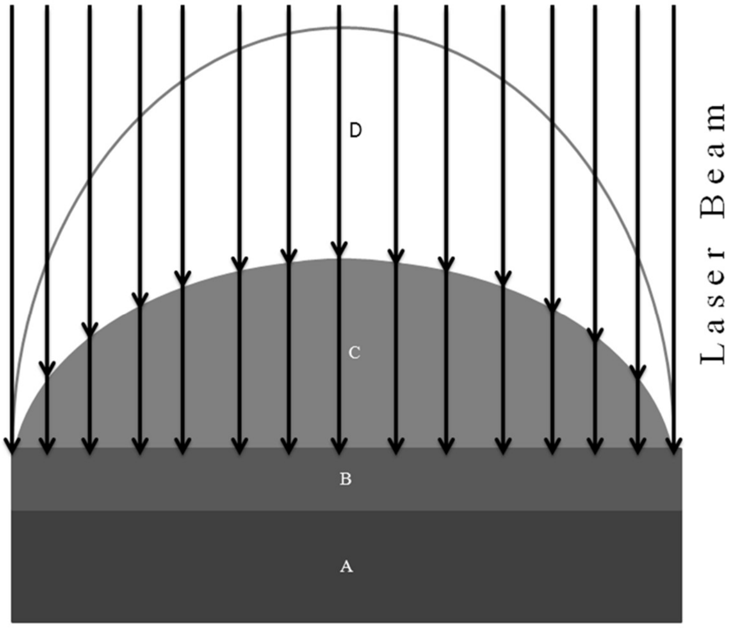

Figure 2: The different phases present during irradiation of a laser on a bulk target: (A) unaffected bulk target, (B) evaporated target materials, (C) dense plasma absorbing the laser radiation, and (D) expanding plasma transparent to the laser beam [18].

The particle density in the plasma depends on the degree of ionization, evaporation rate and plasma expansion velocity [18]. Because the plasma has a very high expansion velocity, the electron and ion densities decrease very rapidly with time. This makes the plasma transparent to the laser beam for distances farther away from the target surface (Figure 2, region D). In the region close to the target surface (Figure 2, region C), the laser radiation is absorbed by the plasma due to the constant growth of the plasma with evaporated particles. In its early stage, the plasma expands strongly in the direction normal to the ablated target due to the difference in pressure gradients in axial and radial directions. This difference in pressure gradients causes expansion of the plasma in the maximum pressure gradient direction (normal to the target).

The plasma plume created thus expands in a vacuum or an ambient atmosphere before condensing on a suitable substrate (in the case of material deposition).

In a vacuum, the rapid plasma expansion results from the large density gradients [18, 26]. The velocity, density and pressure profiles in the plasma are shown schematically in Figure 3. The plasma density and pressure gradients monotonically decrease from the target surface while the velocity increases linearly [18]. In the initial stages of expansion, the acceleration is very high when the expansion velocities are low. When the expansion velocities increase, the acceleration begins to diminish and ultimately becomes zero, resulting in the elongated plasma shape. In the case of expansion into an ambient atmosphere, the plume compresses the background gas during its expansion, resulting in a hemispherical plume shape. Both pressure and temperature fall in the case of a rapid expansion of the plume, carrying the system into a supersaturated state.

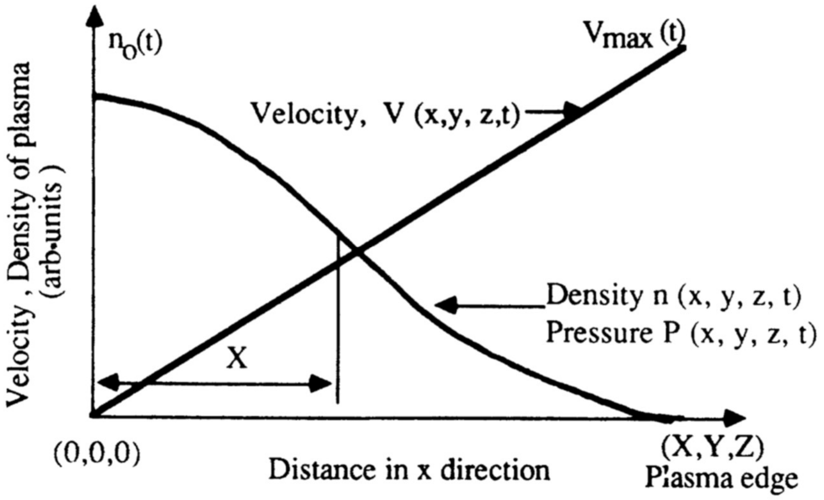

Figure 3: Schematic profile showing the density (n), pressure (P) and velocity (V) gradients in the plasma in the x direction, perpendicular to the target surface [18].

1.2 Thin film fabrication by PLD

In contrast to its conceptual technical simplicity, pulsed laser deposition (PLD) is very complex from a physical-chemical point of view. PLD offers several advantages over other deposition techniques, e.g., preservation of stoichiometry, film homogeneity and high-quality crystalline structure of the deposited films. The good structural quality is attributed to the large kinetic energy of the ablated atoms and molecules upon arrival at the substrate surface [27]. The efficiency of nanocrystallization of the films depends on the local thermodynamic conditions and thus, on the properties of the laser beam (wavelength, energy, intensity, etc.), deposition geometry, type and purity of the initial target and substrate. Furthermore, the laser ablation process is strongly affected by the ambient conditions such as temperature, background pressure and gas composition.

In PLD, the deposition of the ablated material on the substrate begins immediately after formation of the collision region which is established between the incident high-energy species ejected from the target and sputtered atoms from the substrate surface. This collision or thermalised region behaves as a source for condensation of particles. When the condensation rate is higher than the sputtering rate, thermal equilibrium condition can be reached quickly and the film grows on the substrate surface directly from the flow of ablation particles. The two main thermodynamic parameters for the growth mechanism are the substrate temperature T and supersaturation $\Delta\mu$, which can be related by the following equation [28],

$$\Delta\mu = k_B T \ln\frac{R}{R_0} \tag{4}$$

where k_B is the Boltzmann constant, R the actual deposition rate and R_0 the equilibrium value at temperature T. The high supersaturation of the vapour leads to a large nucleation rate. When a system becomes supersaturated, the molecular clusters increase in concentration and reach a critical size d_c,

$$d_c = \frac{\sigma V_m}{k_B T \ln\frac{p}{p_{s_c}}} \tag{5}$$

where $\frac{p}{p_{s_c}}$ is the ratio of the partial pressure of the condensable vapour to the saturation vapour pressure at the local temperature T, σ the surface tension and V_m the molecular volume of the material composing the particle [23].

When the critical size is reached, the system becomes stable and exhibits a tendency for further growth into liquid droplets. The stable nuclei are generated by the homogenous nucleation or self-nucleation process [23, 25] and its formation relieves the super saturation in the gas. The small super saturation is characterized by the large nuclei, which create islands of film on the substrates which subsequently grow and coalesce. If the super saturation increases, the critical nucleus size decreases and a two-dimensional layer will be formed. Layer-by-layer nucleation will occur in the event of large supersaturation.

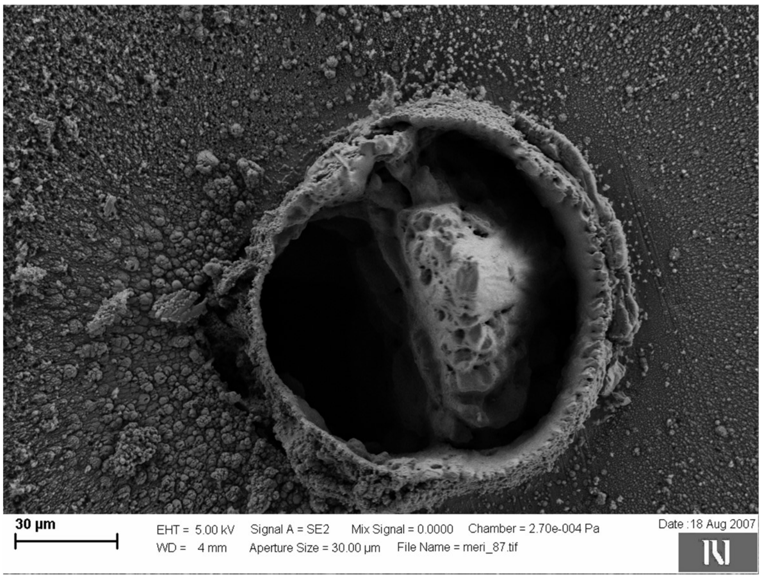

Figure 4: Splashing patterns on a $Sm_{13.8}Fe_{82.2}Ta_{4.0}$ target.

If the critical nuclei have the size of a single molecule, particle formation will take place via the coagulation process, which modifies the size distribution of the particles, i.e. particle collision and coagulation lead to a reduction in the total number of particles and an increase in the average size [24]. By increasing the average size, the time to reach the solidification temperature decreases and smaller particles will stay liquid for longer periods with a tendency to coalesce and form agglomerates [29].

It was shown that coalescence is not the cause of the larger particle fraction and that the "splashing" pattern around the laser crater (Figure 4) indicates the melt layer as the reason for large particles [23]. To avoid these particles, the thickness of the liquid layer must be minimized. This can be achieved if absorption is high and the laser energy larger than heat diffusion losses into material around the laser spot. This results in high evaporation rates and a thin melt layer [23].

1.2.1 Film growth modes

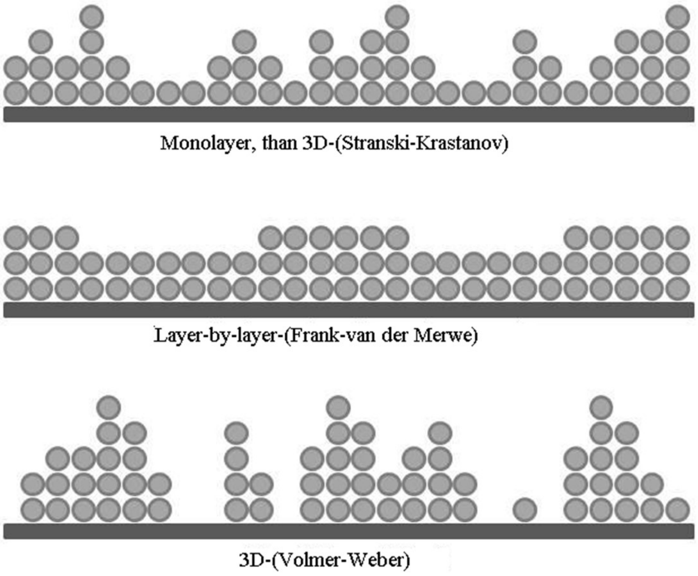

Figure 5: Various growth modes at surfaces, depending on the surface and interface energies.

The nucleation and growth processes mentioned above can also be classified into three different modes: (i) three-dimensional island or Volmer-Weber growth, (ii) two-dimensional layer-by-layer or Frank-van der Merwe growth and (iii) two-dimensional growth of monolayers followed by nucleation and growth of three-dimensional islands or Stranski-Krastranov growth [30]. The previous regimes are shown in the Figure 5.

1.2.1.1 Volmer-Weber nucleation and growth

The nucleation of clusters due to the deposition of atoms on a substrate involves several processes as illustrated in Figure 6.

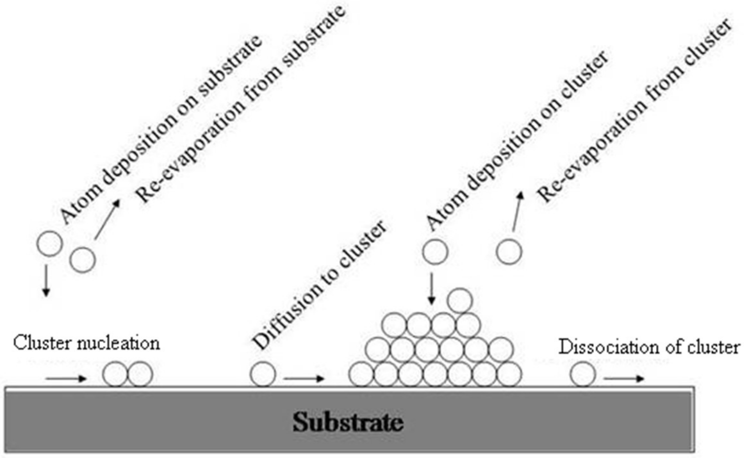

Figure 6: Schematic diagram of atomic processes in the nucleation of three-dimensional clusters of deposited film atoms on a substrate surface [31].

Dependening on the deposition parameters, atoms arrive either on clean substrate areas or on pre-existing clusters. These atoms can subsequently diffuse over the substrate or clusters, be re-evaporated from the substrate or from the clusters, or be sundered from the clusters remaining on the substrate surface. The total free energy of the cluster, which governs the balance between growth and dissolution processes, can be written using Greene's equation:

$$\Delta G = a_1 r^2 \gamma_{c-v} + a_2 r^2 \gamma_{s-c} - a_2 r^2 \gamma_{s-v} + a_3 r^2 \Delta D_V \tag{6}$$

where r is the radius of the cluster, and γ_{c-v}, γ_{s-c}, γ_{s-v} are cluster-vapour, substrate-cluster and substrate-vapour interface energies, respectively. ΔG_V is the change in volume free energy upon condensation of the cluster and a_1,a_2, a_3 are constants that depend on the shape of the nuclei [31].

If $a_1\gamma_{c-v} + a_2\gamma_{s-c} > a_2\gamma_{s-v}$ is satisfied, then the surface free energy will be positive and three dimensional cluster growth will dominate [31]. If the volume free energy is negative and the surface free energy is positive, the total free energy for cluster formation will (i) increase with atom addition for clusters smaller than the critical size and (ii) decrease with atom addition for clusters larger than the critical size. If the magnitude of the negative volume free energy increases and/or the surface/interface free energy decreases, the cluster radius will be stable and the cluster nucleation rate will increase. Negative volume free energy can be produced by increasing the deposition rate or decreasing the substrate temperature, which, on the other hand, will increase the supersaturation of vapour atoms on the substrate surface and decrease the surface diffusion coefficient of the absorbed vapour atoms. In the film deposition case, a decreased substrate temperature can slow the formation of a crystal structure, so that a metastable microstructure is produced. A common example of this phenomenon is the change from a crystalline to amorphous phase during the deposition process at low substrate temperatures.

1.2.1.2 Frank-van der Merwe nucleation and growth

If $a_1\gamma_{c-v} + a_2\gamma_{s-c} > a_2\gamma_{s-v}$ is not satisfied, then the layer-by-layer growth mode will be more favourable than three dimensional clusters on the substrate surface [31]. The condition for layer-by-layer growth can be written as

$$\frac{\gamma_{s-v}}{\gamma_{c-v}} - \frac{\gamma_{s-c}}{\gamma_{c-v}} \geq 1 \tag{7}$$

When the film is deposited on a clean surface of the same material, $\gamma_{s-c} = 0$ and $\gamma_{c-v} = \gamma_{s-v}$ and the above conditions are satisfied. If the film is deposited on dissimilar substrates, layer-by-layer nucleation will be promoted by the nucleation of islands, which are now only one monolayer thick and coalesce before significant clusters are developed on the next film layer (Figure 5).

1.2.1.3 Stranski-Krastanov nucleation and growth

Stranski-Krastanov growth is characterized by both two-dimensional layer-by-layer and three-dimensional island growth. The basic sequence is that the atoms initially form complete monolayers on the clean substrate and subsequently, nucleate three dimensional clusters on these layers, typically after 1–5 monolayers have been deposited. This three-dimensional cluster nucleation arises due to the increasing layer thickness in the stress due to mismatched lattice spacing.

Different growth modes have been observed for the same film-substrate system, thus clearly indicating that growth techniques and parameters are crucial to determining the final film morphology.

1.2.2 Influence of deposition parameters

Film growth and quality depend on a few fundamental parameters such as substrate temperature, laser fluence, laser wavelength, background gas and target-to-substrate distance [32].

1.2.2.1 Substrate temperature

The temperature of the substrate is an important parameter which has an influence on film morphology and thickening [33]. If the substrate temperature is low, the formation of particulates and lattice defects will increase. For higher substrate temperatures, the particles deposited on the substrate can be re-evaporated from the surface, nucleated into clusters or consumed by existing clusters. More film relaxation channels will be energetically accessible if the temperature of the substrate T_s is closer to the melting temperature of the film T_m. At low substrate temperatures ($< 0.2\ T_m$), metastable structures will be grown while at higher temperatures ($0.3\ T_m < T_s < 0.5\ T_m$), recrystallization occurs, yielding larger crystallites.

From the above discussion, it is clear that the microstructural morphology of the film is highly dependent on the growth temperature. Metastable structures are grown preferentially at lower substrate temperatures, while the growth of crystalline materials will require higher ($> 0.3\ T_m$) substrate temperatures.

1.2.2.2 Laser fluence and laser wavelength

The laser fluence on the target has the most significant effect on the particulate size and density, and plume visibility. If the fluence increases, the visible part of the plume will become longer due to the increasing energy of the ablated species. At high fluences, the formation of cones, cracks, craters and columnar structures on the target surface occurs and as a result, the plume can move away from the target normal. This effect can be also observed if the laser fluence is constant and the laser spot size on the target is reduced too much because a too small laser beam diameter can result in the ejection of droplets or large particulates from the target. The laser fluence, which is necessary for the stoichiometric ablation has to be higher than a certain threshold value. Above the threshold laser fluence, the particulate number density increases rapidly with increasing fluence and the rate of increase reduces at higher fluence, indicating saturation. The saturation of the particulate density at higher fluence may be exaggerated somewhat, since the adhesion of the particulates to the substrate appears to be poorer at elevated laser fluence [34]. The threshold value for the fluence has been determined for several different materials, and its dependence on the wavelength, pulse duration and beam size have been widely studied [17, 21, 35–37].

The laser wavelength λ comes into play mainly in regard to the effectiveness of the absorption of the laser energy in the target. For most metals, the absorption coefficient α decreases by decreasing λ, but for other materials, the variation of the absorption coefficient with wavelength is more complex because of the various absorption mechanisms. As the laser wavelength increases the particulate size and, the depth and width of the grooves generated on the target surface increase [38]. On the other hand, the correlation of the ejected particulate size, and depth or width of the grooves on the target surface is remarkable for it is difficult to say that the surface roughness in itself leads to the formation of particulates, although a smooth target usually produces fewer particulates after a few initial laser pulses irradiated on the target.

Kautek et al. [38] have shown that more and larger particulates are generated when using higher fluence and higher wavelength.

1.2.2.3 Background gas and /or vacuum

Background gas can enable the production of a multicomponent film (nitrides or oxides) from a monocomponent target, ablated in a reactive background gas (e.g. nitrogen or oxygen). If the deposition process takes place in the background gas, chemical reactions or non-reactive thermalising collisions between the energetic flux and the background gas will occur. Depending on the kinetic energy of the deposition fluxes, background gas can induce gas phase reactions, which can be introduced into deposited film. If the deposition flux has high kinetic energy and directionality, it will be usefully controlled by the introduction of a reactive or non-reactive background gas, but on the other hand, if the deposition flux has low kinetic energy and no directionality, it will be scattered by background gas collisions [33].

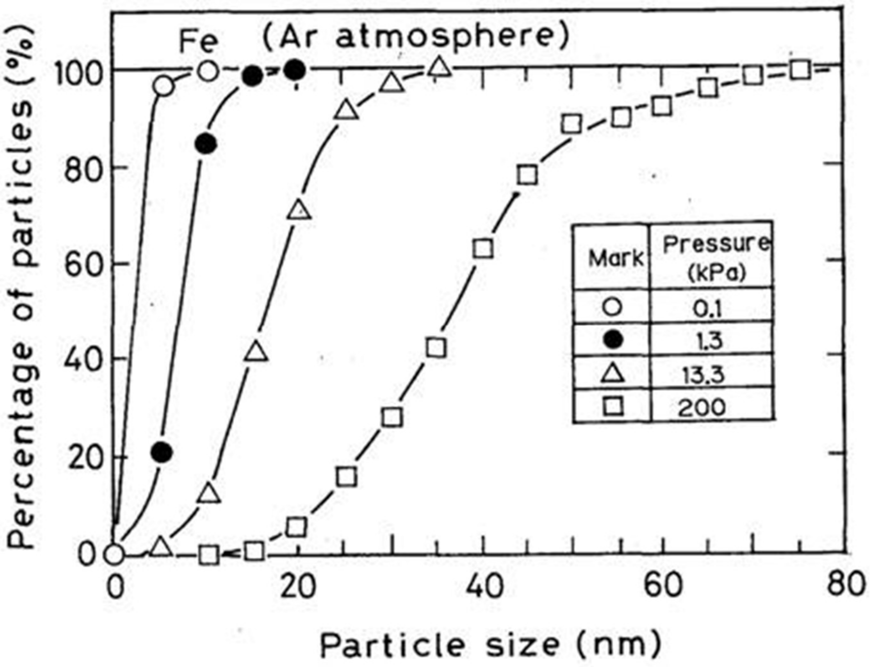

Figure 7: Particle size distributions of ultrafine Fe powder made under Ar pressure of 0.1; 1.3; 13.3 and 200 kPa [39].

The collision between the ejected species and the ambient gas depends on the ambient gas pressure [39]. If the ambient gas pressure increases, the collision and particle size (Figure 7) will increase as well and the vapour species will form particulates before arriving at the substrate.

If the deposition experiment is performed in a vacuum, the ejected species will diffuse in the plume and collide with each other, leading to a rapid thermalisation of the particle cloud [40]. In vacuum there are virtually no collisions between the ejected species before reaching the substrate. Therefore, particulates are predominantly formed from solidified liquid droplets that are expelled from the target by the recoiled pressure with the vapour species deposited as a uniform background film.

1.2.2.4 Target-substrate distance

In PLD experiments performed in poor vacuum or at ambient gas pressure, coalescence of particulates may occur depending on the distance between the target and the substrate. The effects of ambient gas pressure and target-substrate distance are interrelated. When the background gas pressure increases, the collisions between the laser-produced plume and background gas also increases, resulting in a plume with decreasing dimension. The length of the plume, L is given by

$$L \propto \left(\frac{E}{P_0}\right)^{\frac{1}{3\gamma}} \tag{8}$$

where E is the laser energy, P_0 the background gas pressure and γ the ratio of the specific heats of the elements in the plume [41].

When the target-substrate distance is significantly smaller than L, there is no huge difference in particulate size and density. If the distance increases, the proportion of the smaller particulates will decrease and a few larger particulates will appear, indicating coalescence during transport from the target to the substrate. If the target-substrate distance is significantly larger than L, the adhesion of ejected particulates and atomic species to the substrate will be poor.

1.2.2.5 Angular distribution of ablated material

The angular distribution of the ablated material either in vacuum or in the presence of an ambient gas has an influence on the film thickness and its composition. The stoichiometric transfer from the target to the substrate is one of the major characteristics of the PLD technique and for that reason it is also important to determine in what manner the film stoichiometry varies from the angle between the ejected species and target normal. The angular variation in the film composition can be linked to differences in the angular distribution of the plume components (ions, atoms, molecules, nm-µm particles) which may be associated with differences in their species charge and mass (heavy or light elements) [42]. The measurements in vacuum indicate that the laser plume is oriented along the target normal when the direction of the incident beam is also facing towards the target normal [43]. When the angle between the incident laser beam and the target normal is not zero, a plume deflection occurs. In the presence of an ambient gas due to collisions between the ablated particles and the background gas species, the plume particles are scattered from their original directions thereby broadening the angular distribution. In the multicomponent target, a higher distribution of the lighter elements is observed near the target normal [42].

The plume deflection effect is always present during long laser irradiation and it is due to the target surface roughness [44]. Manipulation of the substrate holder or alternative laser ablation geometries, e.g. normal laser incidence through the ablation plume, is essential in designing laser systems for deposition of uniform thin films [44] due to the deflection effect of the plume. The main components ablated in the direction of the incident laser beam are liquid droplets while for the oblique angles the main ablated components are monomers [45].

The above mentioned parameters affect the properties of thin films produced by PLD and can be varied. These variables allow the film properties to be manipulated somewhat, to suit individual applications. However, optimization can require a considerable amount of time and effort.

1.3 Selected materials for magnetic thin film fabrication by PLD

Magnetic films fabricated from rare earth (RE)-transition metal alloys are used in novel electronic devices, such as micro-circulators, isolators, magnetoresistive heads and micro-machines [46]. The main technologies used for thick/thin film fabrication are: bonding, screen-printing, sputtering, electro deposition and pulse laser deposition (PLD) [47, 48]. Thin films of engineering materials growth by PLD have optimum magnetic, optical and surface functionality in comparison to those fabricated using the above mentioned techniques [49]. Films fabricated by sputtering and PLD have proven to have the best magnetic properties, but problems implementing the technology on a wider scale persist because of low production efficiency (deposition in ultra high vacuum, heated substrates) and chemical, thermal and mechanical constraints. Nevertheless, ferromagnetic films of intermetallic alloys of rare-earth (RE) and transition metals have been successfully fabricated by sputtering and PLD [49].

PLD is the most suitable method for growing thin magnetic films such as Sm-Co [50–53], Nd-Fe-B [54, 55] and Sm-Fe-N [56–58]. The magnetic compound $Sm_2Fe_{17}N_3$ (used in our work) exhibits a high coercivity, large magnetic anisotropy and saturation magnetization and a high Curie temperature [59]. The fabrication of magnetic thin films by PLD is always accompanied by the formation of amorphous nano/micro droplets, especially at low laser energy and fluence. Films with nano/micro crystalline morphologies exhibit a coercivity of ~6.5 kOe with nanodroplet film morphology showing a lower coercivity in the order of ~ 0.11 kOe [60]. Furthermore, the presence of droplets implies an increased concentration of the α-Fe phase [56], which diminishes the magnetic properties of the film. In our samples, Ta is used as an additive element in the basic alloy to prevent the formation of the α-Fe phase during recrystallization [58, 61–63].

1.3.1 Magnetic properties

The magnetic properties of the materials can be described by their magnetic dipole moment m. The quantity of the magnetic moment per unit volume is called magnetization M, and is defined by the relation

$$M = nm \tag{9}$$

where n is the number density of magnetic moments. The magnetization defines the auxiliary magnetic field H as

$$B = \mu_0(H + M) \tag{10}$$

where B is the magnetic flux density and $\mu_0 = 4\pi * 10^{-7}\ NA^{-2}$ is the vacuum permeability. A relationship between magnetization M and the magnetic field H exists in many materials. In diamagnets and paramagnets, the relation is usually linear

$$M = \chi H \tag{11}$$

where χ is the magnetic susceptibility of the material. The sign χ determines whether the material is diamagnetic ($\chi < 0$) or paramagnetic ($\chi > 0$).

The field inside the material differs from the external field since magnetization induces a field opposite to the direction of the external field H_0, i.e. the total field is represented by

$$H = H_0 + H_d \tag{12}$$

where,

$$H_d = -NM \tag{13}$$

is the demagnetizing field and N the demagnetization factor.

Table 1: Summary of different types of magnetic behaviours [65].

Type of magnetism	**Susceptibility**	**Atomic/magnetic behaviour**
Diamagnetism	Small and negative Atoms have no magnetic moment	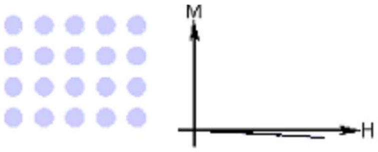
Paramagnetism	Small and positive Atoms have randomly oriented magnetic moments	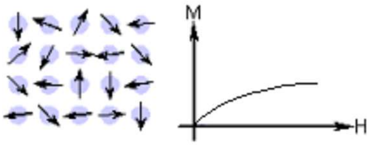
Ferromagnetism	Large and positive, function of applied field, microstructure dependent Atoms have parallel aligned magnetic moments	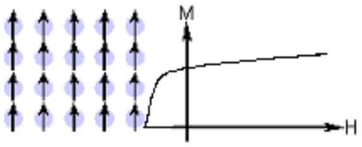
Antiferromagnetism	Small and positive Atoms have mixed parallel and anti-parallel aligned magnetic moments	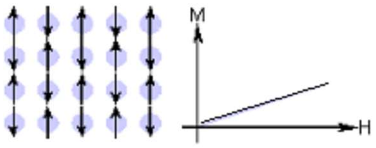
Ferrimagnetism	Large and positive, function of applied field, microstructure dependent Atoms have anti-parallel aligned magnetic moments	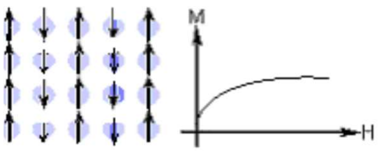

Materials may be classified by their response to externally applied magnetic fields as diamagnetic, paramagnetic, or ferromagnetic. Diamagnetic materials have a negative and very small susceptibility (10^{-5}). Diamagnetism is present in all materials, but usually hidden due to stronger forms of magnetism. Only superconductors show perfect diamagnetism with $\chi = -1$. Paramagnetism is stronger than diamagnetism and produces magnetization in the direction of the applied field proportional to the applied field. Some ferromagnetic (Fe, Co and Ni) and antiferromagnetic (Cr and Mn) materials at room temperature are para- or diamagnetic. All ferromagnetic materials above their Curie temperatures become paramagnetic. Paramagnetic materials have positive, but still relatively small susceptibility (10^{-5}–10^{-3}). Ferromagnetic effects are much larger than either diamagnetic or paramagnetic effects. Antiferromagnetic materials have small and positive susceptibility and may be regarded as anomalous paramagnets. Antiferromagnetic materials comprise some metal oxides, sulfides, chlorides, etc. Ferrimagnetic materials, such as ferromagnetics, consist of magnetically saturated domains and exhibit magnetic saturation and hysteresis. The most important ferrimagnetic materials are certain double oxides of iron and other metals, called ferrites.

Table 1.1 shows the classification of magnetic material according to their susceptibility and magnetic moment arrangement, respectively.

However, only ferromagnetic materials can produce forces strong enough to be felt, and they are responsible for the common phenomena of magnetism in everyday life. Ferromagnetic materials exhibit a long-range ordering of the magnetic dipoles, even in the absence of an external magnetic field. Magnetic ordering is primarily caused by a quantum mechanical exchange interaction between the spins of the neighbouring atoms [64]. Ferromagnetic materials spontaneously divide into domains.

The magnetic domains are separated by domain walls where the direction of the magnetization vector progressively changes from one orientation to another in order to minimize the cost in the exchange energy interaction. The exchange interaction is not perfectly isotropic but depends also on the absolute orientations of the spins with respect to the crystal axes and to each other. It is assumed that at zero field, a ferromagnetic sample is initially in a demagnetized state. When the magnetic field is switched on, the domain walls will begin to move in a favourable orientation with respect to the field increase.

Figure 8 schematically describes the process of increasing magnetization by applying a magnetic field to a ferromagnetic material.

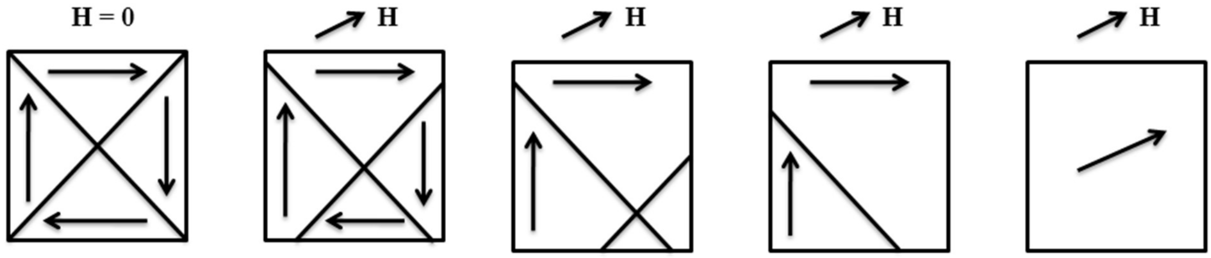

Figure 8: The effect of an applied field on a simplified domain structure [66].

When H=0, the spin moments are equally distributed along the easy directions. If H>0, the domain walls will move to increase the volume of the domains resulting in the smallest angle between magnetization direction and magnetic field vector.

1.3.1.1 Magnetic anisotropy

The anisotropy of materials is an important factor in determining the coercivity of bulk ferromagnets and epitaxial films. This means that the magnetic properties depend on the direction in which they are measured. The magnetization tends to stay along the easy axes and the energy required to rotate it away from the easy axes is defined as the anisotropy energy. For cubic crystals the anisotropy energy can be written as [64]

$$E_a = K_0 + K_1(\alpha_1^2\alpha_2^2 + \alpha_2^2\alpha_3^2 + \alpha_3^2\alpha_1^2) + K_2\alpha_1^2\alpha_2^2\alpha_3^2 + \dots\dots \tag{14}$$

where α_i are the cosines of the saturation magnetization M_s with respect to the crystal axes [100], [010], and [001] and K_i the cubic anisotropy constants expressed in J m^{-3}. Since a higher power to rotate magnetization away from the easy axes is not needed, K_2 is small enough to enable the third term in the above relation to be neglected. K_0 is independent of the angle and is usually ignored. If we take K_2=0, the direction of easy magnetization will be determined by K_1. If $K_1 > 0$, the easy axis of magnetization will be parallel to the [1 0 0] direction, but only if $K_1 < 0$, [1 1 1] is the easy direction.

In a hexagonal crystal the anisotropy energy is [64]:

$$E_a = K_{u,0} + K_{u,1} \sin^2 \theta + K_{u,2} \sin^4 \theta + \ldots\ldots \tag{15}$$

where the coefficients $K_{u,i}$ are called the uniaxial anisotropy constants and θ the angle between the saturation magnetization M_s and easy axis. Here, the easy axis of magnetization is the hexagonal c axis. The condition $K_{u,i} > 0$ means that the c axis is the easy axis of magnetization and energy is minimum for $\theta = 0°$. If $K_{u,i} < 0$, minimum energy will occur at $\theta = 90°$ and the easy plane of magnetization will be created here, perpendicular to the c axis.

1.3.1.2 Coercivity of magnetic thin films

The magnetization behaviour of a ferromagnetic material can be clearly described in terms of M-H or B-H magnetization curves (Figure 9). When the external field H is zero, the value of M is called the remnant or residual magnetization denoted by M_r and the value of B is called the residual flux density denoted by B_r. The reverse external field H_c that would demagnetize the material and make M or B zero is called the coercivity or coercive force. The second quadrant of the B-H curve, commonly referred to as the "demagnetization curve", describes the conditions under which ferromagnetic materials are used in practice. Based on their B-H behaviour, engineering materials are also typically classified into soft and hard magnetic materials (Figure 10).

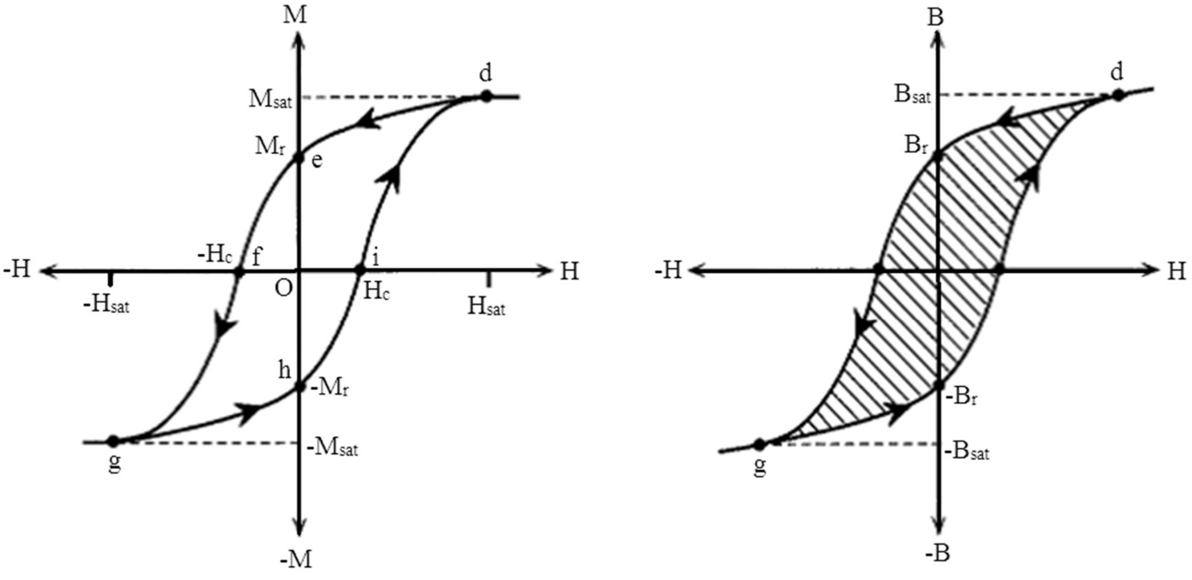

(a) (b)

Figure 9: a) Typical M versus H hysteresis curve: b) The corresponding B versus H curve [65].

Magnetically soft materials reach saturation quickly at low fields, whereas magnetically hard materials require much stronger fields to complete the magnetization process. Hard ferromagnets also have a significant remanent magnetization M_r and high coercive field H_c. By cyclically varying the magnetic field between the extreme values ± H, a hysteresis loop is formed as shown in Figure 9. The important properties of permanent magnetic materials are coercivity H_c, remanence B_r and the maximum energy product $|BH|_{max}$.

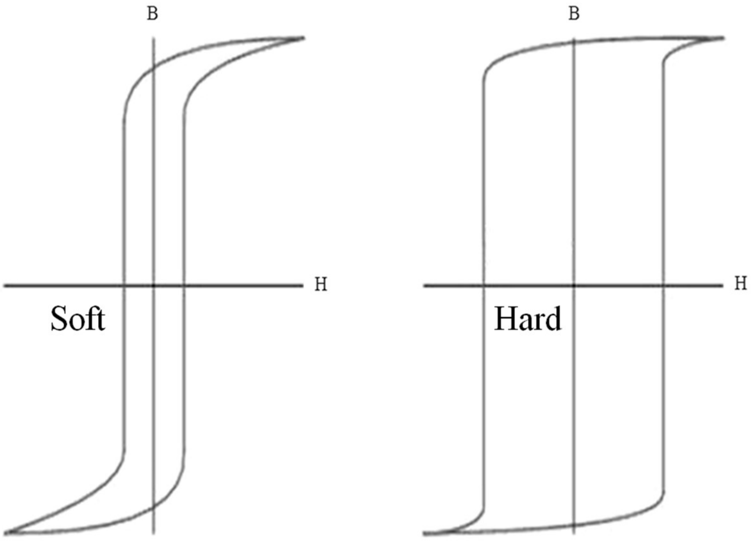

Figure 10: Soft and hard magnetic properties.

1.3.2 Sm-Fe-Ta

In R_2Fe_{17} (R = rare-earth metal) compounds, the magnetic moments of iron are almost as large as those in iron metal and are therefore possible candidates for permanent magnetic materials however their Curie temperatures are low at room temperature. The magnetic properties of R_2Fe_{17} are very sensitive to the elemental composition. It was found that interstitial H [68], C [69] or N [59] atoms are very effective in raising its Curie temperature T_C.

R_2Fe_{17} compounds always contain unreacted α-Fe [70]. If α-Fe exists as an impurity, it will prevent the compounds from attaining high coercivity, because it is a soft magnetic phase. It has been reported [71] that minor additions of *IV*B/*V*B/*VI*B group elements (Ti, V, Cr, Zr, Nb, Mo, Hf, Ta and W) significantly reduce the amount of α-Fe precipitated in the starting materials. For example, the addition of 4–5 % Ta in the SmFe alloy [62] can help to stabilize the rhombohedral structure and to reduce the soft magnetic impurity phases such as α-Fe. It was found that the SmFeTa alloys contain significant amounts of Sm_2Fe_{17}, $SmFe_2$, $SmFe_3$, $TaFe_2$ phases, but without the α-Fe [72]. To provide the highest coercivities for the conventional $Sm_{13.7}Fe_{86.3}$ binary alloy and $Sm_{13.8}Fe_{82.2}Ta_{4.0}$ alloy, Žužek et al. used the HDDR (hydrogenation-disproportionation-desorption-recombination) process, combining it with pre-attritor milling. Attritor milling prior to the HDDR treatment produces a small particle size and improves the magnetic properties [73].

1.3.2.1 Crystal structure and magnetic properties of $Sm_2Fe_{17}N_3$

The R_2Fe_{17} intermetallics crystallize in a rhombohedral Th_2Zn_{17} - type structure for light rare-earths (Figure 11a) and a hexagonal Th_2Ni_{17} - type structure for heavy rare-earths (Figure 11b). Upon exposure to N_2 gas (1 bar), 9e and 6h sites in R_2Fe_{17} are occupied by nitrogen and T_C (Figure 12) and M_S increases dramatically due to a lattice volume expansion of 5–7 %. For example, in $Sm_2Fe_{17}N_{3-\delta}$, T_C increases from 389 to 749 K and $\mu_0 M_S$ at 300 K increases from 1.0 T to 1.5 T and the planar anisotropy becomes strongly uniaxial, with K = 8.6 MJm^{-3} nearly twice that of $Nd_2Fe_{14}B$. This shows that nitrides exhibit strong ferromagnetism [74].

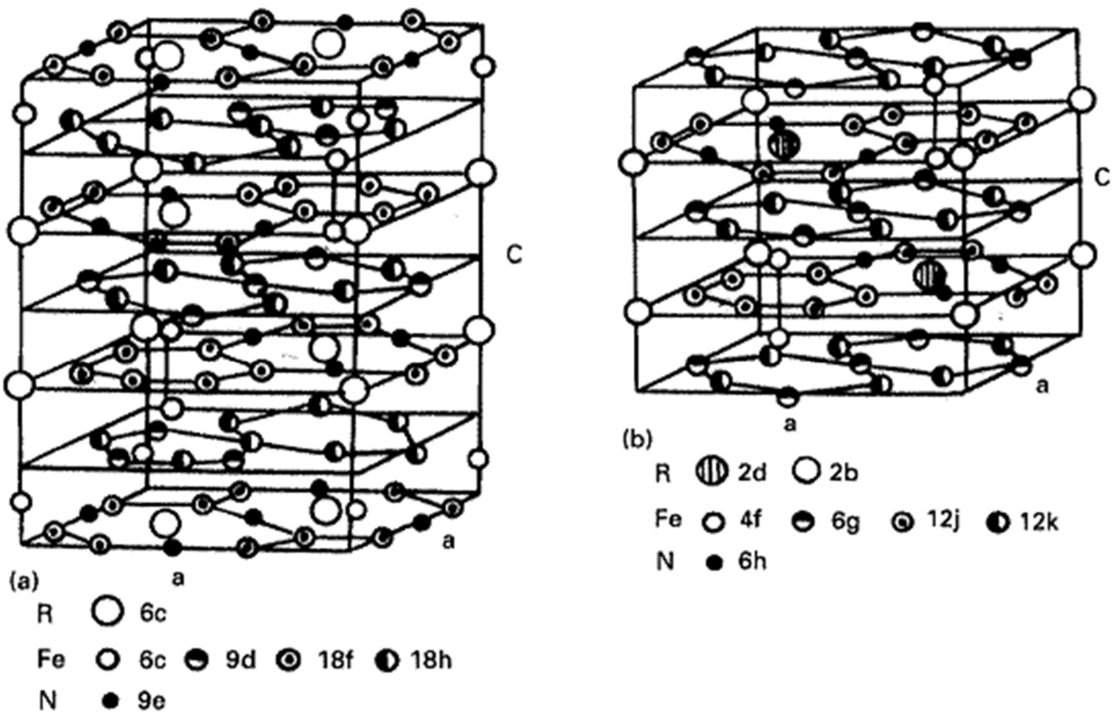

Figure 11: Structures of the rhombohedral (a) and hexagonal (b) varieties of R_2Fe_{17} [75].

The reaction between nitrogen and Sm_2Fe_{17} can be written as

$$\frac{1}{2}(3-\delta)N_2 + Sm_2Fe_{17} \rightarrow Sm_2Fe_{17}N_{(3-\delta)} \tag{16}$$

The 9e octahedral sites are completely filled if $\delta = 0$.

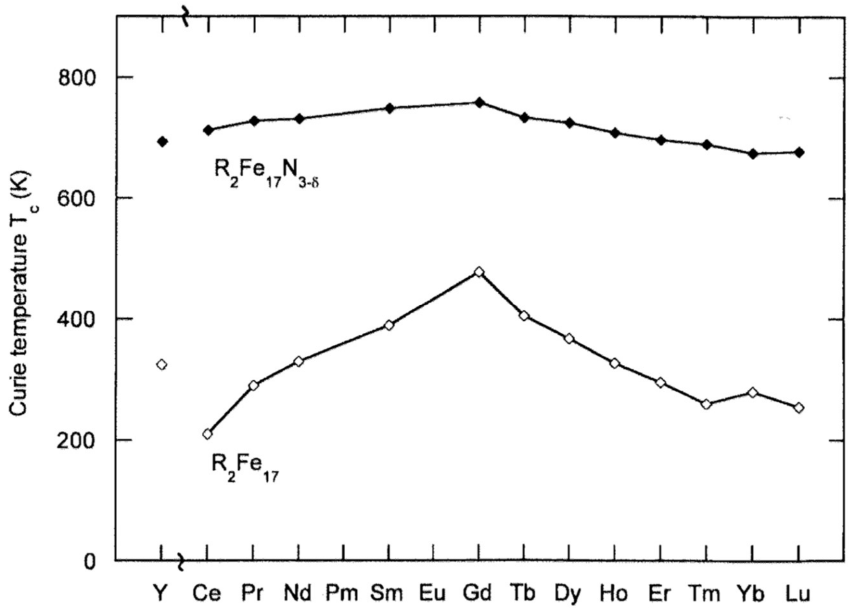

Figure 12: Curie temperatures of R_2Fe_{17} and $R_2Fe_{17}N_{3-\delta}$ compounds, with and without nitrogen [76].

The nitrogen content and homogeneity of nitrogenization have a major influence on the magnetic properties of $Sm_2Fe_{17}N_3$ due to the presence of incompletely nitrided particles, with the soft magnetic Sm_2Fe_{17} core unfavourable to the coercivity. The mechanism of nitrogen diffusion has been considered in detail by Coey and Skomski [67, 77] who proposed a mechanism of free diffusion in a gas-solid solution. The soft magnetic phases formed due to incomplete nitrogenation and/or nitriding for an excessive period can be avoided by decreasing particle size using a post-nitrogenization milling treatment [78].

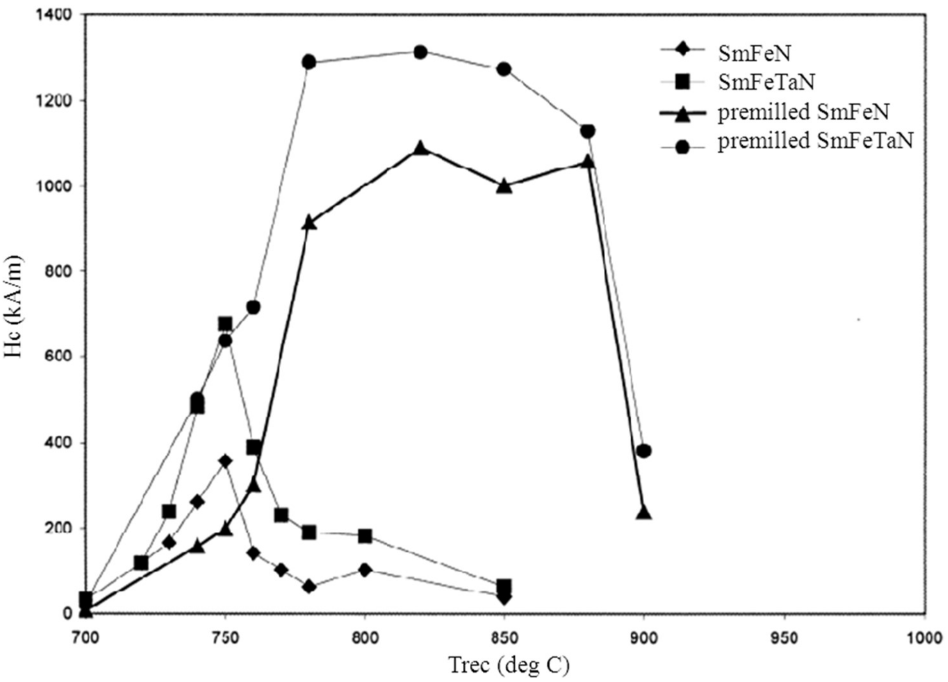

Figure 13: The coercivity force as a function of the recombination temperature for non pre-milled and pre-milled samples [73].

As mentioned previously, Ta additions and pre-milling of the material also affect the magnetic properties and microstructure of a conventional SmFe cast alloy [73]. The coercivity force as a function of the recombination temperature for non pre-milled and pre-milled samples is shown in Figure 13.

The coercivity of the SmFeTa sample (680 kA m^{-1}) is almost twice higher than the coercivity of the SmFe binary alloy (360 kA m^{-1}). In the case of the pre-attritor milled material, the coercivity is increased from 360 to 1075 kA m^{-1} for SmFeN and from 680 to 1280 kA m^{-1} for SmFeTaN.

These properties immediately mark $Sm_2Fe_{17}N_3$ as a potential permanent magnet material. The main advantages of $Sm_2Fe_{17}N_3$ materials over $Nd_2Fe_{14}B$-based materials are improved stability of the magnetic properties with respect to elevated temperatures [76].

1.4 Motivation and objectives

This work is meant to investigate *i*) the pulsed laser ablation process at two different wavelengths, namely at 213 nm (analytical Nd:YAG laser ablation instrument) and at 157 nm (true PLD molecular fluorine (F_2) laser), and *ii*) the subsequent deposition process to deposit Sm-Fe-Ta-N magnetic material (as thin films or layer of droplets) on a Si/Ta substrate. This thesis emphasizes this two-fold approach by providing a better understanding of the laser ablation process of a specific material ($Sm_{13.8}Fe_{82.2}Ta_{4.0}$), correlating the influence of the ablation conditions on the magnetic properties of the Sm-Fe-Ta-N material deposited.

Sm-Fe-Ta has been selected for its attractive properties, not only from an ablation viewpoint but also from a materials science point of view. Sm-Fe-Ta has been selected for its attractive properties, not only from an ablation viewpoint but also from a materials science point of view. Magnetic recording industry utilizes the trchniques for depositing high-quality ferromagnetic materials on magnetic storage media. Magnetic materials can be incorporated into MEMS with an extremely low cost. One important process in the research of magnetic MEMS is the deposition of magnetic materials on micro components.

PLD is a technique to deposit thin films of complex materials. Any material, from pure elements to multicomponent compounds can be deposited by PLD techniques, the stoichiometry of the material is reproduced in the film, and it is simple and low cost technique.

On the other hand, the evaporation and sputtering methods are largely physical deposition processes and a CVD relies on chemical reactions. The evaporated films have very poor ability to cover the surface topology and by evaporation is difficult to produce well controlled alloys.

Conceptually and experimentally, PLD is relatively simple, probably the simplest among the all thin film growth techniques. Pulsed-laser deposition (PLD) has gained a great deal of attention in the past few years because of its using for depositing materials of complex stoichiometry. Many materials that are normally difficult to deposit by other methods, especially multi-element nitrides or oxides, have been successfully deposited by PLD. The main limitation of PLD at the present time is that, some issues related to industrial scale-up have yet to be addressed. In particular, deposition of films on large-area substrates may be difficult.

A thorough study on the complex interactions between a laser beam and solid target ($Sm_{13.8}Fe_{82.2}Ta_{4.0}$) will be executed to achieve a good optimum between ablation, deposition and material characteristics. Critical PLD parameters in both laser ablation instruments such as energy density, laser diameter, target-substrate distance, gas flow rate in the ablation chamber, etc. will be established. PLD demonstration experiments in He and N_2 will be performed with the $Sm_{13.8}Fe_{82.2}Ta_{4.0}$ target using Ta-coated silicon substrates in a contraption with defined geometry in the laser ablation chambers.

Commercial laser ablation-inductively coupled plasma mass spectrometer (LA-ICPMS) systems for elemental microanalysis have similar lasers as PLD instruments but not the possibility to work under high vacuum conditions. However, in many instances PLD can be successfully executed under atmospheric conditions in the presence of an inert gas, even for the target material ($Sm_{13.8}Fe_{82.2}Ta_{4.0}$) used in this study. This suggests that commercial LA-ICPMS systems may be used to good effect as well, with the added advantage of in situ analysis of the ablation plume and ex situ analysis of the deposited particles.

Although the primary function of an analytical laser ablation instrument (213 nm) is the elemental characterization of solid materials by modifying the laser ablation cell (target-substrate contraption), it can be converted into a laser-assisted deposition apparatus with auxiliary elemental analysis opportunities to diagnose and optimize the particle fabrication process. This LA instrument offers in situ monitoring facilities, making the intended use of the analytical laser ablation instrument very novel from a particle fabrication point of view, i.e. its dual use for synthesis and diagnostics of the fabrication process. The detection and characterization of the ablation plume via measurements of the ablated components in the plume using a hyphenated ICPMS instrument will be investigated, thus providing a data set against which to test models for the ablation process. The understanding of the processes governing laser ablation was fundamental to subsequently studying the influence of the ablation and deposition process parameters on the properties of the deposited material. Additionally, the density, homogeneity and stoichiometry of the deposited material were investigated and the PLD parameters optimized using the LA-ICPMS instrument as an elemental mapping tool in combination with image analysis. In this way, information was gathered on the density and stoichiometry of the deposited material.

The use of a true PLD laser (157 nm) for synthesis of magnetic nanodroplets with controlled size, shape, composition, morphology and surface chemistry was also investigated. The nucleation and growth of nanodroplets under various thermodynamic/kinetic conditions were systematically studied and a general methodology developed to fabricate a variety of magnetic nanoparticles with desirable morphologies and controlled magnetic properties.

A suite of characterization techniques will be used to reveal the properties of the particles in the plume (ICPMS) and particles deposited (SEM-EDXS, TEM, XRD, AFM, VSM, SQUID). The properties of the $Sm_{13.8}Fe_{82.2}Ta_{4.0}$ particles will be compared in order to observe the similarities and differences of the particle formation processes in both laser ablation instruments used.

2 Materials and Methods

A schematic overview of the experimental approach is given in Figure 14 which will be discussed in this chapter, including the experimental parameters used. General information about the techniques used for characterization is given in Appendix 1.

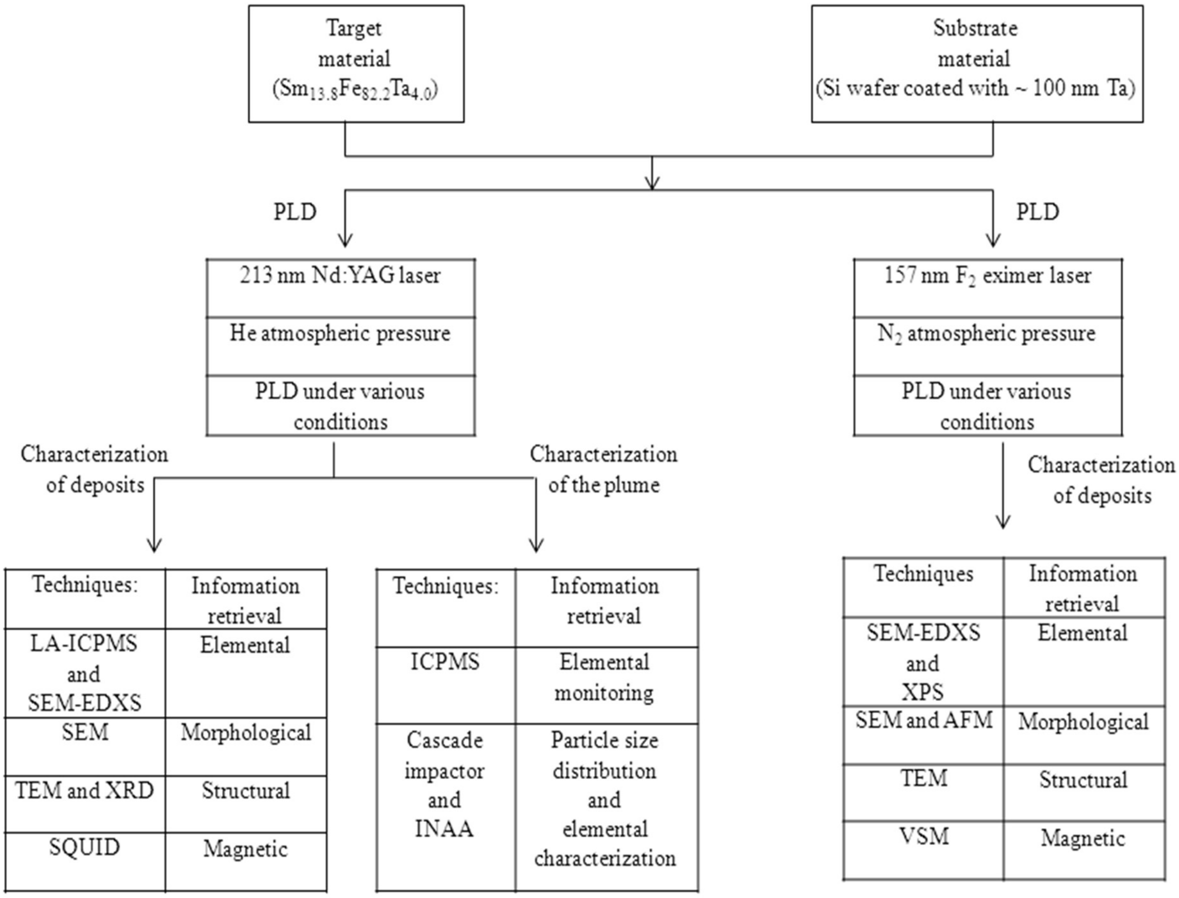

Figure 14: Schematic overview of the experimental approach.

2.1 Materials

2.1.1 Target material

A $Sm_{13.8}Fe_{82.2}Ta_{4.0}$ alloy was used as the target material, obtained using the conventional induction melting method by Less Common Metals [73]. The target`s dimensions were 10 mm x 5 mm with a thickness of 2 mm. The target was polished before each experiment to remove the oxidized surface layer.

2.1.2 Substrate material

Layers were grown on Si substrates coated with 100 nm thick layers of Ta to prevent a reaction between the Si substrate and film. The Ta film was deposited by sputtering (CemeCon CC800/7 at 10^{-3} to 2×10^{-3} mbar). The substrate`s dimensions were ca. 6 mm x 3 mm with a thickness of 0.21 mm.

The substrate`s coated surface morphology is shown in Figure 15 (left). The average surface roughness in the Z direction over an area of 150 x 150 nm was 3.4 nm. The film morphology over a larger area of 50 x 50 µm is indicated in Figure 15 (right) showing an average surface roughness in the Z direction of 65 nm.

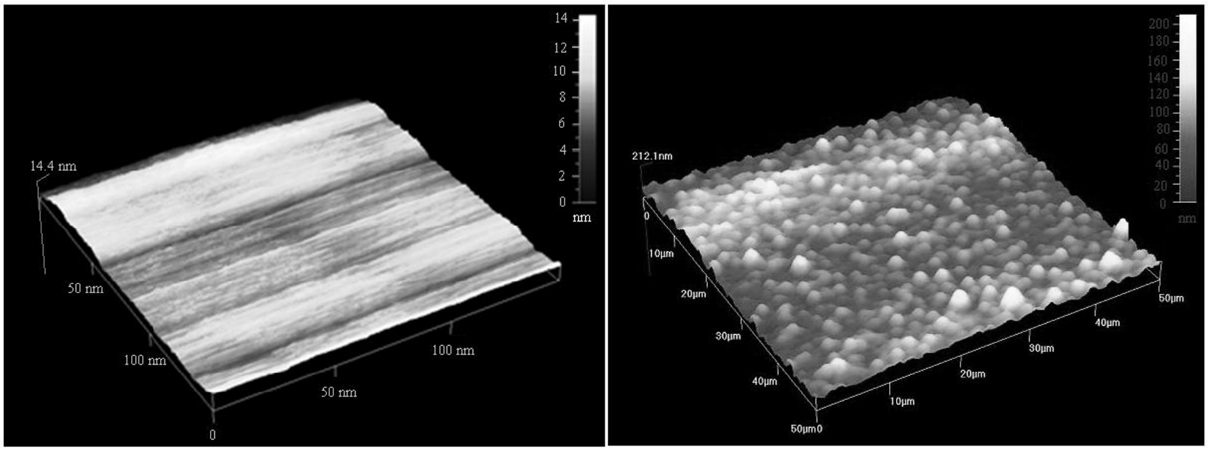

Figure 15: AFM images of the surface of the Ta film grown by sputtering on the Si substrate. The surface roughness in the Z direction over an area of 150 nm x 150 nm (left) and 50 µm x 50 µm (right).

2.2 PLD setups

Pulsed laser deposition is a technique for depositing almost any material on a selected substrate. High-power laser pulses for the ablation process were produced by a F_2 excimer laser (Lambda Physik LPF 200) and a solid state Nd:YAG laser (New Wave Research UP 213).

2.2.1 157 nm Lambda Physik LPF 200 Laser Ablation System

High power laser pulses for the ablation process are produced by the Lambda Physik LPF 200 molecular fluorine (F2) laser. The output wavelength of the laser is 157 nm [79] and the pulse duration 15 ns FWHM (full width at half maximum). The maximum repetition rate and output energy are 20 Hz and 20–55 mJ, respectively.

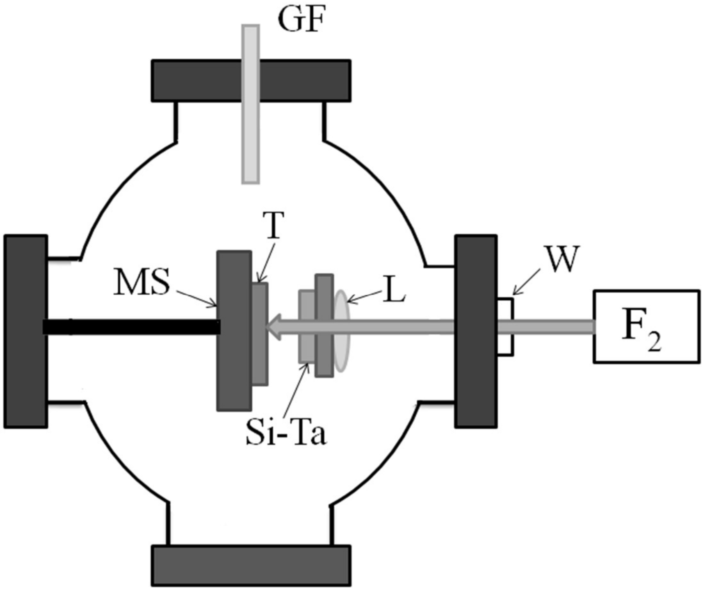

Figure 16: Experimental configuration for 157 nm PLD. F_2: 157 nm laser. MS: X-Y-Z-θ computer controlled stage. GF: Gas filling system. T: Target. L: Focusing and CaF_2 projection system. W: CaF_2 window.

The high quantum energy of 7.9 eV of 157 nm photons not only allows for efficient ionization, but also opens the door to an extension of laser-material processing to optical materials. Optical materials have wide band gaps and are made in such a high purity grade that they do not absorb in their spectral window of use.

Hence, they usually withstand powerful laser radiation in that spectral range. However, in vacuum ultraviolet (VUV) almost all materials absorb strongly, especially 157 nm light. The 157 nm laser usually occupies dissociative-repulsive electronic or ionizing states that lead to molecular photo dissociation within the fs time scale. Thus, 157 nm radiation from F_2 lasers may extend the well-known advantages of laser-material processing to materials not easily treatable by conventional laser light. The 157 nm laser offers the shortest available laser wavelength. Its photon energy of 7.9 eV acts as a “hammer” when interacting with free atoms or molecules, or in material processing. The excellent coupling of high peak power radiation into the samples yields clean ablation in materials that are difficult to process at other common laser wavelengths.

The experimental apparatus used in our investigation is indicated in Figure 16. It comprises a 157 nm F_2 laser, a high quality beam projection CaF_2 optical system and a computer-controlled X-Y-Z-θ motorized stage, combined with a CCD camera for real time imaging and automatic control. The CaF_2 optics is protected from the ablative products with a CaF_2 window (1 mm thick). The target is placed inside a 316 stainless-steel chamber on a translation stage, which operates with 2 μm resolution steps and repeatability. The PLD process takes place in a He or N_2 environment and/or under high vacuum conditions (10^{-7} mbar), depending on the application.

To investigate the structure and magnetic properties of Sm-Fe-Ta-N nanodroplets fabricated by 157 nm PLD, we used a $Sm_{13.8}Fe_{82.2}Ta_{4.0}$ target, positioned perpendicular to the laser beam and focused with a high quality CaF_2 lens, through a 5 mm aperture in a compact geometry. The distance between the target and the substrate was 1.5 cm or 0.5 cm (results are presented in section 3.2.1). Films were grown in an atmosphere of pure nitrogen (1 bar) with laser energy of 10 mJ or a laser fluence of 3–5 J cm^{-2} (~ 600 μm laser spot size on the target) and a repetition rate of 15 Hz. The CaF_2 optical elements were protected from the ablative products with a CaF_2 window, which was replaced after 10 h of PLD. Focusing of the laser beam in the Z direction was aided by the computerized micrometric translation stage.

To investigate the size distribution, the stochiometry and morphology configurations of Sm-Fe-Ta-N deposits grown by 157 nm PLD from $Sm_{13.8}Fe_{82.2}Ta_{4.0}$ solid targets on Si/Ta substrates, the target was placed inside the stainless steel chamber on the translation stage and positioned perpendicular to the laser beam. The deposits were grown on the substrates, which were placed in three different orientations with respect to the target. One orientation was opposite to the target along the direction of the laser beam at 180° and along other two coplanar orientations perpendicular to the laser beam at 90° and 270°, respectively (results are presented in section 3.2.2). The X-Y micro-motion of the target allowed continuous ablation under tight laser beam focusing. In order to establish optimum ablative and deposition efficiency conditions, the distance between the target and substrate was adjusted to 1.5 cm and the laser energy was varied between 1 and 50 mJ. At 20 mJ and 1.5 cm, the growth rate of the deposit was 100 nm per hour in N_2 atmosphere (1atm).

2.2.2 New-Wave Research UP 213 Laser Ablation System

The schematic setup of the laser ablation system is shown in Figure 17. The laser ablation device contains a frequency-quintupled Nd:YAG laser with a wavelength of 213 nm and a pulse width of 4 ns. The fluence is typically 0.1–30 J cm^{-2}. The objective lens focuses the high-intensity pulsed ultraviolet (UV) beam through a window onto the sample surface in an ablation cell which is placed on a motorized stage to move the sample in the *x*, *y* and *z* direction (with sub-micrometer resolution) to the desired ablation location. The motorized *x* and/or *y* translational stages allow line scanning or rastering on the target surface. Line scan speed range typically ranges from 1–2000 μm s^{-1} and spot sizes vary from 4 to 250 μm, accurately set by a software-controlled aperture. The pulsed UV beam irradiates the sample surface and ablates a small amount of material, producing a plume with only one or several pulses. The UP 213 laser ablation system may be fired at rates of 1–20 Hz. The ablation process can be visualized using a CCD camera with a high magnification and a computer-controlled zoom.

The ablation cell where the PLD process takes place, a so-called SuperCell^{TM} (New Wave Research), has a small void volume (10 mL). The ablation cell houses the various target-substrate contraptions (Figures 18, 19 and 20). The ablation cell can be filled or continuously mixed with a carrier gas which, depending on the application, can be helium, argon, a mix of helium and argon or a reactive gas (nitrogen, oxygen).

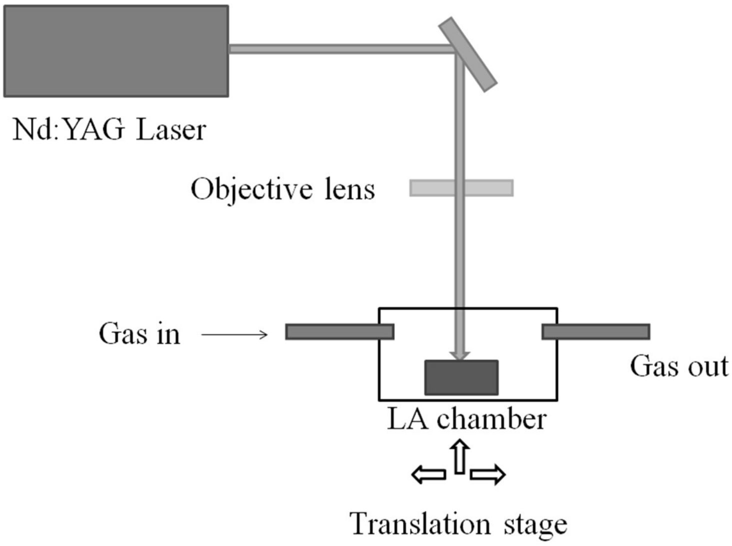

Figure 17: Schematic setup of the components of the UP 213 laser ablation system. The photographs show the complete laser ablation system and details of the laser ablation cell with a contraption to support the target and substrate (see also Figures 18 and 19).

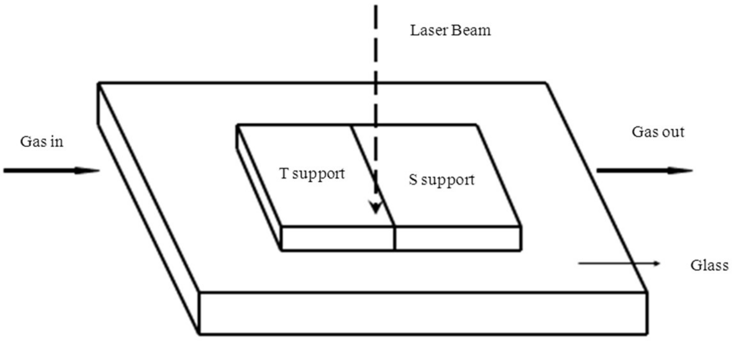

Figure 18: Target-substrate geometry for PLD (Configuration 1).

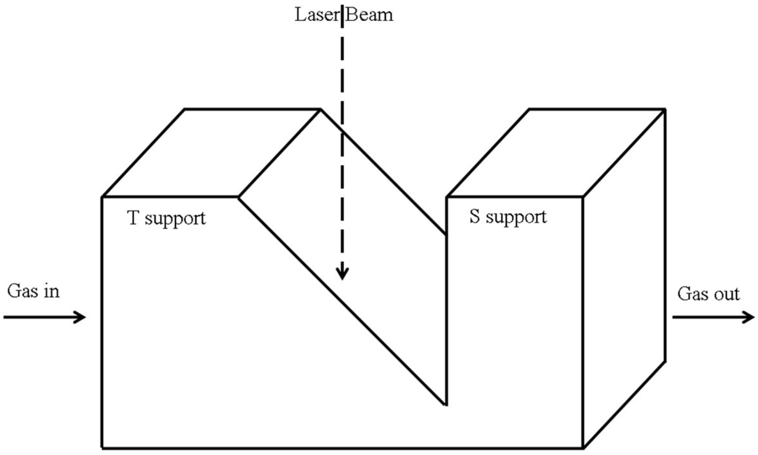

Figure 19: Target-substrate geometry for PLD (Configuration 2)

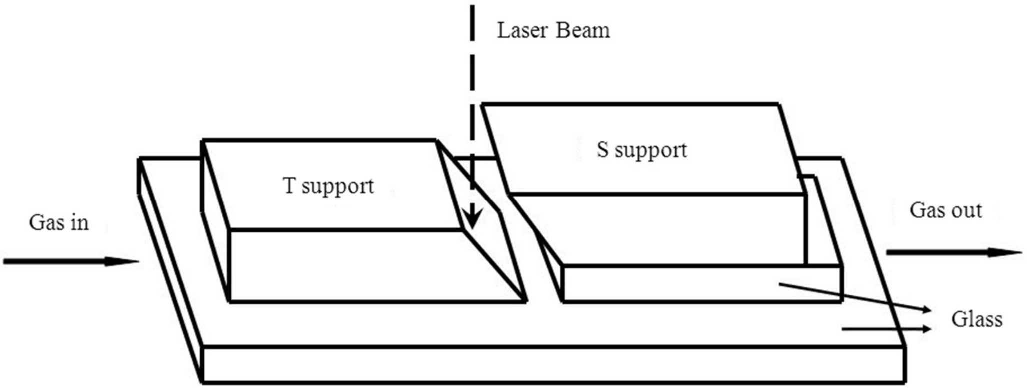

Figure 20: Target-substrate geometry for PLD (Configuration 3).

To investigate the PLD process (efficiency, accuracy, etc.), various target-substrate PLD configurations in the ablation cell were tested as a function of external parameters (laser fluence, type of background gas and gas flow rate). The PLD configurations tested are shown in Figures 18, 19 and 20. Initially, the target and substrate were mounted (using double-sided tape) on a glass slide next to each other with as little spacing as possible, perpendicular to the laser beam and with the target-substrate contraption in line with the gas flow direction (Figure 18). Subsequently, the laser beam was incident to the target surface at an angle of 45° and parallel to the substrate surface (Figure19), and in a third configuration, target-substrate contraption was used which angled both the target and substrate 45° with respect to the laser beam, keeping the target and substrate parallel (Figure 20). The contraptions in Figure 19 and 20 were custom-made out of PVC and were freestanding and mounted (using double-sided tape) on a glass slide, respectively. The substrate support (Figure 20) was mounted on a 1 mm higher piece of glass slide enabling the distance between the target and substrate to be adjusted. The target and substrate were attached to the respective angled contraption parts; the straight edge of the substrate was aligned parallel to the top edge of the substrate support. The laser beam was focused on the target, half-way up the target's height.

2.3 Characterization methods for ablation products

2.3.1 In-line methods

The target material which is not deposited on the substrate, i.e. aerosol particles of a certain size and composition, can be studied by connecting the laser ablation system to an external instrument (in-line characterization), i.e. an ICP-MS (inductively coupled plasma mass spectrometer) for elemental analysis or a Berner 10-stage cascade impactor for size-segregation purposes.

Inductively Coupled Plasma Mass Spectrometry (ICP-MS): In situ elemental ICPMS analysis of the PLD plume was performed as a function of the laser fluence (0.1–15 J cm^{-2}), crater size (8–100 µm) and repetition rate (1–20 Hz) under the following operational parameters: He flow rate, 0.95 L/min; Ar make up flow rate, 0.75 L min^{-1}, scanning speed, 10 µm s^{-1} time-resolved analysis of ^{57}Fe and ^{147}Sm (both 0.1 s acquisition time).

Cascade Impactor: The particle size distribution generated in the laser ablation process was investigated by a Berner ten-stage low-pressure cascade impactor which covers the sizes between 38 nm and 1.6 µm. The cascade impactor was connected to the laser ablation system (New Wave Research UP 213) by simply hovering the outlet tube of the laser ablation cell in the inlet part of the impactor. A vacuum pump was adjusted to create a pressure gradient which resulted in a throughput of 25 L min^{-1}. Clean Tedlar impaction foils were used and particles collected for 30 min. The absolute elemental amounts impacted on the foils were measured by instrumental neutron activation analysis (INAA) as described in section 2.3.2.

2.3.2 Off-line methods

For deposited material on the substrate, off-line characterization methods will be applied for morphological, elemental, structural and magnetic analysis.

Laser Ablation-Inductively Coupled Plasma Mass Spectrometry (LA-ICPMS): Laser ablation-

ICPMS is a microanalytical solid sampling technique for determining trace elements directly in all types of solid samples with minimum sample preparation. Laser ablation (LA) is a highly sensitive technique with a wide analytical dynamic range from part per billion (ppb) to percent (%) in the solid. For more than twenty years laser ablation in combination with ICP-MS has been used as one of the most effective solid sampling techniques for bulk elemental analysis [80]. By traversing the laser beam over the sample (rastering), one can generate element maps of the surface of a sample and in our case, obtain information on particles deposited on the substrate, i.e. particle density, homogeneity and stoichiometry as a function of the laser fluence, He flow rate and target-substrate distance at 30 min deposition time. He (5.0) was used to transport the ablated material from the ablation chamber to the ICPMS for elemental analysis (see 2.3.1.1). Mapping was performed under the following rastering/acquisition conditions: laser fluence, ca. 4 J cm^{-2}; laser beam diameter, 80 µm; scanning speed, 150 µm s^{-1}; pulse rate, 10 Hz; line distance, 100 µm; He flow rate, 1.0 L min^{-1}; acquisition time, 0.2 s ^{57}Fe and 0.4 s ^{147}Sm. Subsequent image analysis was carried out using Origin 7.5 SR4 software (OriginLab Corporation, Northampton, USA).

Scanning Electron Microscopy (SEM): A SEM-EDXS instrument (FE-SEM SUPRA 35VP [Carl Zeiss] equipped with an Inca 400 [Oxford Instruments] EDXS was used to investigate the morphology of the material deposited on the substrate by both instruments (157 nm and 213 nm) and quantitatively analyze the relevant elements. For this instrument the sample (Si/Ta substrate with Sm-Fe-Ta-N particles deposited on) was fixed (using double-sided carbon tape) on the holder with a diameter of 3 mm. The aperture size was set to 30 µm and the working distance to 4–6 mm; EHT was adjusted to 3–5 kV. For EDXS analysis, the aperture size was set to 60 µm and the working distance to 8.5 mm; EHT was adjusted to 20 kV.

Transmission Electron Microscopy (TEM): The nanoscale structure and crystallinity of the Fe-Sm-Ta-N nanoparticles deposited by both PLD instruments (157 nm and 213 nm) were investigated using a JEOL 2010 F field-emission transmission electron microscope (TEM) with STEM unit, bright field-dark field detector, a Gatan PEELS 677 and Gatan off-axis TC camera. TEM was equipped with an EDXS Link Isis from Oxford Instruments for elemental chemical analysis. The structure was determined using different electron diffraction techniques (SAED - selected area electron diffraction and microdiffraction). The microscope operates at 200 kV with a resolution of around 0.19 nm.

For TEM analysis, the deposited material from the substrate was transferred to a carbon-coated Cu grid using a scalpel. This Cu grid is 3 mm in diameter with 200 mesh (with openings around 50 µm) and is coated with a very thin layer of amorphous carbon.

Atomic Force Microscopy (AFM): The surface morphology of the Sm-Fe-Ta deposited material on the substrate was investigated using a Quesant, Q-ScopeT 250 atomic force microscope (AFM), equipped with a 40-µm Dual PZT scanner. The available scanning modes are Contact AFM-Z Height and Lateral Force, Intermittent Contact AFM (WaveModea) and Phase Mode. Besides AFM, the magnetic force microscopy (MFM) option is also available. The Q-ScopeT 250 operates inside an acoustic and thermal isolation chamber with the stability of the system controlled by a laser interferometer.

The AFM images were acquired in ambient conditions, in tapping-mode by a silicon cantilever coated with a 30-nm thick aluminum reflex film (Quesant *Premounted on a T-Plate*) with a nominal spring constant of 48 N m^{-1} (20–100 N m^{-1}) at a resonance frequency of 190 kHz (130–250 kHz) and nominal radius < 10 nm. The AFM images were obtained at different scanning areas with a maximum scanning rate of 3 Hz and an image resolution of 512 x 512 pixels. The AFM microscope was placed inside an acoustic isolation chamber.

Diffraction (XRD): The XRD spectra of the deposited Fe-Sm-Ta-N particles obtained using a commercial laser ablation instrument (213 nm solid state Nd:YAG laser) were taken by a PANalytical X'Pert PRO X-ray powder diffractometer (room temperature; radiation wavelength CuKα_1 = 1.5406 Å; 2θ = 20° to 75°) to elucidate the crystalline phases.

X-Ray Photoelectron Spectroscopy (XPS): The XPS spectrum of the surface and XPS depth profile of the elemental distribution in the Sm-Fe-Ta-N particles were obtained by a Physical Electronics Inc. model TFA XPS. The surface of the deposited material was analyzed to a depth of 3–5 nm with a 400 µm electron beam profile. XPS spectra were excited by X-ray radiation from an Al-standard source. The base pressure in the spectrometer was 2×10^{-8} Pa. Ion sputtering was performed with a 1 keV Ar^+ ion beam rastered over the entire area of the sample. It was estimated that the relative deviation for the composition analysis was 20 %.

Vibrating Sample Magnetometer (VSM): The magnetic properties of our samples (Sm-Fe-Ta-N core-shell nanodroplets) were measured using a VSM Lake Shore 7003 device at room temperature in field range from 14 kOe (1.4 T) to –14 kOe back to 14 kOe. The sensitivity is a high as 5×10^{-6} emu and can achieve a magnetic field from –1.4 to 1.4 Tesla and attain temperatures down to 7 K. The cryostat operates with a closed liquid helium circuit. The samples are mounted on a plastic sample holder with a dimension of 5 mm x 20 mm and positioned in the VSM.

Superconducting Quantum Interference Device (SQUID): Magnetic measurements of the Sm-Fe-Ta material deposited on the Si/Ta substrate upon ablation of $Sm_{13.8}Fe_{82.2}Ta_{4.0}$ by a commercial 213 nm laser ablation instrument were performed using a Quantum Design MPMS-XL magnetometer. This magnetometer contains a high precision temperature control system enabling measurements between 1.9 K and 400 K with an accuracy of 0.01 K. It has a very high sensitivity up to 10^{-14} T, but requires cooling with liquid helium (4.2 K) to operate. A superconducting magnet provides magnetic fields of up to 5 T.

Instrumental Neutron Activation Analysis (INAA): The aerosol particles generated upon laser ablation of the $Sm_{13.8}Fe_{82.2}Ta_{4.0}$ target by the 213 nm laser were size-segregated in a cascade impactor and the elemental ratios of the deposited material on the Tedlar foils measured by INAA. The foils (ca. 0.2 g) were sealed into pure polyethylene ampoules (SPRONK System, Lexmond, Netherlands) with a high of 8 mm and a diameter of 8 mm. A sample and standard Al-0.1 % Au (IRMM-530RA disc of 6 mm in diameter and 0.1 mm high) were stacked together, fixed in the polyethylene vial in sandwich form and irradiated for 8 hours in the carousel facility (CF) of the TRIGA reactor with a thermal neutron flux of 1.1×10^{12} $n\cdot cm^{-2}\cdot s^{-1}$. After irradiation, the samples and standards were measured following 4 and 15 days cooling time on absolutely calibrated HPGe detectors with 40 and 45 % relative efficiencies. The HyperLab program was used for peak area evaluation, whereas the “Cd-ratio” method for multi monitor [81] was used to determine f (thermal to epithermal flux ratio) and α (parameter which represents the epithermal flux deviation from the ideal distribution). The values $f = 28.63$ and $\alpha = -0.0011$ were used to calculate the element concentrations. Calculation of the elemental concentrations and effective solid angle calculations was carried out using the KayWin software package, which is based on the k_0-standardization method of neutron activation analysis.

3 Results and Discussion

Our research of laser ablation is focused on two areas, namely the laser ablation process itself and the properties of the deposited material. Correlation of the two areas provides an integrated picture of the best process parameters to use when seeking to deposit a material with given properties. This chapter emphasizes this two-fold approach by describing the laser ablation process of a specific material and correlating it to the final properties of the deposited ablation product.

Laser ablation and pulsed laser deposition of $Sm_{13.8}Fe_{82.2}Ta_{4.0}$ have been studied in this work at two different wavelengths, namely at 213 nm with a commercial Nd:YAG laser ablation-inductively coupled plasma mass spectrometer (LA-ICPMS) intended for analytical microanalysis and at 157 nm using a real PLD instrument (molecular fluorine (F_2) laser). The ablation process at 213 nm was studied using an ICPMS instrument that allows direct investigation of the LA plume by monitoring the amount of laser ablated species as a function of the laser fluence, laser beam diameter and pulse rate. Further investigations of the pulsed laser ablation and deposition process were performed using different laser wavelengths, fluences, gas flow rates and target-substrate distances. Laser excitation of the solid with these different parameters reveals different ablation mechanisms and properties, which are reflected in the properties of the deposited material.

This chapter is directly based on published/presented scientific data:

Articles

Azdejković, J. M.; Elteren, J.; Žužek, R. K.; Jaćimović, R.; Sarantopoulou, E.; Kobe, S.; Cefalas, A. C. Dual purpose laser ablation-inductively coupled plasma mass spectrometry for pulsed laser deposition and diagnostics of thin film fabrication: preliminary study. *Talanta* **79**, 583 (2009).

Cefalas, A. C.; Kobe, S.; Sarantopoulou, E.; Samardzija, Z.; Janeva, M.; Dražić, G.; Kollia, Z. Growth, clustering and morphology of intermetallic alloy core-shell nanodroplets. *Physica Status Solidi (a): Applications and Materials Science* **205**, 1465 (2008).

Kobe, S.; Sarantopoulou, E.; Dražić, G.; Kovač, J.; Janeva, M.; Kollia, Z.; Cefalas, A. C. Growth of crystalline/amorphous biphase Sm-Fe-Ta-N magnetic nanodroplets. *Applied Surface Science* **254**, 1027 (2007).

Conference contributions

Azdejković, J. M.; Elteren, J.; Žužek, R. K.; Jaćimović, R.; Sarantopoulou, E.; Kobe, S.; Cefalas, A. C. Optimization of PLD for Fe-Sm-based thin film fabrication using an analytical laser ablation system interfaced with an inductively coupled plasma mass spectrometer. *Hot nano topics 2008: incorporating SLONANO 2008, 3 overlapping workshops on current hot subjects in nanoscience, 23–30 May, Portorož, Slovenia : abstract book.* 245 (Ljubljana: [s. n.], 2008).

Azdejković, J. M.; Elteren, J. Dual purpose laser ablation ICP-MS for PLD synthesis and elemental analysis to rapidly optimize thin film fabrication. *15th Young Investigators' Seminar on Analytical Chemistry (YISAC), Ljubljana, Slovenia*, July 2–5, 2008. *Book of abstracts*. 111–112 (Ljubljana: Faculty of Chemistry and Chemical Technology, 2008).

3.1 Dual purpose laser ablation-inductively coupled plasma mass spectrometry for pulsed laser deposition and diagnostics of thin film fabrication

In this section, the potential of a commercial LA-ICPMS system (213 nm Nd:YAG laser) for PLD purposes was investigated using $Sm_{13.8}Fe_{82.2}Ta_{4.0}$ as the target material. The hyphenated ICPMS instrument was tested for in and ex situ ICPMS analysis for diagnostics of the ablation process and detailed analysis of the deposition process, respectively. The LA system was also attached to a ten-stage low-pressure cascade impactor to investigate the size and composition of particles generated by the LA process. The elemental signal ratios in the ablated plume were monitored to ensure the absence of large particles; this was also independently checked by multi-stage cascade impaction of particles leaving the laser ablation chamber. The investigation of the pulsed laser deposition was focused on the optimization of the deposition parameters, i.e. laser fluence, type of ambient gas, gas flow rate and target-substrate distance using the LA-ICPMS instrument as an elemental mapping tool in combination with image analysis. The deposited material grown under the given conditions was analyzed using numerous characterization techniques (SEM-EDXS, TEM, XRD, SQUID) to reveal its properties.

3.1.1 Influence of the target position to the laser beam and to the substrate on the deposit morphology

Initially, the PLD work with the 213 nm Nd:YAG laser ablation system was focused on the optimization of the proper target-substrate geometry for maximum deposition in He at atmospheric pressure. $Sm_{13.8}Fe_{82.2}Ta_{4.0}$ was used as the target material in these experiments. The morphology and composition of the deposited material on the Si/Ta substrate for 30 min in a horizontally aligned (Figure 18, Configuration 1) and 45° angled target-substrate geometry (Figure 19, Configuration 2), using a laser fluence of 2.3 J cm^{-2} and He flow rate of 0.95 L min^{-1}, were investigated using SEM-EDXS.

The deposited material, as can be seen in the SEM images, is consisted mainly of spherical shaped nano- and micro-droplets (Figure 21a) and fragments (Figure 21b). Initially, they were formed in the ablation plume and subsequently deposited on the substrate in the liquid phase. The size distribution of the droplets ranged between 200 nm – 1 μm. SEM-EDXS analysis of the particles indicates that their composition is close to that of the target material (Fe, 84 at. %; Sm, 16 at. %).

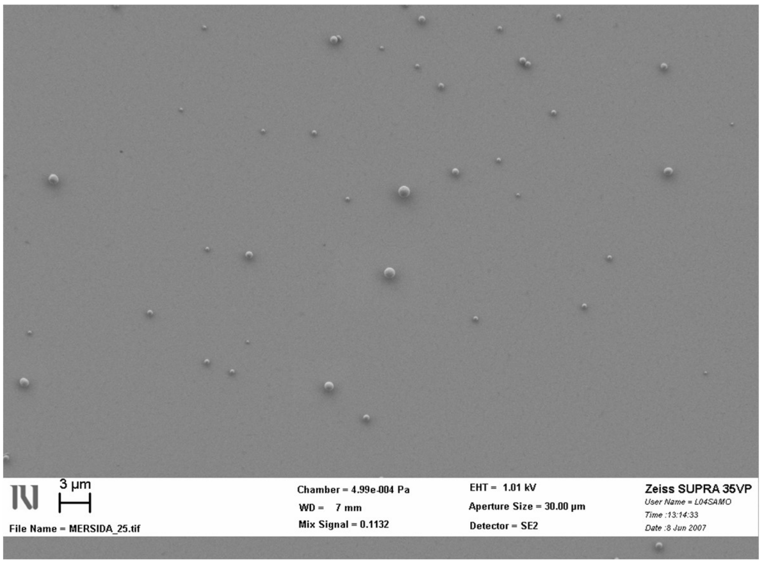

Figure 21a: SEM image of the Sm-Fe-Ta droplets with different size deposited in He at atmospheric pressure.

The results are promising but show poor deposition efficiency, most likely the result of incorrect target-substrate geometry. Cultrera et al. [82] found that maximum deposition occurs at about 45° to the target normal, i.e. in the incident laser beam direction. Replicating this angled target-substrate geometry (Figure 20, Configuration 3) for our PLD case, the deposition efficiency was increased enormously as can be seen in Figure 21c. A dendritic-like deposition pattern is observed, which upon close inspection (zooming in) consisted of random conglomerates of single spherical particles.

The elemental composition (Fe, 78 at. % and Sm, 22 at. %) shows an enrichment in samarium compared to the target material. This phenomenon can probably be attributed to the low laser fluence (2.3 J cm^{-2}). The heat of vaporization and the vaporization temperature of iron are much higher than that of samarium, causing iron to vaporize with more difficulty compared to the samarium, resulting in lower deposition efficiencies.

The expulsion of the different species and deposition rates observed in different directions can be due to the deflection of the plume caused by the collisions between the ablated species and ambient gas, and due to the generated grooves on the target surface [82].

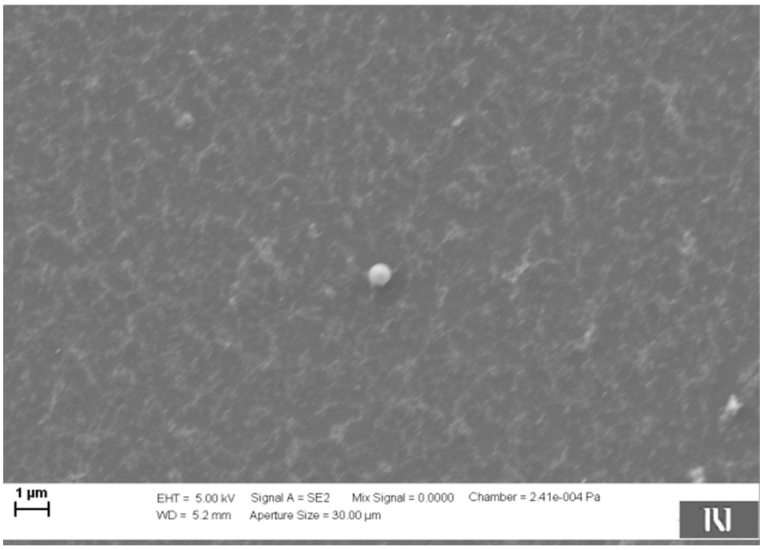

Figure 21b: SEM image of the Sm-Fe-Ta droplets and fragments with different size deposited in He at atmospheric pressure.

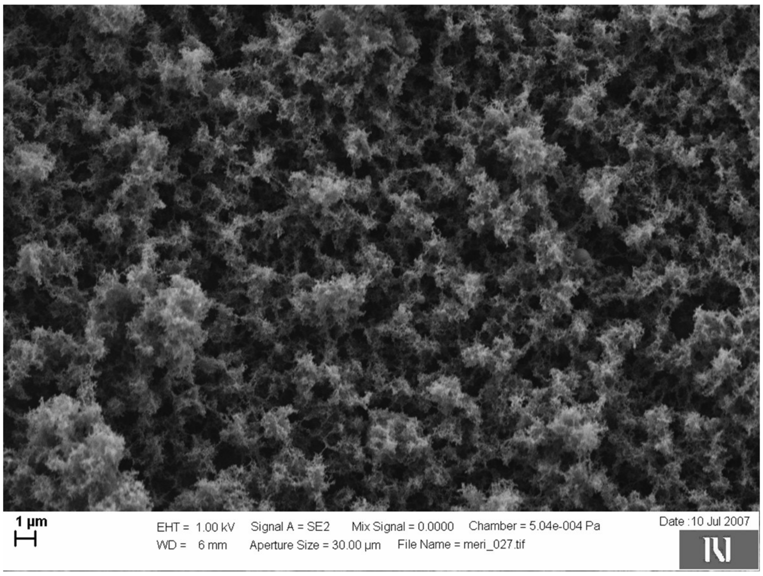

Figure 21c: SEM image of the Sm-Fe-Ta layer deposited in He at atmospheric pressure.

From the above results it can be concluded that the position of the target in relation to the laser beam and to the substrate significantly influences the deposit composition and morphology.

3.1.2 Target homogeneity

The properties of the ablated material depend on laser characteristics, as well as target properties. Since the composition of the deposited material is directly related to the target composition, a highly homogenous target is very important for the PLD process. For this reason, one part of this work was focused on the investigation of the homogeneity of the $Sm_{13.8}Fe_{82.2}Ta_{4.0}$ target used in all further experiments for producing Sm-Fe-Ta layers and nanodroplets.

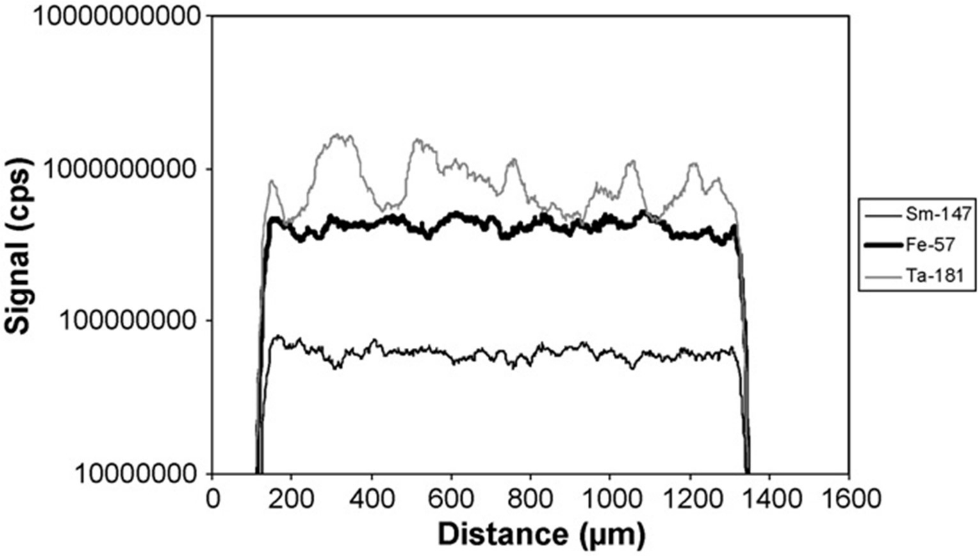

Figure 22: Elemental signals upon traversing the $Sm_{13.8}Fe_{82.2}Ta_{4.0}$ target. Operational LA-ICPMS parameters: fluence, 10 J cm^{-2}; laser beam diameter, 100 µm; repetition rate, 10 Hz; scanning speed, 10 µm s^{-1}; He gas flow rate, 0.95 L min^{-1}, RF power, 1500 W; acquisition time, 0.1 s for each mass.

Under conditions optimal for LA-ICPMS microanalysis (high He flow rate to minimize transport losses and a high ICP RF power to maximize the evaporation of particles), the target was ablated and the ^{57}Fe, ^{147}Sm and ^{181}Ta signals monitored upon traversing the target. From Figure 22 it can be observed that Ta is less homogeneously distributed than Fe and Sm. The target material is a melt composite of $SmFe_2$, $SmFe_3$, Sm_2Fe_{17} and $TaFe_2$ with a low amount of Ta (4.0 at. %) present in only one of the phases [72]. Since the much more abundant Sm (13.8 at. %) and Fe (82.2 at. %) are present in three and four of the phases, respectively, it is obvious that Ta is less homogeneously distributed in the target than Sm and Fe. The Ta heterogeneity may have consequences for the homogeneity of the final deposit fabricated although deposits with appropriate characteristics (magnetic properties) have been fabricated from the very target using a real PLD instrument [63, 83]. In the continuation of this work predominantly ^{57}Fe and ^{147}Sm signals and their ratios were monitored.

3.1.3 In situ elemental monitoring of the PLD plume generated in He

In the in situ PLD diagnostics procedure, the majority of particles from the ablation plume (>99 %) is transferred to the ICPMS. In PLD one desires to deposit small particles on the substrate only, as arrival of macroscopic globules of molten material up to ca. 10 µm diameter is detrimental to the properties of the deposited material. The use of ICPMS as an on-line detector may aid in the optimization of the PLD parameters for generating small particles with an appropriate stoichiometry.

Principally, the particles generated should have the same composition as the target; however, elemental fractionation may occur due to the laser-target interaction and/or transport of the particles to the ICP-MS. Laser ablation of solid material involves the processes of heating, melting and evaporation of the sample material at an extremely high temperature and pressure. Mass may be removed from the target in the form of atoms, molecules, vapour, droplets, solid flakes, large particulates or a mixture of these forms. Large particles may not be completely vaporized even if they are successfully transported to the ICP-MS, which may result in additional elemental fractionation in the ICP-MS itself. It should be noted that the latent heat of evaporation plays a leading role, not only in the decomposition of particles during plasma heating, but also in the formation of particles during cooling of the ablated material in the ablation cell.

Guillong and Günther [84] have shown that the U/Th ratio upon ablation of NIST glass 610 (measured as a cps ratio), using a 266 nm Nd:YAG system, dramatically depends on the conditions for ablation as a result of the particle size. They claim that their fractionation findings are due to ICP-enhanced processes related to particle size, critically limited to diameters above 1µm. Filtering the large particles resulted in a better U/Th ratio (closer to unity as implicated by almost identical first ionization potentials for U and Th) in all instances. In our case, using an opaque target instead of a transparent target and a 213 nm Nd:YAG system instead of a 266 nm Nd:YAG system, we can estimate that a large proportion of the particles have a diameter below 0.2 µm [85] and are therefore less influenced by the ICP.

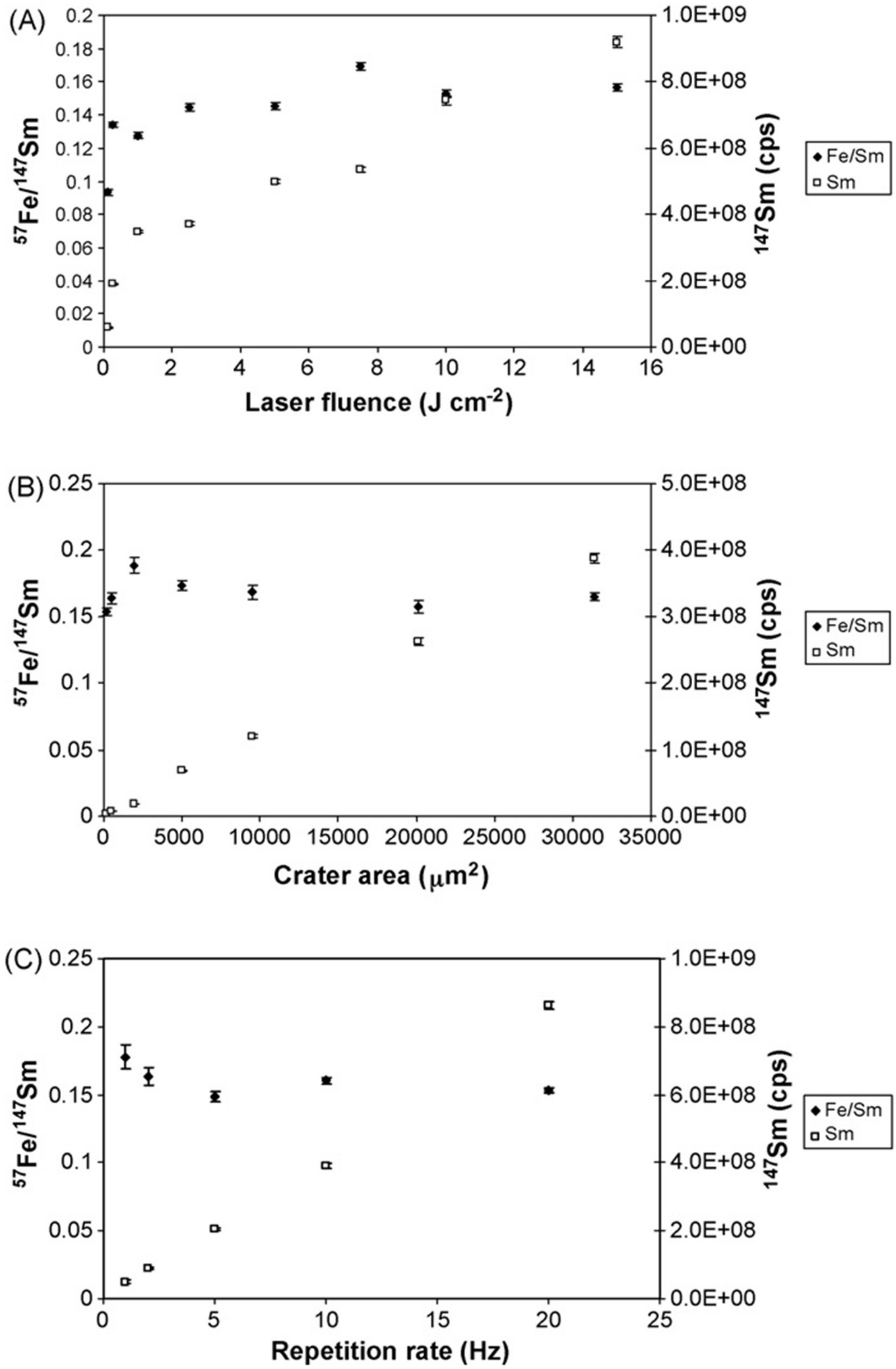

Figure 23: Influence of laser fluence (A), crater area (B) and repetition rate (C) on the ^{147}Sm signal and the ^{57}Fe/^{147}Sm ratio. For operational default LA-ICPMS parameters, see Figure 22. Error bars denote the uncertainty in the measurement.

From Figure 23 it can be observed that experiments with an ICPMS tuned for normal LA-ICPMS microanalysis work do not show significant differences in the ^{57}Fe/^{147}Sm ratios (measured as cps ratios) upon ablation of the $Sm_{13.8}Fe_{82.2}Ta_{4.0}$ target as a function of the following PLD parameters: laser fluence (0.1–15 J cm^{-2}, Figure 23A), laser beam diameter (8−100 µm, Figure 23B) and pulse rate (1–20 Hz, Figure 23C). The average ^{57}Fe/^{147}Sm ratio for all experiments was 0.16, with a maximum deviation of ±5 %. None of the PLD parameters tested appears to compromise the average stoichiometry of the particles in the plume as governed by the ^{57}Fe/^{147}Sm ratio measured. The elemental signals (in cps) in Figure 23, given for Sm but similar for Fe and Ta, augment these observations via their linear proportionalities with regard to laser fluence (after overcoming an initial threshold), crater area and repetition rate. It seems logical to conclude that for all PLD parameters tested (for a range of conditions) the nominal particle size is below 1 µm, which is supposed to be the limit for the occurrence of ICP-enhanced processes [84]. The validity of this assumption was also verified by size segregation of particles in a ten-stage cascade impactor (see section 3.1.5).

3.1.4 Ex situ LA-ICPMS of the particles deposited in He

When particles are deposited on a substrate and a deposit is generated, one desires to maximize the deposit density and at the same time, minimize the deposit heterogeneity. Furthermore, one strives for an average stoichiometry which reflects that of the target. Using the LA-ICPMS as an elemental mapping tool, the influence of laser fluence, He flow rate and target-substrate distance on these deposit properties were investigated.

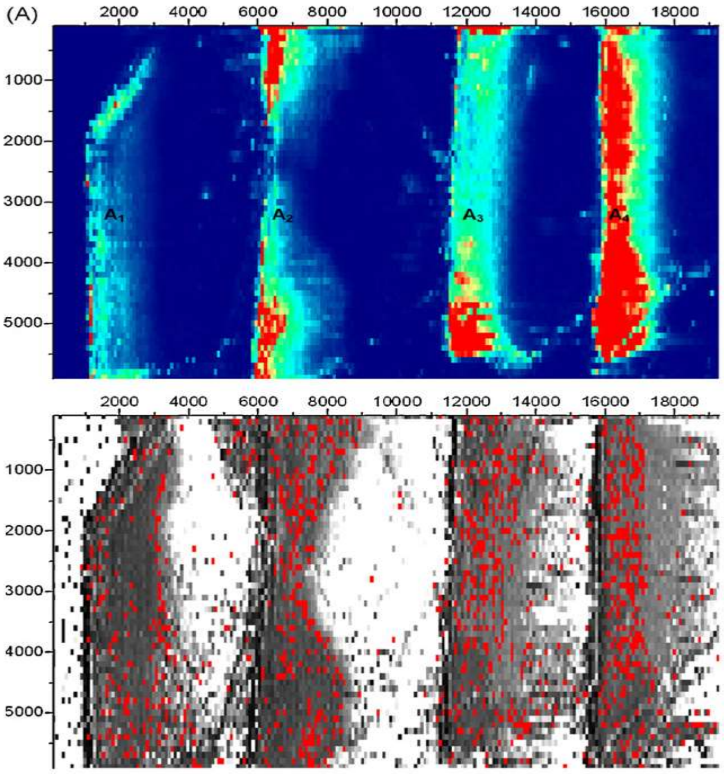

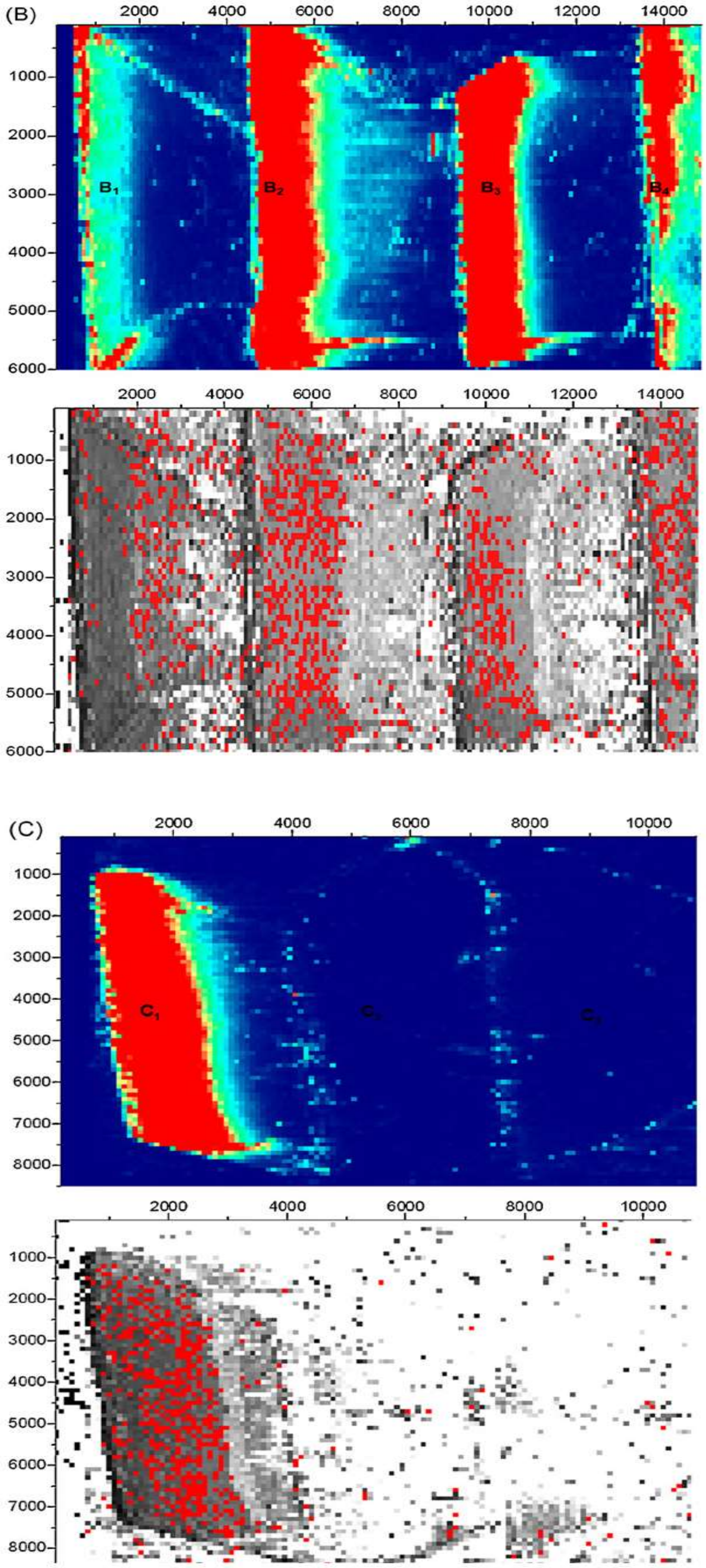

Figure 24: Element maps (scale in µm) of ^{57}Fe and ^{57}Fe/^{147}Sm for substrates generated at varying fluence (A_1 = 1.7 J cm^{-2}, A_2 = 3.9 J cm^{-2}, A_3 = 6.1 J cm^{-2}, A_4 = 9.3 J cm^{-2}), He flow rate (B_1 = 0 L min^{-1}, B_2 = 0.3 L min^{-1}, B_3 = 0.6 L min^{-1}, B_4 = 1.0 L min^{-1}) and target-substrate distance (C_1 = 2 mm, C_2 = 3 mm, C_3 = 4 mm), with the first image (in JET colours) denoting the ^{57}Fe maps and the second image (in shades of gray, with red pixels indicating the target stoichiometry [± 5 %]) the ^{57}Fe/^{147}Sm maps. For JET colours lower image densities are mapped onto “cool” colours and higher densities onto “hot” colours; low density images are shown in blue or violet, and high density images appear as orange or red. Operational default PLD parameters: fluence, 9 J cm^{-2}; He gas flow rate, 0.3 L min^{-1}; target-substrate distance, 2 mm; laser beam diameter, 100 µm; repetition rate, 10 Hz; scanning speed, 10 µm s^{-1}, deposition time, 30 min.

In Figure 24 the findings of the mapping are given for ^{57}Fe (similar for ^{147}Sm) as an indication of the deposit density, and for ^{57}Fe/^{147}Sm as an indication of the deposit homogeneity and stoichiometry. The ^{57}Fe maps are given in so-called JET colours to display the range of concentrations in an illustrative way. The ^{57}Fe/^{147}Sm maps are expressed in 256 shades of grey with the actual target stoichiometry (^{57}Fe/^{147}Sm ratio of 0.16 as found by analysis of the plume upon ablation of the target, see section 3.1.3) indicated as red pixels with a deviation of ± 5 % from this value.

Since the laser fluence is more or less directly proportional to the amount of particles generated above a certain threshold (Figure 24A) it is no surprise that in Figure 24A the largest fluence (9.3 J cm^{-2}) yields the highest deposit density (A4). The average stoichiometry for this fluence is also very close to the target's stoichiometry as can be seen from the red pixel distribution in the section referring to this deposit. In Figure 24B one can see that a He flow rate of 0.3 L min^{-1} yields the thickest deposit (B2) with a stoichiometry closest to that of the target. From Figure 24C it can be observed that the target-substrate distance is very critical in the generation of a thick deposit; 2 mm is the only distance which yields a film having a composition close to that of the target (C1). For other background gases, the findings most probably differ due to the effect of the thermal conductivity of the gas on the particle diameter and size of the laser-induced plasma [89]. The optimized PLD parameters (A4, B2 and C1) were used to fabricate deposits for further characterization.

The Fe and Sm distribution in the layer deposited using a 9.3 J cm^{-2} laser fluence (A4), 0.30 L min^{-1} He flow rate (B2) and 2 mm distance between target and substrate (C1) was the highest obtained. Relative concentration densities on the substrates are shown in Table 2 as found using MCID Analysis™ software (Imaging Research Inc.). In all three cases (A, B and C, Figure 24), the highest density was arbitrarily set to 100. It can be seen that the relative densities of Fe and Sm are very similar for the fluence and He flow rate parameters, indicating that the overall (average) particle composition deposited is more or less independent of these parameter settings; only the absolute amounts deposited seems to vary significantly.

Table 2: Relative concentration densities on the substrates for the cases A, B and C in Figure 24.

Fluence (J cm^{-2})	Fe (rel. dens.)	Sm (rel. dens.)
S1: 1.7	6.92	8.71
S2: 3.9	27.4	37.82
S3: 6.1	37.08	41.2
S4: 9.3	**100**	**100**
He flow rate (L min^{-1})	Fe (rel. dens.)	Sm (rel. dens.)
S1: 0.00	7.69	16.33
S2: 0.30	**100**	**100**
S3: 0.61	97.53	99.42
S4: 1.00	21.08	17.93
T-S distance (mm)	Fe (rel. dens.)	Fe (rel. dens.)
S1: 2	**100**	**100**
S2: 3	0	0
S3: 4	0	0

3.1.5 Verification of the particle size distribution in He

The laser ablation outlet was sampled by a ten-stage cascade impactor with the distribution data obtained by INAA given in Figure 25.

It is clear that the particle size distribution under a laser fluence of 9 J cm^{-2} results in the generation of small particles (Figure 25A), with ca. 95 % [w/w] having an aerodynamic diameter $D_{ae} \leq 0.75$ µm. By ablating a target of $Sm_{13.8}Fe_{82.2}Ta_{4.0}$ we expect to collect aerosol particles which resemble the composition of the target (28.1 % [w/w] Sm, 62.1 % [w/w] Fe and 9.8 % [w/w] Ta). The average particle composition is fairly similar to this target composition with 26.7 % [w/w] Sm, 65.1 % [w/w] Fe and 8.2 % [w/w] Ta. However, the elemental distribution is not identical for all particle sizes (Figure 25B).

The mass-weighted deviation from the measured average particle composition for each size fraction indicates that Sm and Ta are more or less equally distributed over the particle sizes whereas Fe shows a reverse trend to make the mass balance neutral (neutral here means in accordance with the measured average particle composition). It is unclear why Sm and Ta behave similarly, especially since they are the most and least volatile of the three elements investigated, respectively. In general, smaller particles tend to be enriched with more volatile elements and larger ones depleted [86, 87]. However, the mass-weighted composition of the various particle sizes never differs more than ca. 10 %. The findings not only confirm that nanoparticles are generated in the LA setup used, but also that the composition of the particles reflects that of the target with little mass-weighted inter-particle heterogeneity.

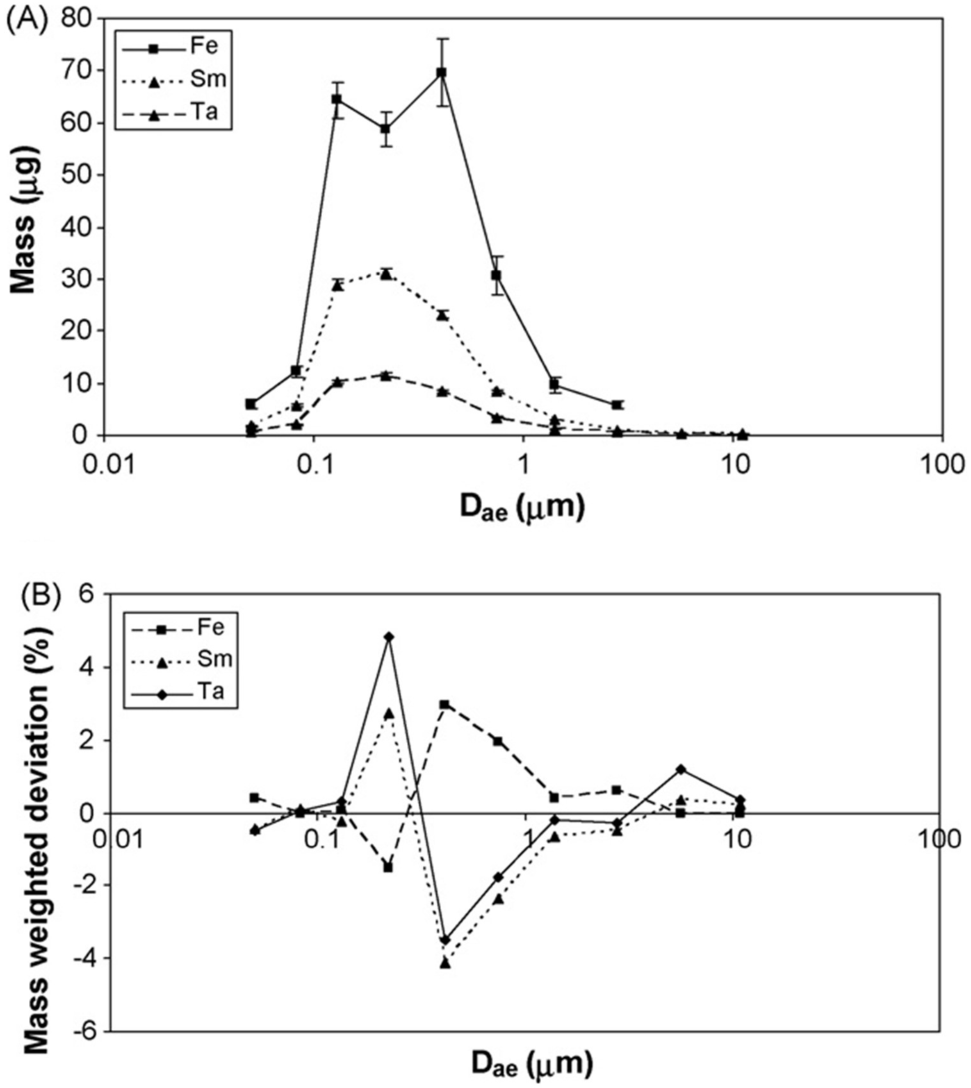

Figure 25: Mass size distributions (A) and mass-weighted deviations from the target composition (B) for Fe, Sm and Ta upon ablation of the Sm$_{13.8}$Fe$_{82.2}$Ta$_{4.0}$ target and size segregation in the cascade impactor. Since the target composition is not exactly identical to the average composition of the particles found, the graphs in (B) are slightly offset in the vertical direction (see the text for details). LA conditions: laser fluence, 9 J cm^{-2}; laser beam diameter, 100 µm; pulse rate, 10 Hz; scanning speed, 10 µm s^{-1}; He flow rate, 0.6 L min^{-1}. Error bars denote the uncertainty in the measurement.

3.1.6 Characterization of the material deposited in He

The dependence of the ablation parameters on the properties of the deposit was investigated using SEM, TEM, XRD and SQUID (Figure 26 - Figure 33). XRD provides macroscopic information, while TEM gives microscopic information regarding the crystal structure. SEM reveals details of the surface structure of the deposits and SQUID provides information on material coercivity.

The SEM micrographs of the material deposited at optimal PLD conditions: fluence of 9 J cm^{-2}; He gas flow rate of 0.3 L min^{-1}; target-substrate distance of 2 mm and deposition time of 30 min and 120 min are presented in Figures 26A and 26B, respectively. It can be seen that the layer growth is three-dimensional with particles forming clusters on the substrate. This so-called Volmer-Weber growth [88] occurs through the ripening and coalescence of clusters until eventually, a continuous layer is produced [88]. This type of island growth is the most common growth mode and prevails when the deposited material and substrate are composed of dissimilar materials, possess different crystal structures and chemistry, and no epitaxial relationship exists between them. In Figure 26A the coalescence process has not been completed yet due to a short deposition time (30 min), whereas in Figure 26B the deposition time of 2h suffices to produce a continuous layer. Zooming in on the deposit (Figure 26C) shows that besides nanoparticles, larger spherical particles of different sizes have also been formed.

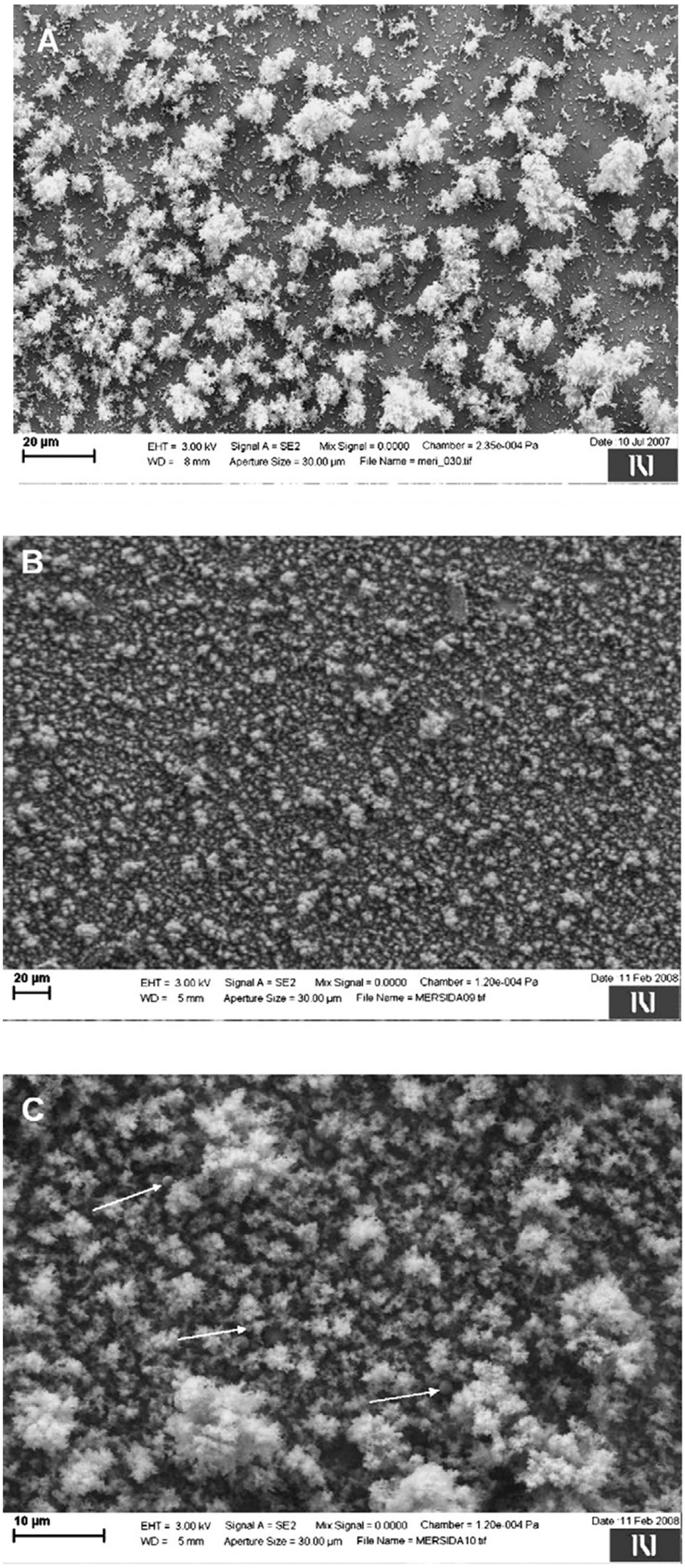

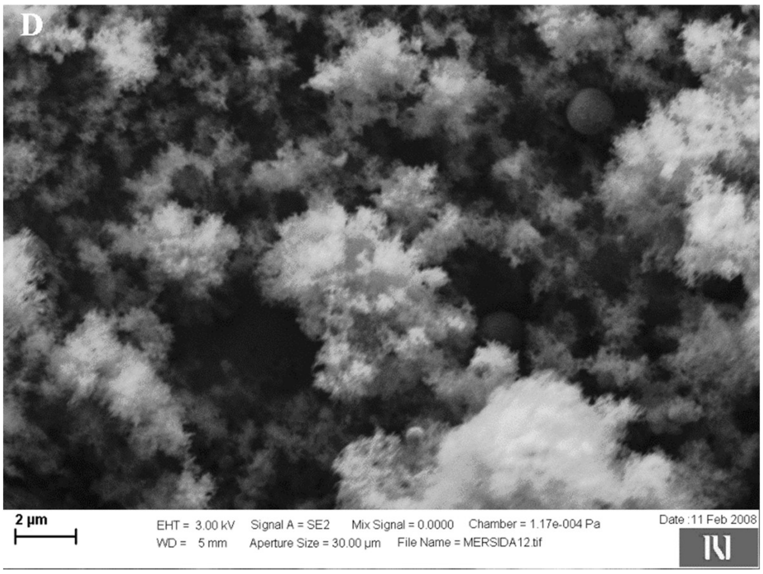

Figure 26: SEM images of particles deposited for (A): 30 min and (B): 2 h; (C): higher magnification of (B), (D): higher magnification of (C), some larger spherical particles of different sizes are indicated by arrows. For operational PLD parameters see also Figure 24.

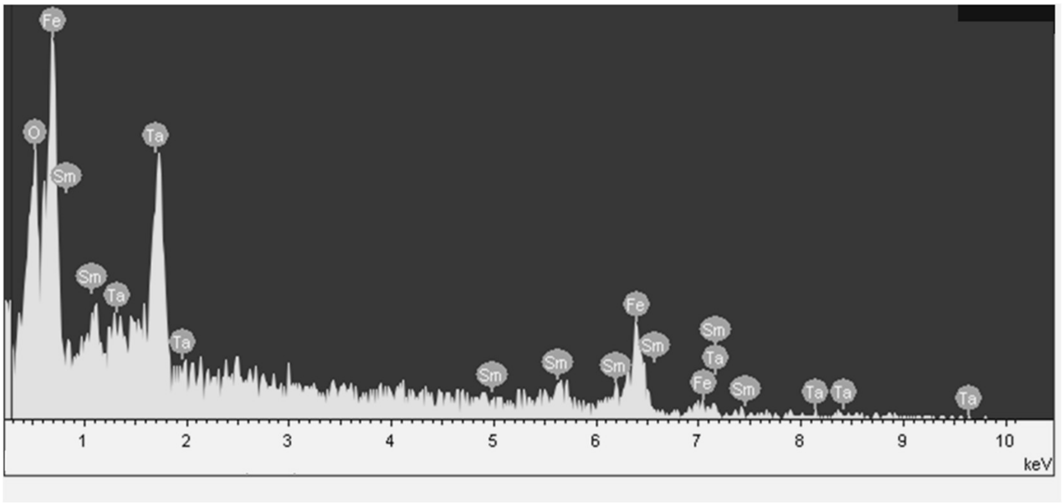

Figure 27: EDXS spectrum of larger particles (> 1 µm) rich in lower volatility Fe (Fe = 89 at. %; Sm = 5 at. %; Ta = 6 at. %).

From SEM-EDXS characterization measurements it follows that the Fe/Sm ratio in larger particles (> 1 µm) was in general, somewhat higher than in the target (Figure 27). This is in accordance with the cascade impactor findings for the fractions between 0.41 and 2.8 µm or higher (Figure 25B). The results seem to agree with the literature as far as mechanisms for formation of particles are concerned. Small particles are formed by nucleation and condensation from the vapour while larger particles may be ejected from the melted liquid due to hydrodynamic instability or recoil pressure from the expanding vapour plume [25]. The vaporization enthalpy of Fe is much higher than that of Sm, causing Sm to vaporize readily upon laser heating leaving a melted residue that is rich in lower volatility Fe. Hence, particles ejected from the melt are expected to have a higher Fe/Sm ratio than the target.

Figure 28: SEM image of particles with size distribution between 50 and 600 nm deposited on the substrate for 2 h.

The size distribution of the medium droplets was between 50 and 600 nm (Figure 28). EDXS analysis indicates that their composition is close to that of the target (Fe = 81 at. %; Sm = 14 at. %; Ta = 5 at. %) and that they are formed by nucleation and condensation from the vapour (Figure 29).

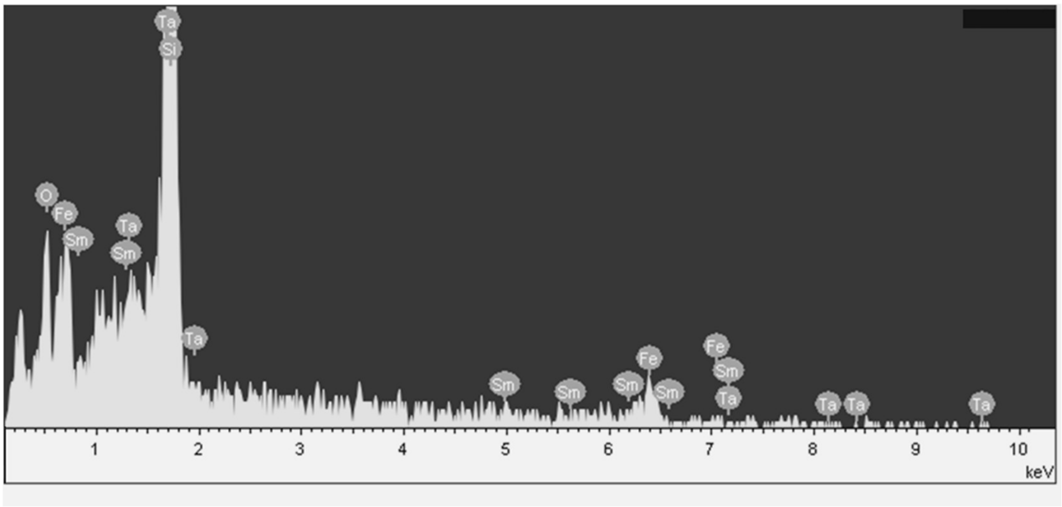

Figure 29: EDXS spectrum of smaller particles (50–600 nm) with composition similar to that of the target.

Transmission electron microscopy was used to characterize nanodroplets. Figures 30A and 30B are typical TEM micrographs of small-size Sm-Fe-Ta nanodroplets, deposited on the Si/Ta substrate for 2 h. The images show many grains of variable size and contrast. The difference in contrast results from varying directions of the diffraction of electrons, corresponding to the crystallinity of the grain. The size distribution of the nanodroplets was between 5 and 20 nm (Figures 30A and 30B).

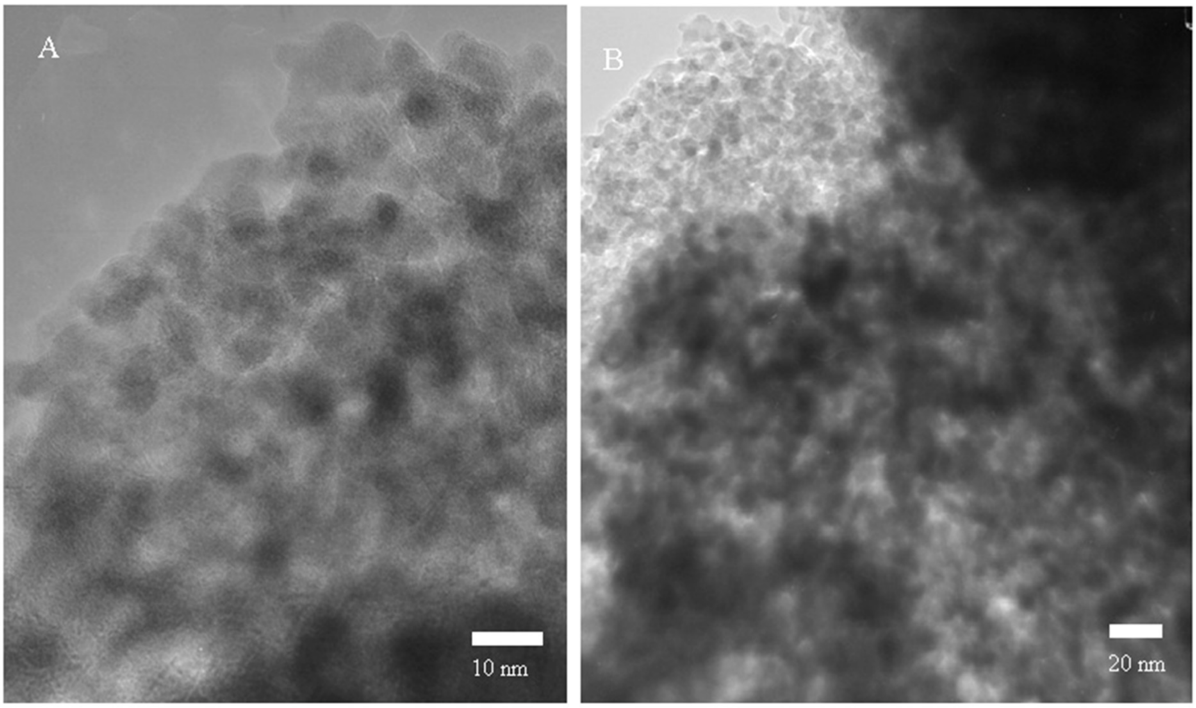

Figure 30: TEM images of particles with size distribution between 5 and 20 nm. For operational PLD parameters see Figure 24.

EDXS analysis (Figure 31) indicates that its composition varies from 71 to 78 at. % for Fe, from 25 to 17 at. % for Sm and from 4 to 5 at. % for Ta, respectively. This deviation in the elemental distribution of the nanodoplets produced by a 213 nm Nd:YAG commercial laser ablation-inductively coupled plasma mass spectrometer (LA-ICPMS) suggests that they are mainly formed in the plume.

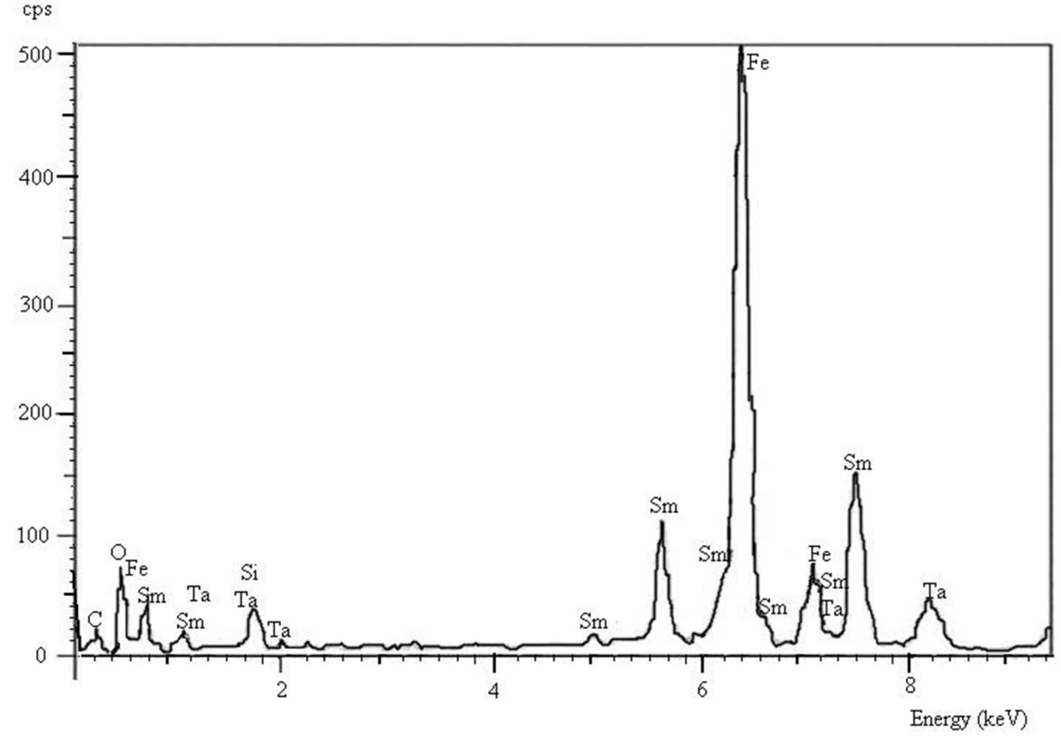

Figure 31: EDXS of nanodroplets shown in Figure 30.

It is generally known that laser ablated material consists not only of evaporated atoms, but also contain particles formed, either directly by laser-solid interaction or later through condensation in the expanding plume. Normally, condensation is used to explain the observation of small particles, composed of tens to thousands of atoms/molecules. Formation of larger (micrometer-sized) particles would require an unrealistically high number of collisions to occur in the expanding plume. Therefore, the larger particles are probably the result of direct ejection from the target.

For identification of crystalline phases in an as-deposited and annealed material, the X-ray diffraction technique was applied. In Figure 32 X-ray diffraction patterns are shown for the Si substrates coated with approximately a 100 nm layer of Ta and Sm-Fe-Ta-N material annealed in a vacuum (10^{-5} mbar) for 5 min at 680 ºC and then nitrogenized in a N_2 atmosphere for 2.5 h at 350 ºC.

It is clear that the sample before annealing and nitriding is amorphous. The reason for the amorphous structure can be the oxidation during the laser ablation, which is not possible to avoid, using LA-ICPMS system. The annealed and nitrided sample indicated the presence of soft phases which have negative influence on the magnetic properties. Formation of α-Fe, $SmFe_7$ and SmN phases can be due to the incomplete nitrogenization and nitriding for long time, which allowing disproportionation.

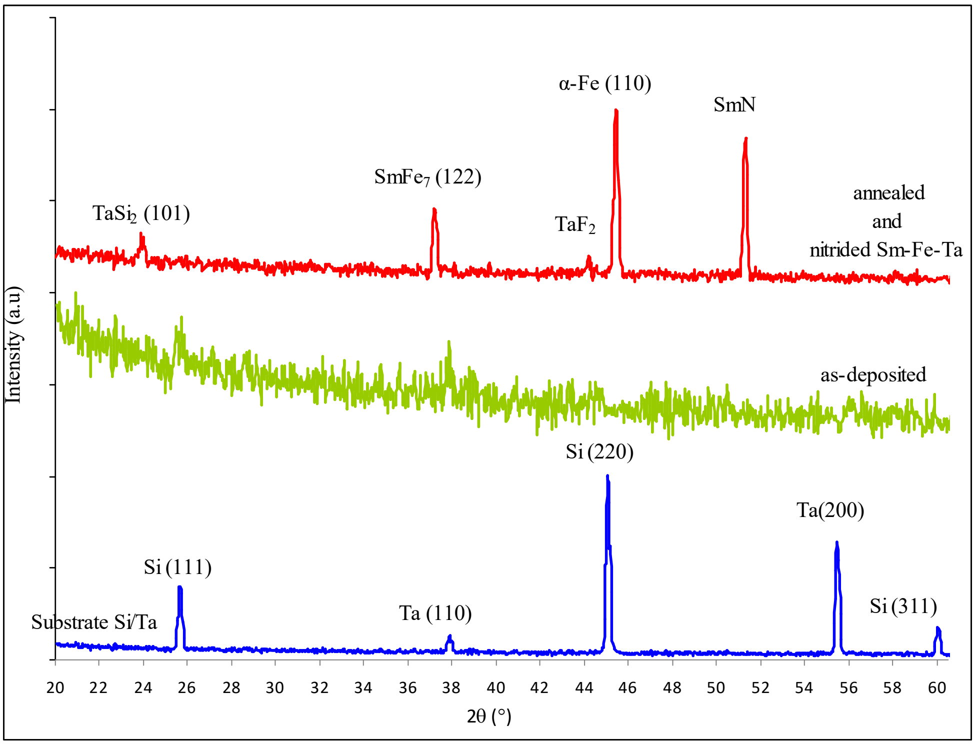

Figure 32: X-Ray diffraction patterns for the Si/Ta substrates and Sm-Fe-Ta-N deposited material.

Figure 33 shows the magnetic hysteresis loops obtained from the as-deposited Sm-Fe-Ta material deposited for 2 h on the Si/Ta substrate as well as from the annealed and nitrided samples. The as-deposited material was largely paramagnetic. The paramagnetic state can be due to the antiferromagnetic Sm–Fe exchange interaction and the random atomic occupation of Sm in a metastable solid-solution of Sm and Fe in the as-deposited material. When the as-deposited was annealed in a vacuum (10^{-5} mbar) for 5 min at 680°C and then nitrided for 2.5 h at 350°C, it became a soft ferromagnet, exhibiting a rise in magnetization and coercivity due to increased ferromagnetic Fe–Fe interactions. However, an H_C of ~ 100 Oe is too low compared to that of the bulk. One of the reasons for the low values can be the oxidation during the laser ablation, which was very difficult to avoid. Also the presence of α-Fe and $SmFe_7$ phases (Figure 32), might also be reason why the deposited material exhibited relatively low values of coercivity.

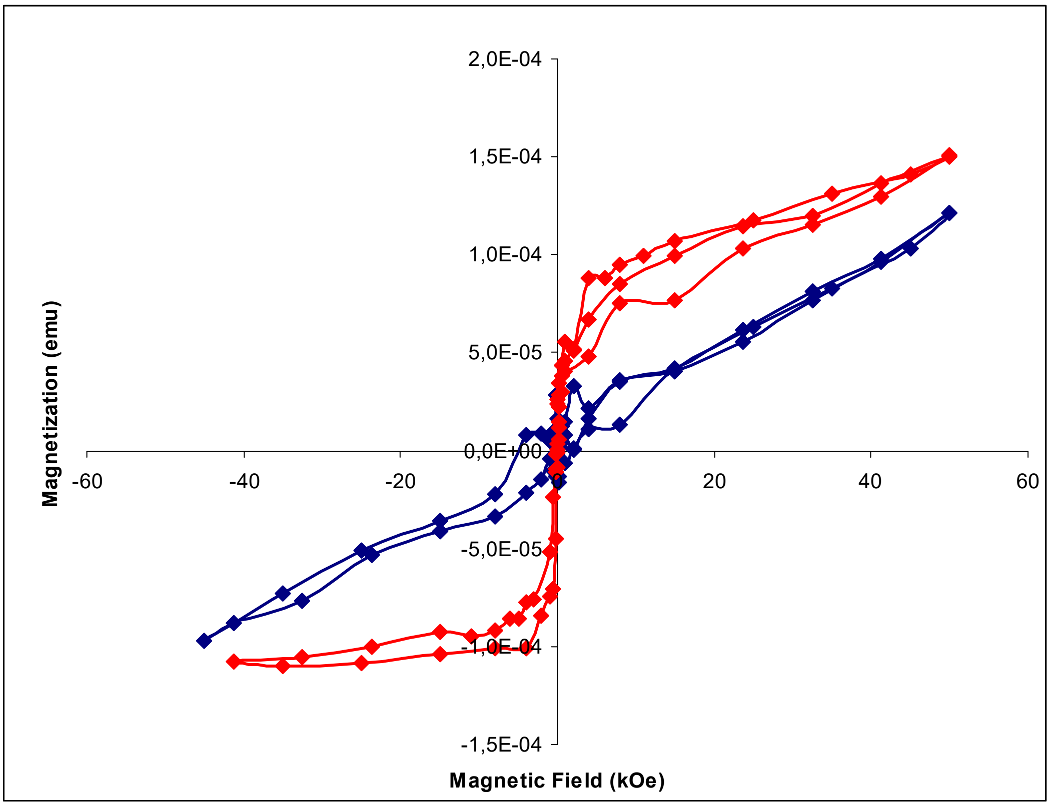

Figure 33: Magnetization curve of the Sm-Fe-Ta as-deposited (blue line), and post ablation annealed and nitrided material (red line) vs. the applied magnetic field.

3.1.7 Density and size distribution of particles generated in N_2

All the above mentioned experiments were performed in He atmosphere. Since the ambient parameters including the gas properties affect the formation of particles, this part of the research work was dedicated to investigating how the background gas influences density and particle size distribution. For that reason, experiments on the $Sm_{13.8}Fe_{82.2}Ta_{4.0}$ target were also carried out in N_2. He and N_2 have different physical properties such as thermal conductivity, molecular weight and first ionization potential which may influence the growth of particles condensing from a vapour. A 213 Nd:YAG ablation system was used in all the experiments with the following default settings: spot size, 100 µm; repetition rate, 10 Hz; line scan speed, 10 µm s^{-1}; deposition time, 30 min.

PLD parameters regarding the $Sm_{13.8}Fe_{82.2}Ta_{4.0}$ target and Ta-coated silicon wafer substrate were optimized for maximum particle density on the substrate (Table 3). The following parameters were varied to this end, in consecutive order: laser fluence, N_2 flow rate and target-substrate distance, one parameter at a time. The maximum elemental deposition of Fe and Sm for a specific parameter followed from elemental mapping of all the substrates for this parameter in a sequence of lines scans. After image analysis and quantification of the elemental amounts deposited, the optimized conditions were fed back prior to optimizing the next parameter.

The (sequentially) optimized parameters in N_2 atmosphere were (indicated in Table 3): laser fluence, 9.3 J cm^{-2}; gas flow rate, 0.0 L min^{-1}; target-substrate distance, 2 mm. Compared to ablation in He (Table 2, section 3.1.4), only the optimized gas flow rates were different. A static N_2 atmosphere (no gas flow) gave the best conditions compared to an intermediate He flow rate. This is probably due to the fact that He has a higher thermal conductivity than N_2, resulting in a significantly smaller laser-induced plasma [89], leading to a significant influence of the background gas flow rate on the deposition rate and density.

As in He atmosphere, the particles deposited in N_2 atmosphere are mainly spherically-shaped nanodroplets (Figure 34). Since N_2 has a lower thermal conductivity than He this may lead to a slower removal of thermal energy away from the laser induced plasma, resulting in slower condensation and yielding larger particles.

Table 3: Relative concentration densities of Fe and Sm deposited on the Si/Ta substrates in N_2 at atmospheric pressure.

Fluence (J cm^{-2})	Fe (rel. dens.)	Sm (rel. dens.)
S1: 1.7	19.6	30.81
S2: 3.9	44.4	53.03
S3: 6.1	74.8	83.33
S4: 9.3	**100**	**100**
N_2 flow rate (L min^{-1})	Fe (rel. dens.)	Sm (rel. dens.)
S1: 0.00	**100**	**100**
S2: 0.28	96.57	81.93
S3: 0.56	90.34	72.59
S4: 0.82	45.17	35.54
T-S distance (mm)	Fe (rel. dens.)	Fe (rel. dens.)
S1: 2	**100**	**100**
S2: 3	50.1	51.56
S3: 4	2.2	1.08

On the other hand, Dyer et al. [41] investigated the influence of the target-substrate distance, i.e. length of the plume on the particle density distribution. If the target-substrate distance is bigger than the length of the plume, the adhesion of ejected particles to the substrate will be poor, but if the target-substrate distance is smaller than the length of the plume, the particle density will be higher.

The differences in the particle densities on the samples deposited in two different gas backgrounds can be attributed to the significantly different lengths of laser-induced plasma in He and N_2 atmosphere. Observations show that the length of the laser-induced plasma plume in He is significantly smaller than in N_2, because of higher He thermal conductivity [89]. This means that the laser-induced plasma plume in N_2 atmosphere (lower thermal conductivity) will be much longer compared to He (higher thermal conductivity), resulting in higher particle density distribution (see Tables 2 and 3).

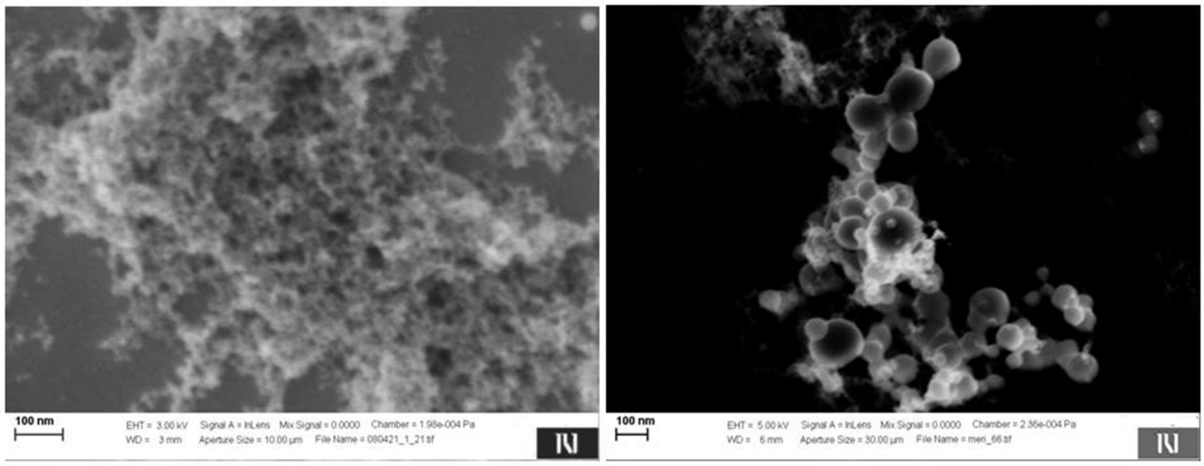

Figure 34: SEM image of the Sm-Fe-Ta deposition patterns in N_2 atmosphere.

3.2 Fabrication of crystalline/amorphous bi-phase Sm-Fe-Ta-N magnetic nanodroplets by PLD at 157 nm

Magnetic nanodroplets have drawn much attention recently due to their potential use in magnetic recording as well as many biological and medical applications. The core-shell nanostructures attract special attention because their applications are limited by their resistance to oxidation. Following the requirements of applications, the study focused on the synthesis of core-shell nanodroplets with a combination of different laser ablation parameters and conditions (laser energy, target-substrate distance and ablation geometry). The research concentrated on studying the structural and magnetic properties of bi-phase Sm-Fe-Ta-N nanodroplets dependence on the target-substrate distance and size distribution, the stochiometry and morphology dependence on the laser fluence and ablation geometry. The thermodynamics of nucleation and growth processes of nanodroplets were also studied in detail.

The study provides a more profound understanding of the laser ablation process of magnetic Sm-Fe-Ta-N materials at 157 nm and correlates such results with the influence of the ablation conditions on the subsequent deposition process of core-shell nanodroplets.

3.2.1 Growth and characterization of bi-phase Sm-Fe-Ta-N nanodroplets

The PLD parameters influence the plasma, the kinetic growth characteristics, composition and structure of the deposited material. The stoichiometry of the plasma and the grown particles are related; one of the parameters influencing the growth rate, the size and composition of the nanoparticles is the target-substrate distance.

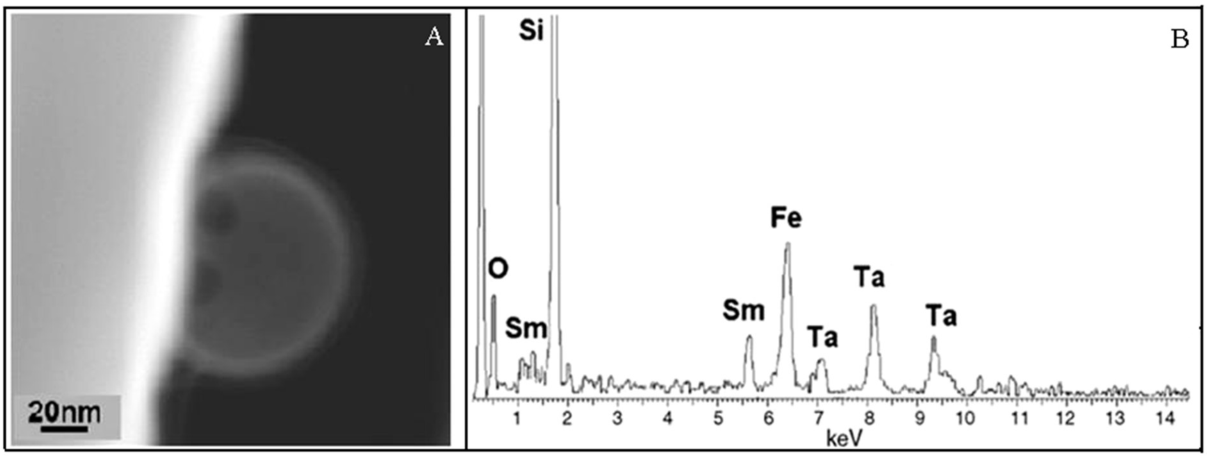

Figure 35: (A) STEM/HAADF (scanning transmission electron microscopy with high-angle annular dark-field) image of the droplet deposited at 10 mJ and a 1.5 cm target-substrate distance. The dark area in the droplet at the interface with the substrate corresponds to crystallization of the amorphous droplet due to rapid cooling. (B) EDXS analysis of droplet in Figure 35A [83].

TEM investigations of Sm-Fe-Ta-N material deposited by 157 nm showed that bi-phase spherical nanodroplets with 50–100 nm in diameter consist of a 5–10 nm crystalline nucleus surrounded by an external amorphous phase. (Figure 35A and Figure 36A). These nanocrystals are formed due to the high cooling rate on the Si/Ta substrate [83]. The probability of nanocrystal formation inside the droplets is exponentially proportional to the square of the temperature difference between the droplets and the substrate [90], meaning that a lower substrate temperature contributes to a higher cooling rate; we can anticipate that the formation of nanocrystals inside the droplets is due to the rapid cooling rate because of the lower substrate temperature.

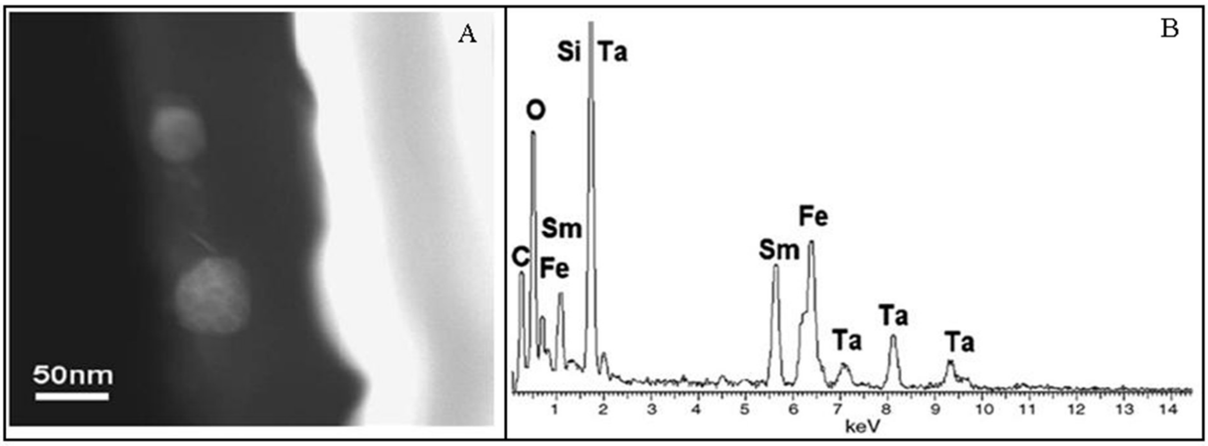

Figure 36: (A) STEM/HAADF image of the droplets deposited at 10 mJ and a 0.5 cm target-substrate distance. The dark areas correspond to the many nanocrystalline nucleation sites. (B) EDXS analysis of

droplets in Figure 36A [83].

The EDXS spectra of the droplets deposited using a laser energy of 10 mJ and target-substrate distances of 1.5 cm and 0.5 cm are shown in Figures 35B and 36B, respectively. The composition of the droplets grown at a 1.5 cm target-substrate distance approximates that of the target, while the composition of the droplets grown at a 0.5 cm distance between the target and substrate was too rich in Sm.

The compositional variations in the multicomponent deposit dependence on the distance between the target and the substrate can be attributed to varied element scattering in the reactive gas ambient. A background gas of a sufficiently high pressure scatters Fe atoms preferentially because they are lighter than Sm atoms. During the plume expansion in a background gas, preferential propagation of the heavy atoms (Sm) along the normal occurs, usually in the direction of the substrate [91]. For the given laser fluence and deposition time, more non-stochiometric material can be deposited at a shorter target-substrate distance because of a higher concentration of heavier ablated species near the target [92]. It was also proposed that the kinetic energy of the ablated species increases if the distance between the target and substrate is decreased, so smaller distances can enhance lattice damage by the high energy particles, which deteriorates the crystallinity [93].

The magnetization curve, which describes the magnetization behaviour of the Sm-Fe-Ta-N nanodroplets deposited using 10 mJ laser energy and a 1.5 cm distance between the target and the substrate, is shown in Figure 37. The coercivity of the as-deposited material was 2.5 kOe. This significant value of coercivity can be attributed to the nitrogenation process, which started in the plume prior to annealing and nitriding [83]. After annealing for 5 min at 680 °C in vacuum (10^{-6} mbar) and nitriding for 2.5 h at 400 °C, the coercivity increased to 5.0 kOe.

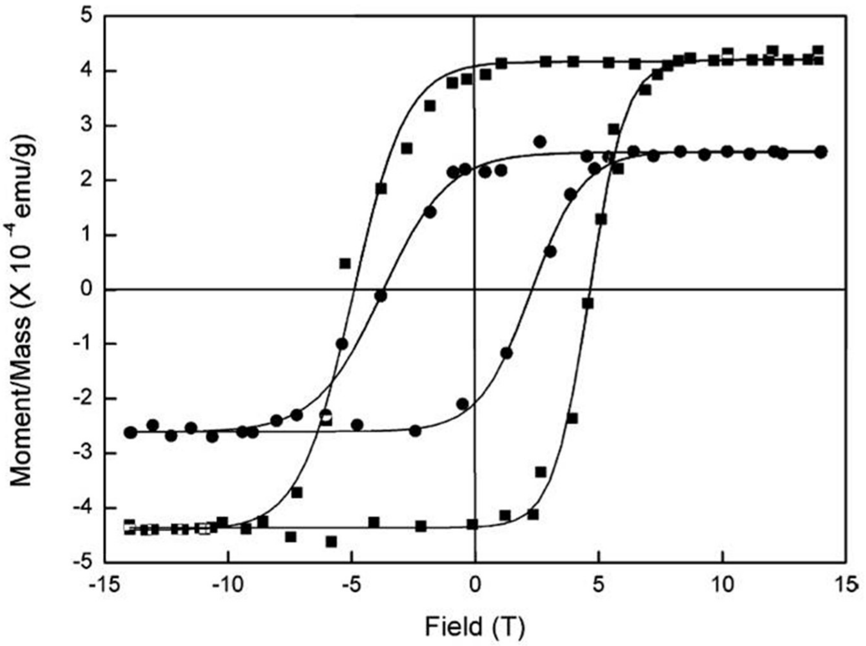

Figure 37: Magnetization curves vs. the applied magnetic field. The deposited material exhibits a ferromagnetic response at room temperature with a coercivity of 2.5 kOe and postablation annealing and nitriding increasing the coercivity to 5.0 kOe [83].

Thus far, it appears that PLD at 157 nm is the only efficient method today capable of creating crystalline nitride nanodomains that exhibit magnetic response. This is mainly due to the fact that high energy of 7.9 eV per photon efficiently ionizes both the metals and the nitrogen molecules to form metal nitrides from the excited electronic states rather, than the ground electronic states the chemical methods use. The excited metallic and nitrogen ions interact far more efficiently to create nitrides through harpoonic (ionic) reactions than covalent ones from the ground or excited electronic molecular states. The formation path of nitrides via excited ionic states, bypasses the constrain of low dissociation energy of the ground electronic states of nitrides, that makes their formation inefficient. Following the formation of the metal nitrides in the gas phase, subsequent cooling of plasma in the plume leads to crystallization in that phase which is more favored in terms of energy and entropy for that particular temperature and pressure. It seems therefore that the crucial 2:17 structure is the most favored one thermodynamically compared to other structures.

Certain rare-earth transition metal compounds contain order–disorder transformations from the disordered $TbCu_7$-type structure to the ordered Th_2Zn_{17}-type structure [94]. In the Sm–Fe system, formation of Sm_2Fe_{17} structures, depend on Sm content and temperature. In the Sm–Fe system, the ordering temperature is much higher than 1300°C [95] and solidification processing results in the formation of the ordered Sm_2Fe_{17} structure. Fe nuclei are formed in the plume during the initial stage of solidification. These Fe nuclei react with Sm in the plume to form longe-range ordered Sm_2Fe_{17} structure. The improvement of magnetic properties is due to intrinsic differences in the magnetic anisotropy between the ordered and disordered states. This relationship of the coercivity with the long-range order parameter indicated that coercivity is controlled by domain wall pinning by antiphase boundaries [96].

The magnetic properties of Sm-Fe alloys are volume-sensitive, with a critical interplay between structure and magnetism. Sm_2Fe_{17} have interstices in their structure which can be occupied by nitrogen with dramatic consequences for the magnetic properties and the nitrogen, as an interstitial impurity, tends to dilate the host lattice [67]. A volume expansion of the latice reduced the 3d-3d overlap and hence the bandwidth, which tends to make Fe a strong ferromagnet. The nitrogen N sp as a nearest neighbour of the 3d states of the Fe reduces the spin splitting, and especially lowers the potential for 3d electrons. There is then charge transfer from the more distant Fe, predominantly from 3d to 3d states. This depletes the 3d band of the strongly ferromagnetic distant neighbours, and increases their magnetic moment [76].

The Sm_2Fe_{17}, without interstitial modification are uselessed as permanent magnet materials; the Curie temperature is close to room temperature, magnetisation is low and magnetocrystalline anisotropy is planar. Nitrogenation dramatic enhances the Curie temperature and magnetisation and changes the sign of the room temperature magnetocrystalline anisotropy. The transformation for $Sm_2Fe_{17}N_3$ is dramatic, with the planar anisotropy becoming strongly uniaxial. The large magnetocrystalline anisotropy for $Sm_2Fe_{17}N_3$ is due to the combined effect of the prolate shape of the Sm 4f shell, the negative crystal field charge of nitrogen and the in-plane coordination of the interstitial 9e site [76]. The mixture of fully nitrided and nonnitrided material is present at all stages of the nitrogenation process [97] and there is a tendency to form core and shell structures in partly nitrogenated particles.

The shape of the M-H loop reveals the formation of typical magnetic dots of less than 100 nm in diameter, which is the characteristic of a single-domain behavior [98]. The double saturation magnetization implies that there is an enhanced number of crystalline magnetic nanodomains per unit volume. Annealing and nitridization implies that the film is optimized in terms of nitrided molecules and crystalline phases. This is expected as nitridization in the plume should be unoptimized due to the fluctuations of temperature and pressure that is natural to lead to large fluctuations of concentration of molecular nitrides.

The enhancement of remanence has been due to producing a coherent nanocrystalline $Sm_2Fe_{17}N_3$ structure. The $Sm_2Fe_{17}N_3$ materials can be considered as systems of interacting single-domain particles where the type and strength of the interaction is controlled by the structure and the composition of the particles. The single domain particles stay in a single domain state for all magnetic fields and their saturation remanence is consistent with the single-domain state. During the demagnetization the magnetic moment cannot be reduced, instead, it can only change direction or rotate toward the applied field. The single-domain particles are resistances to the rotation of magnetisation and are very efficient carriers of remanent magnetisation [99].

The saturation magnetisation decreases with particle size. This can be due to spin canting which results from a magnetic ordered core surrounded by a disordered surface layer [100-103].

Since the coercivity is one of the most important properties of magnetic materials and one of the conditions under which ferromagnetic materials are used in the practice, the high value of 5.0 kOe suggests that the deposited material can be used for application in magnetic nanodevices.

The ferromagnetic response and high coercivity can be attributed to the magnetic dipole interactions in the nanodroplets, which are the most relevant interactions and are always present in the system of small particles. They are of long-range character in the nanosize droplets, for which the thermal energy is lower than the magnetic anisotropy energy at room temperature. The enhancement of the magnetic anisotropy can be attributed to the induced surface strain during the rapid cooling of the liquid nanodroplets on the substrate surface and formation of nanocrystals with appropriate stechiometry [83].

AFM measurement of the surface topography of the Sm-Fe-Ta-N layer consisting of nanodroplets is shown in Figure 38. The layer appears to exhibit significant roughness, showing a variation in height of ~80 nm. The AFM image shows the presence of nanodroplet islands of different shapes, which are closely spaced and indicates a low porosity layer exhibiting nanodroplet island growth.

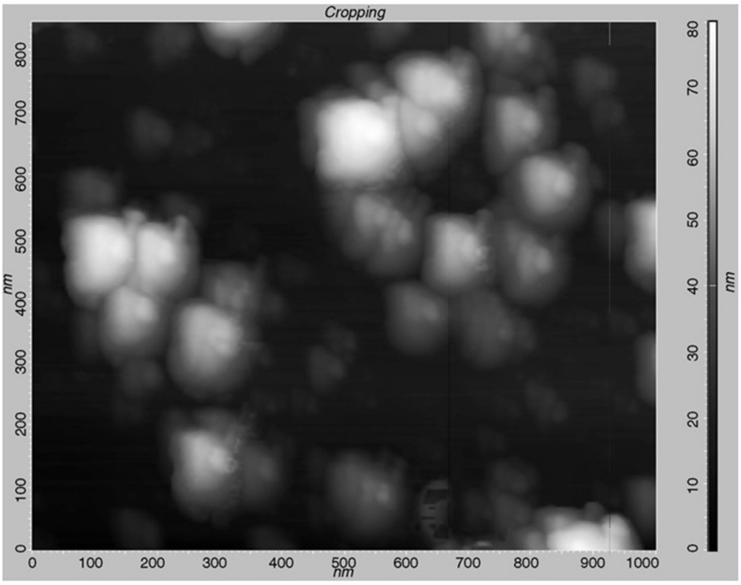

Figure 38: An AFM image of a part of the deposit surface. The deposit consists of monolayer nanodroplet islands of different shapes closely spaced with an average size of 300 nm. The AFM profile shows that the average size of each nanodroplet is ~ 50 nm [83].

Furthermore, X-ray photoelectron spectroscopy (XPS) for additional characterization of bi-phase nanodroplets was used. The XPS method was used to identify all elements in the nanodroplets, especially the N spectral peak, which could not be demonstrated using other techniques such as EELS and EDXS, because of the overlap with the Ta peak and thickness of our sample [83]. For the EELS analysis, the thickness of the samples should only be a few nm.

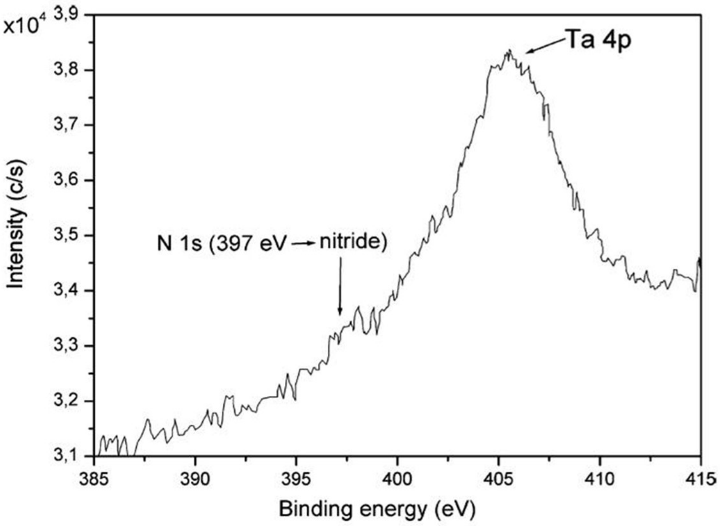

Figure 39: The XPS spectrum of the deposit surface [83].

The XPS method has the advantage of high surface sensitivity, enabling 3–5 nm thick layers to be analyzed with the 400 µm electron beam profile. The nitrogen content was demonstrated using this method, despite the fact that the Ta and N spectral peaks overlapped.

The XPS spectrum of the layer surface in Figure 39 shows that the N 1s peak is identified at 397 eV. The peak at 397 eV, the spectral signature of nitrides, indicates that nitride was already formed in the plume prior to any additional nitriding of the sample [83].

Since the oxygen deteriorates the magnetic properties of Sm-Fe-Ta-N nanodroplets, the degree of oxidation of nanodroplets was evaluated during the ablative process doing depth profile analysis of a nanodroplet layer.

The results of this analysis, which was performed in high vacuum (2 x 10^{-8} Pa) are shown in Figure 40 and indicate that the layer was oxidized only 10 nm in depth. This oxidized amorphous phase on the surface enclosed the nanocrystals inside the droplets and protected them from further oxidization [83].

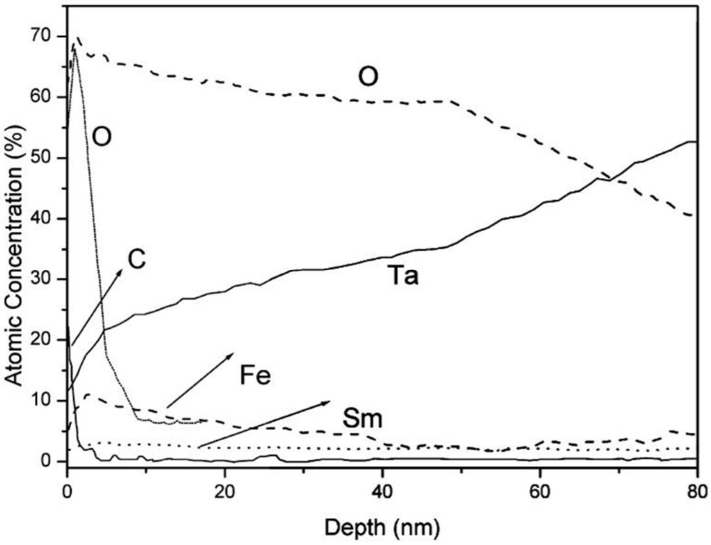

Figure 40: XPS depth profile of deposit of various elements. The upper trace of oxygen corresponds to areas of high oxidization. The lower trace of oxygen corresponds to 90 % of deposit areas of low oxidization [83].

3.2.2 Clustering and morphology of core-shell Sm-Fe-Ta-N nanodroplets grown at 157 nm

The deposit morphology in the PLD experiments depends on the laser energy. The laser energy has the most significant effect on stoichiometry transfer, particle size and density. The laser energy necessary for stoichiometric ablation has to be higher than a certain threshold value. In the case of PLD, a stoichiometry transfer between target and substrate can be obtained when rapid and strong heating of the target surface with high energy photons ensures that all target components evaporate at the same time. On the other hand, too high laser energy may result in the formation of cones, cracks, craters and columnar structures on the target surface and as a result, particles with undesireable sizes and properties may form [34].

The irradiation of the target material with high energy photons ejects highly ionized atomic species from the target in the plume, which collide with background gas species. The collision effects might be expected to form crystal nanostructures or hot liquid droplets, which further agglomerate in the plume. The formation of nanocrystalls versus liquid droplets is governed by the thermodynamic conditions, and the pressure and temperature during the nucleation [104].

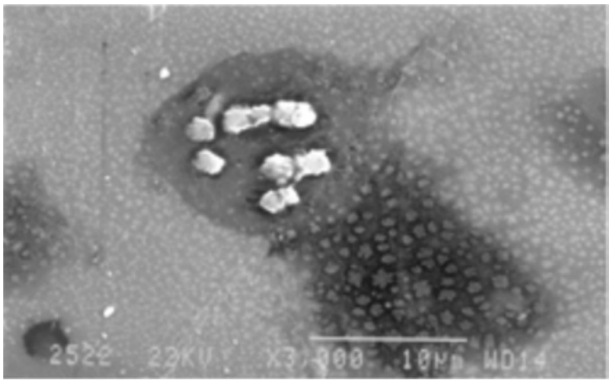

Figure 41: SEM image of the surface morphology of deposits grown at 50 mJ [104].

At higher laser energy (50 mJ), the formation of crystal structures dominated over the spherical nanodroplets, while the situation was quite different for lower laser energy (20 mJ), where the nanodroplets dominated [104]. The material, deposited at 157 nm on the substrate at a distance of 1.5 cm from the target, consisted of asteroids (Figure 41) and long structures (Figure 42). These structures were formed from agglomeration of single nanocrystalline domains and were observed for the higher laser energy (50 mJ). It seems that the local temperature and pressure in the plume have the right values for the system to pass from the gas phase to the solid and crystal one. Such crystal structures can be highly oxidized due to the porosity and large surface area for a given volume [104].

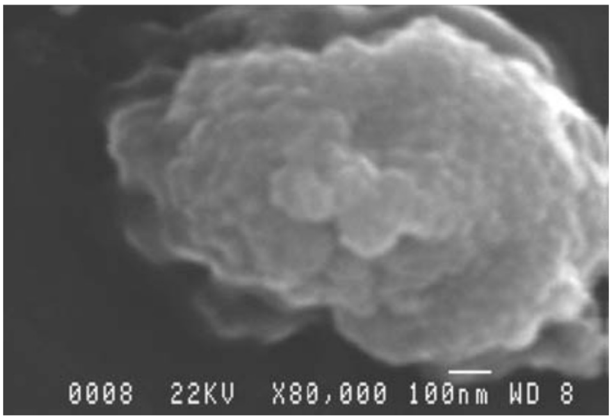

Figure 42: Sm-Fe-Ta solidified long structures formed from agglomeration of single nanocrystallic domains [104].

At laser energy of 20 mJ and distance of 1.5 cm between the target and the substrate, the deposited material consisted of droplets larger than 50 nm (Figure 43) with the same composition as the target and smaller nanodroplets displaying a large deviation in the elemental distribution (Figure 45) [104]. Since the collisions between the ablated particles and the background gas species scatter the plume particles from their original directions thereby broadening the angular distribution, the concentration and morphology of nanodroplets were analyzed in three different directions. One was opposite to the direction of the laser beam (180°) and the other two perpendicular to the laser beam and opposite each other, i.e. 90° and 270°. In this way, by analyzing the nanodroplets, the directional and diffusional effects in the plume were taken into consideration.

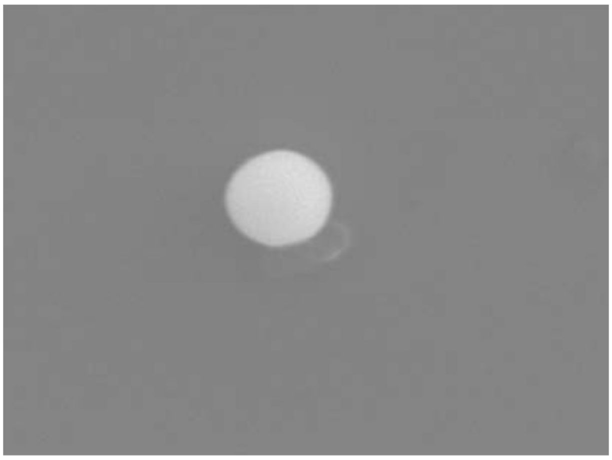

Figure 43: SEM image of a large size nanodroplet (500 nm diameter) [104].

Nanodroplets larger than 50 nm were deposited by more than 80 % in the direction opposite to the laser beam (180°) than in the other two perpendicular directions (90° and 270°). These large size nanodroplets have a rather anisotropic distribution along the directions at 90° and 270° and isotropic distribution along the direction at 180° [104].

The average concentrations of Fe, Sm and Ta were 79 %, 19 % and 2 %, respectively (Figure 44) with a RMS deviation of ± 2 % for Fe and Sm, respectively [104]. Taking into consideration the directional distribution and the fact that the elemental concentration of larger nanodroplets approximated that of the target, it was concluded that they were mainly ejected from the solid target.

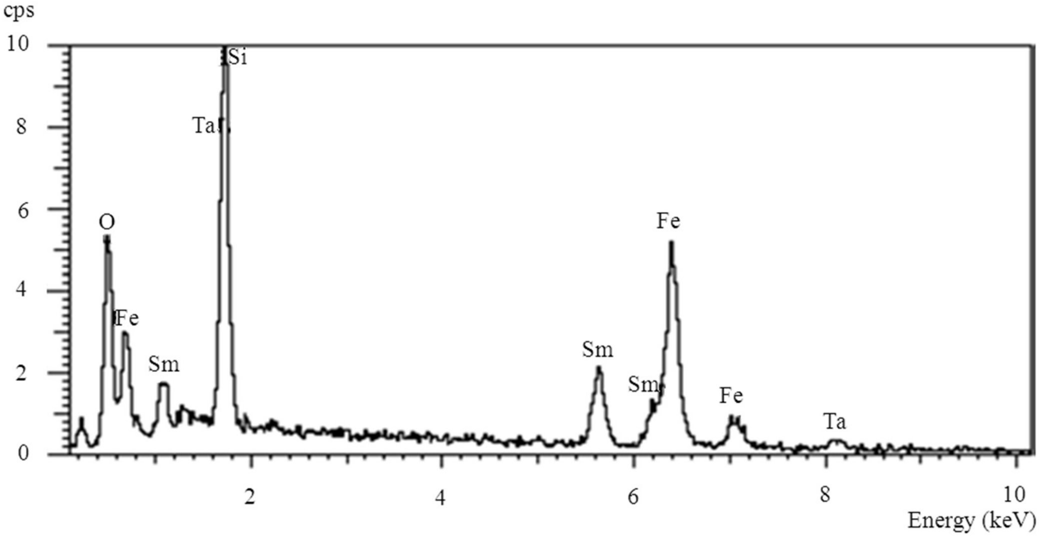

Figure 44: EDX spectrum of a large size nanodroplet (Figure 43) with a composition similar to the target′s [104].

On the other hand, the smaller nanodroplets (Figure 45) displayed a large deviation in the elemental distribution. The average elemental concentration of Fe, Sm and Ta was 58 at. %, 24 at. %, and 18 at. %, respectively and the RMS deviation for Fe, Sm and Ta was 17 %, 9 % and 2 %, respectively as seen in Figure 46 [104]. This large deviation in elemental distribution suggests that smaller particles predominantly originate from nucleation in the plume.

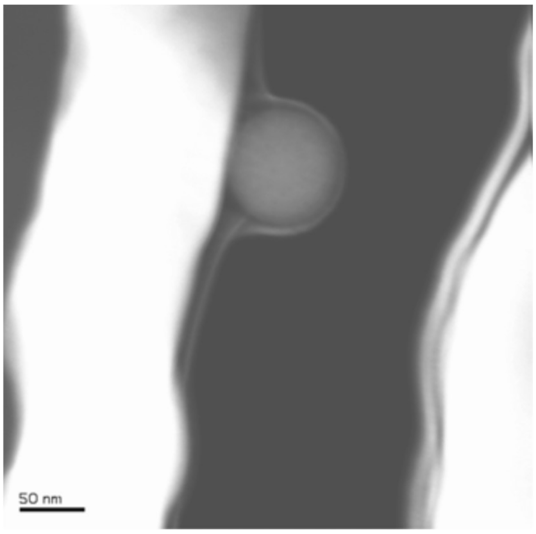

Figure 45: TEM image of a 44 nm medium droplet solidifying on the Si/Ta substrate, attached at a small contact angle [104].

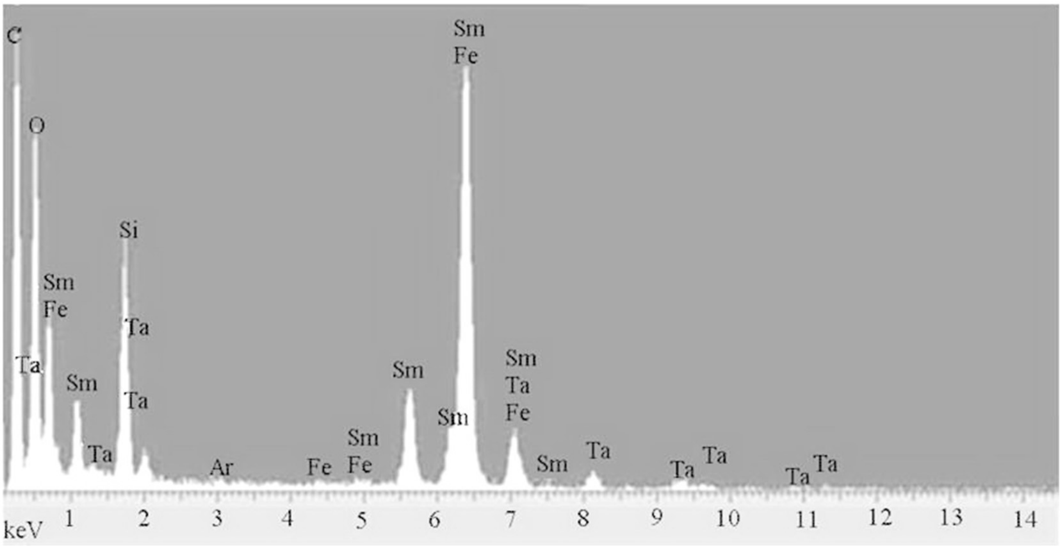

Figure 46: EDX spectrum of the droplet of Figure 45. The concentration of Sm and Fe in small droplets exhibits large variations, suggesting that they are formed in the plume [104].

A greater understanding of the fundamental physical and chemical processes controlling nucleation is essential to allow nanoparticles with desired properties to be created (size, shape, composition, morphology, etc.) The free energy of droplet formation is determined by the relative thermodynamic stability of small precritical droplets [105]. The nucleation process requires the free energy barrier to be overcome as a function of droplet size. However, nucleation is a dynamical process with the central quantity of interest lying in the nucleation rate, which is determined by competition of droplet evaporation and growth. Therefore, it is not sufficient to simply understand the droplet thermodynamics involved in the nucleation process, but an understanding of the kinetics of droplet condensation and evaporation is needed as well.

Nucleation of the liquid phase from a supersaturated vapour phase is an activated process that involves the formation of a critical nucleus of a thermodynamically stable liquid-like embryo within the metastable vapour phase. The free energy of the formation of the critical nucleus is determined by the free energy gain due to the formation of the liquid droplet and free energy loss due to the creation of the gas-liquid interface [106]. According to the classical nucleation theory (CNT), the total free energy of a droplet formed in a supersaturated vapour phase contains two terms: the first being the ‘bulk’ term that expresses the fact that the liquid is more stable than the supersaturated vapour which is negative and proportional to the volume of the droplet. The second is a ‘surface’ term that takes into account the free-energy cost of creating a liquid-gas interface which is positive and proportional to the surface area of the droplet. According to CNT, the total (Gibbs) free-energy estimation to form a spherical droplet with radius *r* is [104]:

$$\Delta G = \frac{4}{3}\pi r^3 N\Delta\mu + 4\pi r^2\sigma \qquad (17)$$

where *N* is the number-density of the solid or concentration of molecules per unit volume, $\Delta\mu$ the difference in chemical potential of the liquid and the gas and σ the liquid-gas interfacial free energy. The maximum of the free-energy gives the critical size of the nucleus r^*, i.e.

$$\frac{d(\Delta G)}{dr} = 0 \qquad (18)$$

Using equation (17), equation (18) becomes:

$$4\pi r^{*2} N\Delta\mu + 8\pi r^*\sigma = 0 \quad \text{or} \quad N\Delta\mu = -\frac{2\sigma}{r^*} = \Delta G_0 \qquad (19)$$

The free energy barrier $\Delta G*$ is given by the following expressions:

$$\Delta G^* = -\frac{4}{3}\pi r^3 \frac{2\sigma}{r^*} + 4\pi r^2\sigma \quad \text{or} \quad \Delta G^* = \frac{4}{3}\pi\Delta G_0\left(r^3 - \frac{3}{2}r^* r^2\right) \qquad (20)$$

where ΔG_0 is the bulk free-energy per unit volume of gas phase changing to liquid phase and:

$$\Delta G_0 = N\Delta\mu \qquad \text{or} \qquad \Delta G_0 = \frac{n}{V} RT \ln \frac{c}{c_0} \tag{21}$$

where $n = \frac{m}{M}$ is number of molecules in a mass m of a pure material having molecular weight M, $V = \frac{m}{\rho}$ is the volume of the droplet and:

$$\Delta\mu = RT \ln \frac{c}{c_0} \tag{22}$$

where c is the concentration of one of the elements in the droplet solution and c_0 is the concentration of the standard solution and bulk free energy is given by the relationship:

$$\Delta G_0 = \frac{\rho RT}{M} \ln \frac{c}{c_0} \tag{23}$$

Droplets smaller than the critical radius will become unstable because their size will be constantly decreasing with decreasing free energy, until finally they vanish. Droplets with a radius larger than the critical will continue to grow with decreasing energy. The size of the droplets then stabilizes around their critical value. On the other hand, as the concentration of the elements in the plume is subject to variation, the critical radius will be strongly dependent on ΔG_0 [104]; see equations (19) and (23).

The probability $W(r)$ for the formation of a crystalline nanodroplet with radius r will depend exponentially on the free energy barrier ΔG^* that is required to form such a droplet:

$$W(r) = \exp\left(-\frac{\Delta G^*}{k_B T}\right) \tag{24}$$

where T is the absolute temperature and k_B is the Boltzmann's constant.

$$\ln W(r) = -\frac{\Delta G^*}{k_B T} \tag{25}$$

Using equations (20), equation (25) becomes:

$$\ln W(r) = \frac{4\pi\Delta G_0}{3k_B T}\left(\frac{3}{2} r^* r^2 - r^3\right) \tag{26}$$

Therefore the probability distribution of nanodroplets of radius r is a logarithmic function of r, σ and ΔG_0. The size distribution of the nanodroplets will be exponentially dependent on the elemental concentration c (equation 23). From equation (26), the size distribution of nanodroplets attains its maximum value at r^*. The average size distribution of nanodroplets for the present experimental conditions is ~ 7.5 nm (Figure 47). Therefore the critical radius r^* of the nanodroplets is ~ 7.5 nm.

Figure 47: Morphology of a deposit consisting of agglomerated nanodroplets with a ~ 15 nm diameter [104].

Taking into consideration the experimental value of alloy density, 8.7 g cm^{-3}, the volume free energy of the nanodroplets (equation 23) is ~15.5 J cm^{-3}. Therefore the surface energy per unit area of the liquid nanodroplet is 5.8 μJ cm^{-2}. The theoretical values of alloy density (8.2 g cm^{-3}) and volume free energy (14.6 J cm^{-3}) were somewhat different from the experimental values, indicating that the target is inhomogeneous and has a higher concentration of the heavy element (Ta).

TEM investigations show core-shell spherical nanodroplets with different sizes. From the TEM image, one can identify four different cores with average radius of 2 nm inside the larger single nanodroplet (~ 31 nm) and a few smaller nanodroplets with ~ 9–15 nm in diameter (Figure 48). The EDXS SEAD (selected area diffraction) pattern in Figure 49 shows that the crystalline embryos in the larger nanodroplet are surrounded by the amorphous shell. It is important to mention that the average size of the crystallites is comparable to the critical radius of the nanodroplets (~ 7.5 nm). This is because bulk free-energy per unit volume ΔG_0 should be of the same order of magnitude for both the liquid and solid phases.

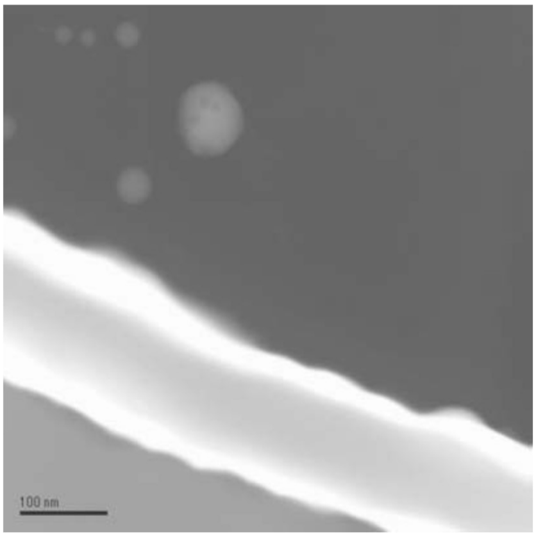

Figure 48: Typical TEM image of a single ~ 31 nm nanodroplet and a few smaller ~ 9–15 nm droplets. Four different 4 nm Sm-Fe-Ta-N nanocrystallites were formed inside the larger nanodroplet, which are surrounded by the amorphous material [104].

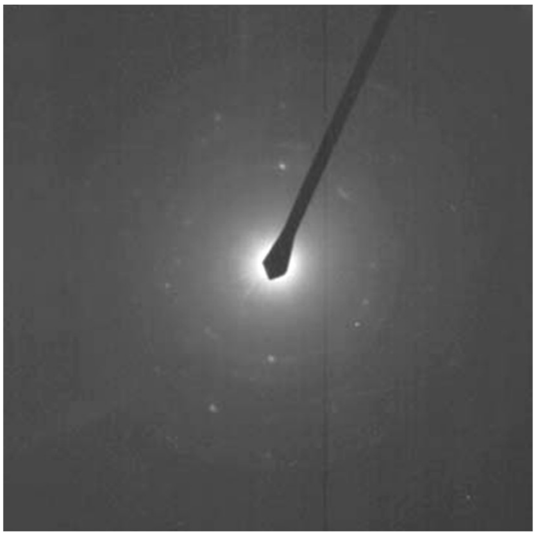

Figure 49: Diffraction pattern of the nanodroplet of Figure 48, where the crystal structure of the embryos is verified [104].

Based on the contact angles between the nanodroplets and substrate, how the droplets were formed can be deduced [104]. The TEM images in Figure 50 clearly indicate the core-shell nanodroplets attached to the Ta substrate with small (zero) and larger contact angles. The nanodroplets attached on the substrate at small (zero) contact angles were formed in the plume due to the homogeneous nucleation and then deposited on the substrate. On the other hand, the nanodroplets attached on the substrate at larger contact angles were formed as a result of heterogeneous nucleation during rapid cooling on the substrate [104].

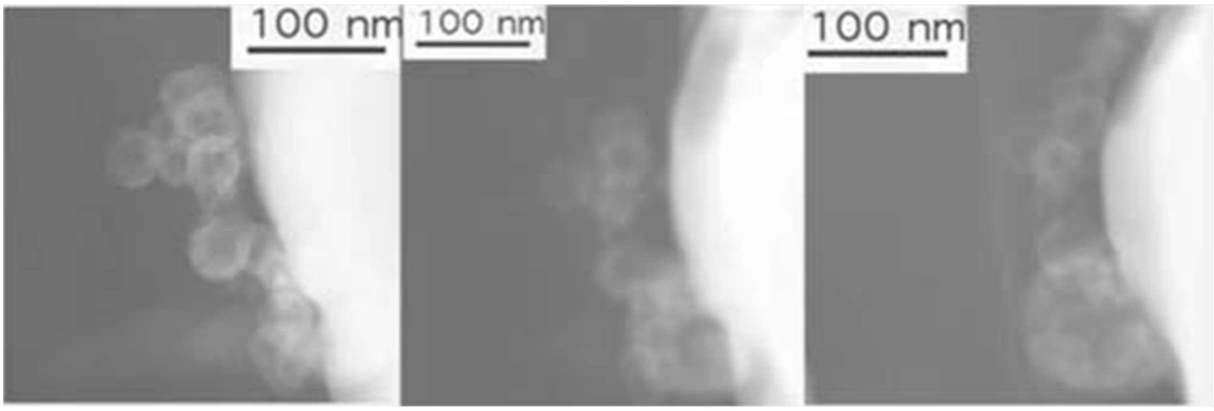

Figure 50: TEM image of clusters of nanodroplets attached to the substrate at different contact angles [94].

Kobe et al. [83] showed that there no significant amount of oxygen is present in the layer consisting of nanodroplets. By experimentally verifying the surface morphology using EDXS, it was observed that the denser the distribution of nanodroplets, the lower the degree of oxidization (Figure 51). This is important because the presence of oxygen has a negative effect on the magnetic properties of the deposited material. Surface oxidation results from the reaction with oxygen during exposure to atmospheric conditions as soon as the sample is taken out of the deposition chamber. Furthermore, the concentration of Ta also varied across the film area. The surface roughness in the Z-direction and surface density of the nanodroplets (Figure 47) were measured at 4.5 nm and 10^{10} droplets cm^{-2}, respectively [94]. EDXS analysis showed that the composition of the nanodroplets deposited on the Si/Ta substrate was very close to the composition of the target, i.e. Fe = 84 ± 10 at. %; Sm = 16 ± 10 at. %.

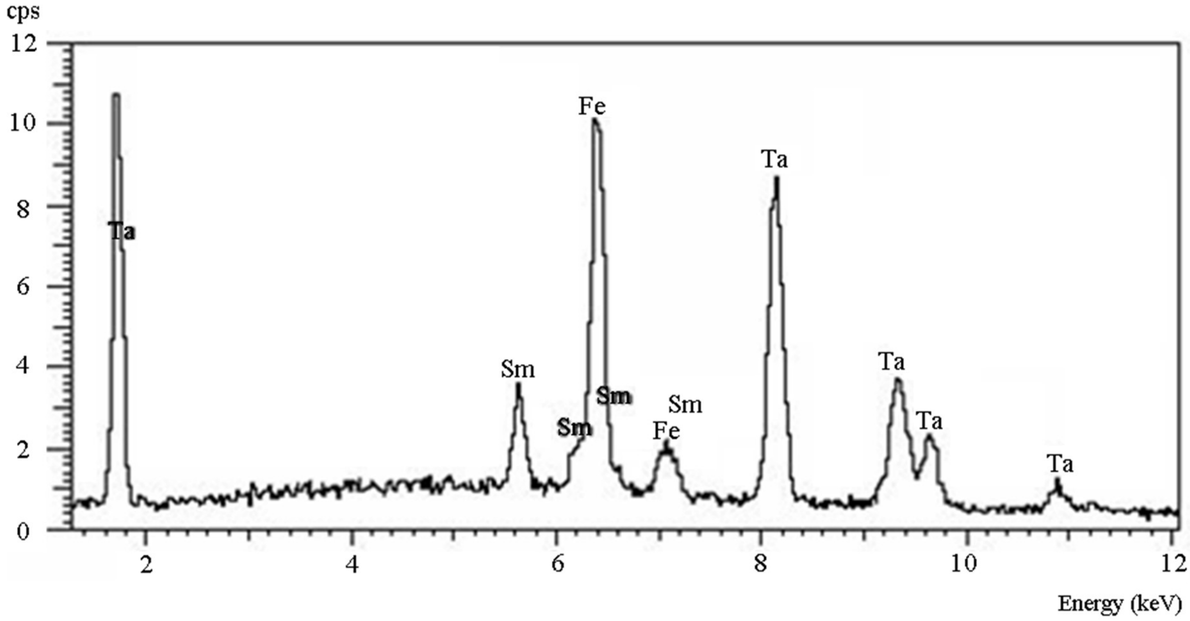

Figure 51: EDXS spectrum of the deposited material of Figure 47, which reveals no oxidation and a high concentration of Ta.

These results constitute a major contribution toward magnetic nanodroplets deposition by PLD at 157 nm. It was shown that the core-shell nanodroplets had a ferromagnetic response at room temperature (Kobe et al., 2007), which can be attributed to the non-oxidized crystalline cores embedded in the amorphous shell, which are needed for ferromagnetism.

4 Conclusion

Laser ablation has, until now, been one of the most versatile techniques for deposition of materials in thin films and layers of droplets (on selected substrates) with properties representing that of the original target material. The research in this thesis focused on two areas, namely on the study of the laser ablation process itself and that of the deposited material properties. We correlated these two areas and provided an integrated picture of the best possible laser ablation parameters (laser energy, gas-flow rate and target-substrate distance) for deposition of $Sm_{13.8}Fe_{82.2}Ta_{4.0}$ material on a Si/Ta substrate, transferring the target properties as flawlessly as possible to the deposited material.

The potential of an analytical LA-ICPMS system (213 nm Nd:YAG laser) for PLD purposes was investigated, i.e. using a target-substrate contraption to ablate and deposit particles in the ablation chamber (in He or N_2, under 1 bar pressure). It was found that the ablated particles were partially deposited onto the substrate whereas the majority (> 99 %) of particles was swept out of the chamber. These particles were transported to the ICPMS for in situ monitoring of the ablation plume and optimization of the critical PLD parameters (fluence, pulse rate, rastering speed, type of gas and gas flow rate). Additionally, the density, homogeneity and stoichiometry were investigated and the PLD parameters optimized using the LA-ICPMS instrument as an elemental mapping tool in combination with image analysis. In this way, information was gathered on the density and spatial stoichiometry of the deposit fabricated. Simultaneously, SEM-EDXS measurements revealed that the composition of the smaller particles (nm range) reflect that of the target while the Fe/Sm ratio in larger particles (> 1μm) is higher than in the target. The vaporization enthalpy of Fe is much higher than that of Sm causing Sm to vaporize readily upon laser heating and the particles ejected from the melt are expected to have a higher Fe/Sm ratio than the target. These results were in accordance with cascade impactor findings for fractions between 0.41 and 2.8 μm. However, the mass-weighted composition of the various particle sizes never differed more than ca. 10 %, which means that the composition of the particles reflects that of the target with little mass-weighted inter-particle heterogeneity.

Comparison with a real 157 nm PLD instrument taught us that the basic properties of the SmFeTa deposits fabricated were similar with both having a ferromagnetic response. For the real PLD instrument it was shown that the magnetic deposit consisted of biphase spherical nanodroplets (50–100 nm) with a 5–10 nm internal portion surrounded by an external amorphous phase. The surrounding amorphous layer prevents post-ablation oxidation of the crystalline magnetic nucleus of the nanodroplet, enhancing its magnetic properties in comparison to crystalline shapes of the larger surface area. Nanodroplets usually deteriorate the film's magnetic properties, but in certain cases, the formation of nanodroplets has a positive contribution on the product's quality, preserving the target's stoichiometry and uniformity in the crystal core as well as preventing oxidization which is essential for good magnetic properties. PLD by the 157 nm F_2 laser showed less and smaller particles deposited than the 213 nm Nd:YAG laser, better preserving the target stoichiometry and crystallinity resulting in excellent magnetic properties. In contrast, at 213 nm more and larger particles were deposited on the substrate due to laser-induced melting and splashing, resulting in poorer magnetic properties.

For the first time, an analytical LA-ICPMS intended for analytical microanalysis has been successfully used for PLD under atmospheric conditions, with the added advantage of in situ ICPMS monitoring of the ablation plume and ex situ LA-ICPMS of the deposited particles on the substrate. The dual purpose use may be seen as a new and exciting, generic approach to be applied to a myriad of target-substrate combinations for optimizing deposit fabrication (under atmospheric conditions) for all kinds of novel materials. Simultaneously, for the first time a 157 nm PLD indicated the magnetic properties of core-shell Sm-Fe-Ta-N nanodomains. By using nitrogen as a background gas, nitriding was already performed in the plume, thus enabling the production of magnetic particles without further treatment.

Nitrogenation induces interstitial modification of 3d metals and 3d-4f intermetallic compounds, which dilates the crystal lattice and changes the electronic structure, and leads to a significant changes of the magnetic properties. The nitrogen induces anisotropy in both the iron and rare-earth sublattices and makes the $Sm_2Fe_{17}N_3$ strong ferromagnets, with increased magnetisation and Curie temperature.

It was proven that the distance between the target and substrate, in addition to the laser energy and ambient pressure, determines the growth rate, composition and size of the biphase nanodroplets. These nanodroplets fabricated by 157 nm PLD at low laser energy (20 mJ) in a nitrogen atmosphere had a ferromagnetic response at room temperature. The thermodynamics of the nucleation and growth process of nanodroplets could explain the experimental results. Nevertheless, the theoretical values of alloy density and volume free energy were somewhat different from the experimental values, indicating that the target is inhomogeneous and has a higher concentration of the heavy element (Ta).

5 Acknowledgements

This work was carried out with the support and help of a great number of people during the course of my study. I would like to thank all the people who in different ways, supported me either directly in the completion of this work or indirectly with their friendship.

Special thanks go to my supervisor **Prof. Dr. Spomenka Kobe** for her untiring instruction and supervision throughout my research work. Her insight into the problems encountered has given me guidance on how to direct my work.

I would also like to thank the one-time head of the Analytical Chemistry Laboratory, **Dr. Božidar Ogorevc**, for giving me the opportunity to work in his group at the National Institute of Chemistry and to realize my PhD research work and this dissertation.

I would also like to especially thank my co-supervisor **Prof. Dr. Alkiviadis Constantinos Cefalas** for giving me the opportunity to perform my first experiments in PLD at the Short Light Wavelengths and Nano-applications Laboratory at the National Hellenic Research Foundation and for his assistance with regard paper work. He has also been extremely patient in explaining and discussing many physics-related problems with me.

I am very grateful to **Dr. Johannes Teun van Elteren** who, as my working mentor, did an excellent job in showing me what is really important and encouraging me when things did not go as expected and for his assistance with paper work.

I would also like to thank the **National Institute of Chemistry** and the **Slovenian Ministry of Science and Higher Education** for financially supporting my research.

My laboratory work was enjoyable and challenging and I would like to thank the many people for their assistance in facilitating my work. **Dr. Evangelia Sarantopoulou and Dr. Zoe Kollia** from the National Hellenic Research Foundation in Athens, Greece taught me the thin film PLD process in the early stages of my work and have been extremely helpful with regard to a number of general issues. **Dr. Kristina Žužek Rožman** from the Jožef Stefan Institute contributed numerous ideas on magnetic measurements and has proven a great inspiration in the fabrication of magnetic thin films and the research work.

Furthermore, I express my gratitude to: **Dr. Radojko Jaćimović** for the INAA measurements, **Dr. Goran Dražič** for my TEM data, **Mr. Gregor Kapun** and **Dr. Zoran Samardžija** for the SEM results and **Dr. Benjamin Podmiljšak** and **Dr. Andraž Kocjan** for the target preparation. Thank you all for all your help.

I would also like to express my appreciation for many of my colleagues and their kind assistance with the measurements and constructive discussions: **Dr. Irena Grgić**, **Dr. Vid Simon Šelih** and **Dr. Michael Beeston**.

Life in Slovenia would have been much more difficult for me without the help and support of **my husband Milan** and without the angelic smile of **my son Aleksandar**. Their encouragement has steered me through many difficult periods.

There are two people in particular to whom I would like to express my deepest gratitude and love for their endless support. **My parents** have been extremely understanding and constantly supportive towards my study.

At the end, I would like to thank all the other people at the Analytical Chemistry Laboratory at the National Institute of Chemistry who helped me in one way or another.

The work was done at the National Institute of Chemistry, Ljubljana, Slovenia and National Hellenic Research Foundation in Athens, Greece. It was financially supported by the Slovenian Ministry of Science and Higher Education.

6 References

[1] Howard, M. S.; Turner, A. F. Vacuum Deposited Thin Films Using a Ruby Laser. *Applied Optics* **4**, 147 (1965).

[2] Strickland, D.; Mourou, G. Compression of amplified chirped optical pulses. *Optical Communications* **56**, 219 (1985).

[3] Russo, R. E.; Mao, X. L.; Mao, S. S. The physics of Laser ablation in Microchemical. *Analytical Chemistry* **74**, 70A (2002).

[4] Gonzalez, J.; Mao, X. L.; Roy, J.; Mao, S. S.; Russo, R. E. Comparison of 193, 213 and 266 nm laser ablation ICP-MS. *Journal of Analytical Atomic Spectrometry* **17**, 1108 (2002).

[5] Hattendorf, B.; Latkoczy, C.; Günther, D. Laser ablation ICP-MS. *Analytical Chemistry* **August 1**, 341A (2003).

[6] Wolf, R.; Thomas, C.; Bohlke, A. Analytical determination of metals in industrial polymers by laser ablation ICP-MS *Applied Surface Science* **127–129**, 299 (1998).

[7] Lenzner, M.; Krausz, F.; Kruger, J.; Kautek, W. Photoablation with sub-10 fs laser pulses. *Applied Surface Science* **154–155**, 11 (2000).

[8] Rudolph, P.; Bonse, J., Kruger, J.; Kautek, W. Femtosecond- and nanosecond pulse laser ablation of bariumalumoborosilicate glass. *Applied Physics A: Materials Science and Processing* **69**, S763 (1999).

[9] Le Drogoff, B.; Margot, J.; Chaker, M.; Sabsabi, M.; Barthelemy, O.; Johnston, T. W.; Laville, S.; Vidal, F.; Von Kaenel, Y. Temporal characterization of femtosecond laser pulses induced plasma for spectrochemical analysis of aluminum alloys. *Spectrochimica Acta Part B: Atomic Spectroscopy* **56**, 987 (2001).

[10] Shi, W. S.; Zheng, Y. F.; Peng, H. Y.; Wang, N.; Lee, C. S.; Lee, S. T. Laser ablation synthesis and optical characterization of silicon carbide nanowires. *Journal of the American Ceramic Society*, **83**, 3228 (2000).

[11] Wu, M. K.; Ashbum, J. R.; Tomg, C. J.; Hor, P. H.; Meng, R. L.; Gao, L.; Huang, Z. J.; Wang, Y. Q.; Chu, C. W. Superconductivity at 93 K in a New Mixed-Phase Y-Ba-Cu-O Compound System at Ambient Pressure. *Physical Review Letters* **58**, 908 (1987).

[12] Dijkkamp, D.; Venkatesan, T.; Wu, X. D.; Shaheen, S. A.; Jisrawi, N.; Min-Lee, Y. H.; Mclean, W. L.; Croft, M. Preparation of Y-Ba-Cu oxide superconductor thin films using pulsed laser evaporation from high Tc bulk material. *Applied Physics Letters* **51**, 619 (1987).

[13] Fang, R.; Zhang, D.; Li, Z.; Li, L.; Tan, X.; Yang, F. Laser-target interaction during high-power pulsed laser deposition of superconducting thin films. *Physics status solid (a): Applications and Materials Science* **204**, 4241 (2007).

[14] Chichkov, B. N.; Momma, C.; Nolte, S.; Von Alvensleben, F.; Tünnermann, A. Femtosecond, picosecond and nanosecond laser ablation of solids. *Applied Physics A: Materials Science and Processing* **63**, 109 (1996).

[15] Leboeuf, J. N.; Chen, K. R.; Donato, J. M.; Geohegan, D. B.; Liu, C. L.; Puretzky, A. A.; Wood, R. F. Modeling of dynamical processes in laser ablation. *Applied Surface Science* **96–98**, 14 (1996).

[16] Lunney, J. G.; Jordan, R. Pulsed laser ablation of metals. *Applied Surface Science* **127–129**, 941(1998).

[17] Haglund Jr, R. F. Microscopic and mesoscopic aspects of laser-induced desorption and ablation. *Applied Surface Science* **96–98**, 1 (1996).

[18] Singh, R. K.; Narayan, J. Pulsed-laser evaporation technique for deposition of thin films: Physics and theoretical model. *Physical Review B: Condensed matter and material physics* **41**, 8843 (1990).

[19] Willmott, P. R.; Huber, J. R. Pulsed laser vaporization and deposition. *Review Modern Physics* **72**, 315 (2000).

[20] Ashfold, M. N. R.; Claeyssens, F.; Fuge, G. M.; Henley, S. J. Pulsed laser ablation and deposition of thin films. *Chemical Society Review* **33**, 23 (2004).

[21] Shen, J.; Gaj, Z.; Kirschner, J. Growth and magnetism of metallic thin films and multilayers by pulsed-

laser deposition. *Surface Science Report* **52**, 163 (2004).

[22] Hergenröder, R. A model of non-congruent laser ablation as a source of fractionation effects in LA-ICP-MS. *Journal of Analytical Atomic Spectrometry* **21**, 505 (2006).

[23] Hergenröder, R. Laser generated aerosols in laser ablation for inductively coupled plasma spectrometry. *Spectrochimica Acta Part B: Atomic Spectroscopy* **61**, 284 (2006).

[24] Hergenröder, R. A model for the generation of small particles in laser ablation ICP-MS. *Journal of analytical Atomic Spectrometry* **21**, 1016 (2006).

[25] Hergenröder, R. Hydrodynamic sputtering as a possible source for fractionation in LA-ICP-MS. *Journal of analytical Atomic Spectrometry* **21**, 517 (2006).

[26] Anisimov, S. I.; Luk'yanchukand, B. S.; Luches, A. An analytical model for three-dimensional laser plume expansion into vacuum in hydrodynamic regime. *Applied Surface Science* **96–98**, 24 (1996).

[27] Kools, J. C. S.; Baller, T. C.; Dezwart, S. T.; Dieleman, J. Gas-flow dynamics in laser ablation deposition. *Journal of Applied Physics* **71**, 4547 (1992).

[28] Sambri A. *Pulsed laser deposition of complex transition metal oxides: plume expansion and film growth*. *PhD Thesis* (University of Geneva, Department of Condensed Matter Physics, 2007).

[29] Murakami, K.; Makimura, T.; Ono, N.; Sakuramoto, T.; Miyashita, A.; Yoda, O. Dynamics of Si plume produced by laser ablation in ambient inert gas and formation of Si nanoclusters. *Applied Surface Science* **127–129**, 368 (1998).

[30] Venables, J. A.; Spiller, G. D. T.; Hanbucken, M. Nucleation and growth of thin films. *Reports on progress in physics* **47**, 399 (1984).

[31] Horwitz, J. S.; Sprague, J. A. Film Nucleation and Film Growth in PLD of Ceramics. In: Chrisey, D. B; Hubler, G. K. (ed.) *Pulsed Laser Deposition of Thin Films*. 229–254 (Wiley and Sons Incorporation, New York, 1994).

[32] Hubler, G. K. In: Chrisey, D. B; Hubler, G. K. (ed.) *Pulsed Laser Deposition of Thin Films*. 327–355 (Wiley and Sons Incorporation, New York, 1994).

[33] Claeyssens, F. *Fundamental Studies of Pulsed Laser Ablation*. *PhD Thesis* (University of Bristol, Department of Chemistry, December, 2001).

[34] Chen, L. C. Particulates Generated by Pulsed Laser Ablation. In: Chrisey, D. B; Hubler, G. K. (ed.) *Pulsed Laser Deposition of Thin Films*. 167–198 (Wiley and Sons Incorporation, New York, 1994).

[35] Gamaly, E. G.; Rode, A. V.; Luther-Davies, B.; Tikhonchuk, V. T. Ablation of solids by femtosecond lasers: ablation mechanism and ablation thresholds for metals and dielectrics *Physics of Plasmas* **9**, 949 (2002).

[36] Martin, S.; Hertwig, A.; Lenzner, M.; Krüger, J.; Kautek, W. Spot-size dependence of the ablation threshold in dielectrics for femtosecond laser pulses. *Applied Physics A: Materials Science and Processing* **77**, 883 (2003).

[37] Doeswijk, L. M.; Rijnders, G.; Blank, D. H. A. Pulsed laser deposition: metal versus oxide ablation. *Applied Physics A*: *Materials Science and Processing* **78**, 263 (2004).

[38] Kautek, W.; Roas, B.; Schultz, L. Formation of Y-Ba-Cu-oxide thin films by pulsed laser deposition: A comparative study in the UV, visible and IR range. *Thin Solid Films* **191**, 317 (1990).

[39] Matsunawa, A.; Katayamy, S.; Susuki, A.; Ariyasu, T. Laser production of metallic ultra-fine particles. *Transactions of JWRI* **15**, 233 (1986).

[40] Tuohiniemi, M. Laser-Ablation System for Depositing High-Temperature Superconducting $YBa_2Cu_3O_{7-\delta}$ Thin Films. *Master's Thesis* (Helsinki University of Technology, Espoo, 1999).

[41] Dyer, P. E.; Issa, A.; Key, P. H. Dynamics of excimer laser ablation of superconductors in an oxygen environment *Applied Physics Letters* **57**, 186 (1990).

[42] Saenger, K. L. Angular distribution of the ablated material In: Chrisey, D. B; Hubler, G. K. (ed.) *Pulsed Laser Deposition of Thin Films*. 199–227 (Wiley and Sons Incorporation, New York, 1994).

[43] Davanloo, F.; Juengerman, E. M.; Jander, D. R.; Lee, T. J.; Collins, C. B.; Matthias, E. Mass flow in laser-plasma deposition of carbon under oblique angles of incidence. *Applied Physics A: Materials Science and Processing* **A54**, 369 (1992).

[44] Perrone, A.; Zocco, A.; Cultrera, L.; Guido, D. Detailed studies of the plume deflection effect during long laser irradiation of solid targets. *Applied Surface Science* **197–198**, 251 (2002).

[45] Cultrera, L.; Guido, D.; Perrone, A.; Zeifman, M. I. Plume separation effect in pulsed laser ablation deposition. *Applied Physics A: Materials Science and Processing* **79**, 1181 (2004).

[46] Cadieu, F. J. Permanent magnetic films for application. In: Adam, J. D.; Francombe, M. H. (ed.) *Handbook of Thin Film Devices Technology and Applications*. Volume 4: Magnetic Thin Film Devices

(Academic Press Incorporation, 2000).

[47] Krieger, M.; Plettl, A.; Steiner, R.; Boyen, H. G.; Ziemann, P. Properties of a Co/Cu/Co spin valve system prepared by an optimized 193 nm pulsed laser deposition process. *Applied Physics A: Materials Science and Processing* **78**, 327 (2004).

[48] Caricato, A. P.; Fernandez, M.; Luches, A.; Luby, S.; Majkova, E.; Chitu, L.; Svec, P.; Frait, Z.; Fraitova, D.; Malych, R.; Mengucci, P. Magnetic damping in Fe-based films deposited by laser ablation in magnetic field. *Applied Surface Science* **252**, 4907 (2006).

[49] Cadieu, F. J.; Cheung, T. D.; Wickramasekara, L.; Kamprath, N. High perpendicular anisotropy Nd-Fe-B sputtered films. *IEEE transitions on magnetic* **22**, 752 (1986).

[50] Cadieu, F. J.; Rani, R.; Qian, X. R.; Chen, L. High coercivity SmCo based films made by pulsed laser deposition. *Journal of Applied Physics* **83**, 6247 (1998).

[51] Cadieu, F. J.; Rani, R.; Theodoropoulos, T.; Chen, L. Fully in plane aligned SmCo based films prepared by pulsed laser deposition. *Journal of Applied Physics* **85**, 5895 (1999).

[52] Neu, V.; Thomas, J.; Fähler, S.; Holzapfel, B.; Schultz, L. Hard magnetic SmCo thin films prepared by pulsed laser deposition. *Journal of Magnetism and Magnetic Materials* **242**, 1290 (2002).

[53] Liu, Y.; Thomas, R. A.; Malhotra, S. S.; Shan, Z. S.; Liou, S. H.; Sellmyer, D. J. Phase formation and magnetic properties of Co-rare earth magnetic films. *Journal of Applied Physics* **83**, 6244 (1998).

[54] Yang, C.; Kim, S. W; Kang, J. S. Magnetic properties of NdFeB thin films synthesized via laser ablation processing. *Journal of Applied Physics* **83**, 6620 (1998).

[55] Kwon, A. R.; Fähler, S.; Neu, V.; Schultz, L. Effect of composition on phase formation, microstructure and magnetic properties of Nd-Fe-B thin films. *Journal of Magnetism and Magnetic Materials* **302**, 252 (2006).

[56] Song, J. M.; Sadakata, H.; Nakano, M.; Kanai, Y.; Fukunaga, H.; Koh, J. G. Effects of film thickness and droplets on magnetic properties of SmFeN films prepared by laser ablation technique. *IEEE transitions on magnetic* **35**, 3052 (1999).

[57] Jang, P. W.; Wang, D.; Doyle, W. D. Structural and magnetic properties of epitaxially grown Fe-Sm and Fe-Sm-N films. *Journal of Applied Physics* **81**, 4664 (1997).

[58] Kobe, S.; Žužek, K.; Sarantopoulou, E.; Samardzija, Z.; Kollia, Z.; Cefalas, A. C. Nanocrystalline Sm-Fe composites fabricated by pulsed laser deposition at 157 nm. *Applied Surface Science* **248**, 349 (2005).

[59] Coey, J. M. D; Sun, H. Improved magnetic properties by treatment of iron-based rare earth intermetallic compounds in ammonia. *Journal of Magnetism and Magnetic Materials* **87**, L251 (1990).

[60] Jang, P. W.; Wang, D.; Doyle, W. D. Structural and magnetic properties of epitaxially grown Fe-Sm and Fe-Sm-N films. *Journal of Applied Physics* **81**, (Part 2) (1999).

[61] Žužek, K.; McGuiness, P. J.; and Kobe, S. Magnetic monitoring of the nitriding process in Sm-Fe-Ta based alloys *IEEE transitions on magnetic* **39**, 2983 (2003).

[62] Saje, B.; Platts, E. A.; Besenicar, K. S.; Harris, R. I. Kolar, D. Microstructure and magnetic properties of Sm-Fe-Ta based alloys. *IEEE transitions on magnetic* **30**, 690 (1994).

[63] Sarantopoulou, E.; Kobe, S.; Rožman, Ž. K.; Kollia, Z.; Dražić, G.; Cefalas, A. C. Fabrication of magnetic SmFe films by pulsed laser deposition at 157 nm *IEEE transitions on magnetic* **40**, 2943 (2004).

[64] O'Handlay, R. C. *Modern Magnetic Materials: Principles and Applications* (John Wiley & Sons Incorporation, New York, 2000).

[65] Zheng, P. Magnetic MEMS and its applications. *Doctoral Dissertation* (Florida State University, Department of Mechanical Engineering, 2004).

[66] Rao, K. S. Microstructure and Texture of Yttrium-Nickel-Borocarbide and Samarium-Cobalt Thin Films. *Doctoral Dissertation,* (Dresden University of Technology, Faculty of Mathematics and Natural Sciences, 2006).

[67] Coey, J. M. D. Interstitial intermetallics. *Journal of Magnetism and Magnetic Materials* **159**, 80 (1996).

[68] Wang, X. Z.; Etourneau, K.; Berlureau, T. Hydrogen absorption and desorption in Nd_2Fe_{17} and Sm_2Fe_{17}. *Journal of Materials Science* **23**, 329 (1988).

[69] Wang, Y. Z.; Hadjipanayis, G. C. Magnetic properties of $Sm_2Fe_{17}C_x$ compounds. *Journal of Applied Physics* **69**, 5565 (1991).

[70] Yao, Y. D.; Kuo, P. C.; Chang, W. C.; Liu, C. J. Electrical and magnetic studies of (Cu/Zn)-bonded $Sm_2Fe_{17}M_xN_y$ magnets (M = B or C). *Journal of Applied Physics* **75**, 6244 (1994).

[71] Chen, X.; Altounian, Z. Hydrogenation decomposition desorption recombination magnets based on Sm_2+delta-$Fe_{17}M_{0.4}$ carbonitrides (M= IVB/VB/VIB group elements). *Journal of Applied Physics* **75**, 6012 (1994).

[72] Žužek, K.; McGuiness, P. J.; and Kobe, S. Gaseous interactions with Sm-Fe and Sm-Fe-Ta intermetallic alloys. *Journal of Alloys and Compounds* **289**, 213 (1999a).

[73] Žužek, K.; McGuiness, P. J.; and Kobe, S. Bonded Sm-Fe-(Ta)-N materials produced via attritor milling and HDDR. *Journal of Alloys and Compounds* **289**, 265 (1999b).

[74] Rao, X. L.; Skomski, R.; Qi, Q. N.; Coey, J. M. D. Paramagnetic densities of states of iron-rich permanent magnets. *Physica Status Solid (b): Basic solid state physics* **186**, K23 (1994).

[75] Chen, X. X.; Liu, G. C.; Niu, M. L.; Meng, Q. H.; Xing, J. P.; Xu, Z. J.; Zu, K. L.; Hu, B. P. ^{57}Fe Moössbauer effect studies of Sm_2Fe_{17} under different heat treatment conditions. *Journal of materials science*. **32**, 5955 (1997).

[76] Coey, J. M. D.; Smith, P. A. I. Magnetic nitrides. *Journal of Magnetism and Magnetic Materials* **200**, 405 (1999).

[77] Skomski, R.; Coey, J. M. D. Nitrogen diffusion in Sm_2Fe_{17} and local elastic and magnetic properties. *Journal of Applied Physics* **73**, 7602 (1993).

[78] Müller, K. H.; Cao, L.; Dempsey, N. M.; Wendhausen, P. A. P. Sm_2Fe_{17} interstitial magnets. *Journal of Applied Physics* **79**, 5045 (1996).

[79] Cefalas, A. C.; Skordoulis, C.; Kompitsas, M.; Nikolaides, C. A. Gian measurements at 157 nm in a molecular fluorine pulsed discharge molecular laser. *Optics Communications* **55**, 423 (1985).

[80] Gray, A. L. Solid sample introduction by laser ablation for inductively coupled plasma source-mass spectrometry. *Analyst* **110**, 551 (1985).

[81] Jaćimović, R.; Smodiš, B.; Bučar, T.; Stegnar, P. k_0–NAA Quality Assessment by Analysis of Different Certified Reference Materials Using the KAYZERO/SOLCOI Software. *Journal of Radioanalytical and Nuclear Chemistry* **257**, 659 (2003).

[82] Cultrera, L.; Zeifman, M. I.; Perrone, A. Investigation of liquid droplets, plume deflection and, a columnar structure in laser ablation of silicon. *Physical Review B* **73**, 075304–1 (2006).

[83] Kobe, S.; Sarantopoulou, E.; Dražić, G.; Kovač, J.; Janeva, M.; Kollia, Z.; Cefalas, A. C. Growth of crystalline/amorphous biphase Sm-Fe-Ta-N magnetic nanodroplets. *Applied Surface Science* **254**, 1027 (2007).

[84] Guillong, M.; Günther, D. Effect of particle size distribution on ICP-induced elemental fractionation in laser ablation-inductively coupled plasma-mass spectrometry. *Journal of Analytical Atomic Spectrometry* **17**, 831 (2002).

[85] Horn, I.; Guillong, M.; Günther, D. Wavelength dependant ablation rates for metals and silicate glasses using homogenized lase beam profiles-implications for LA-ICP-MS. *Applied Surface Science* **182**, 91 (2001).

[86] Koch, J.; Von Bohlen, A.; Hergenröder, R.; Niemax, K. Particle size distributions and compositions of aerosols produced by near-IR femto- and nanosecond laser ablation of brass. *Journal of Analytical Atomic Spectrometry*, **19**, 267 (2004).

[87] Liu, C. Y.; Mao, X. L.; Mao, S. S.; Greif, R.; Russo, R. E. Particle size dependent chemistry from laser ablation of brass. *Analytical Chemistry* **77**, 6687 (2005).

[88] Stokes, R. J.; Fennell, E. D. *Fundamentals of Interfacial Engineering* (Wiley and Sons Incorporation, New York, 1997).

[89] Horn, I.; Günther, D. The influence of ablation carrier gasses Ar, He and Ne on the particle size distribution and transport efficiencies of laser ablation-induced aerosols: implications for LA-ICP-MS. *Applied Surface Science* **207**, 144 (2003).

[90] Cefalas, A. C.; Kovač, J.; Sarantopoulou, E.; Dražić, G.; Kollia, Z.; Kobe, S. Growth and adhesion of biphasic crystalline-amorphous Sm/Fe-Ta-N magnetic nanospheroids on a Ta surface. *Surface and Interface Analysis* **40**, 364 (2008).

[91] Thestrup, B.; Toftmann, B.; Schou, J.; doggett, B.; Lunney, J. G. Acomparison of the laser plume from Cu and YBCO studied with ion probes. *Applied Surface Science* **208–209**, 33 (2003)

[92] Liáng, L. C. (ed.) *YBCO Superconductor Research Progress* (Nova Science Publishers, New York, 2008).

[93] Huafu, Z.; Hanfa, L.; Aiping, Z.; Changkun, Y. Influence of the distance between target and substrate on the properties of transparent conducting Al-Zr co-doped zinc oxide thin films. *Journal of Semiconductors* **30**, 113002–1 (2009).

[94] Buschow, K. H. J.; Goot, A. S. Composition and crystal structure of hexagonal Cu-rich rare earth-copper compounds. *Acta Crystallographica–Section B: Structural Crystallography and Crystal Chemistry* **27**, 1085 (1971).

[95] Khan, Y. On the crystal structures of the R_2Co_{17} intermetallic compounds. *Acta Crystallographica–Section B: Structural Crystallography and Crystal Chemistry* **29**, 2502 (1973).

[96] Meacham, B. E.; Shield, J. E.; Branagan,D. J. Order–disorder effects in nitrided Sm–Fe permanent magnets. *Journal of Applied Physics* **87**, 6707 (2000).

[97] Teresiak, A.; Gebel, B.; Handstein, A.; Mattern, N.; Klose, H.; Muller, K. H. In-situ observation of the nitrogenation of Sm_2Fe_{17} by means of high-temperature x-ray diffraction. *Journal of Analitical Chemistry* **361**, 674 (1998).

[98] Yang, J. Y.; Yoon, K. S.; Do, Y. H.; Koo, J. H.; Kim, C. O; Hong, J. P. Magnetic properties of laser-induced ferromagnetic cobalt quantum dots passivated by ultrathin Ta films**.** *Journal of Applied Physics* **95**, 7548 (2004).

[99] Butler, R. F. PALEOMAGNETISM: Magnetic Domains to Geologic Terranes, Chapter 3 (University of Portland, Sptember 2004).

[100] Kodama, R. H.; Berkowitz, A. E.; McNiff Jr. E. J.; Foner, S. Surface Spin Disorder in $NiFe_2O_4$ Nanoparticles. *Physical Review Letters* **77**, 394 (1996).

[101] Martinez, B.; Obradors, X.; Balcells, L.; Rouanet, A.; Monty, C. Low Temperature Surface Spin-Glass Transition in γ- Fe_2O_3 Nanoparticles. *Physical Review Letters* **80**, 181 (1998).

[102] Kodama, R. H.; Berkowitz, A. E. Atomic-scale magnetic modeling of oxide nanoparticles. *Physical Review B* **59**, 6321 (1999).

[103] Aharoni, A. Introduction to the theory of ferrimagnetism. (Oxford Science Publications, Oxford, 1996).

[104] Cefalas, A. C.; Kobe, S.; Sarantopoulou, E.; Samardzija, Z.; Janeva, M.; Dražić, G.; Kollia, Z. Growth, clustering and morphology of intermetallic alloy core-shell nanodroplets. *Physica Status Solidi (a): Applications and Materials Science* **205**, 1465 (2008).

[105] Kathmann, S. M.; Schenter, G. K.; Garrett, B. C.; Chen, B.; Siepmann, J. I. Thermodynamics and Kinetics of Nanoclusters Controlling Gas-to-Particle Nucleation. *Journal of Physical Chemistry C* **113**, 10354 (2009).

[106] Santra, M.; Chakrabarty, S.; Bagchi, B. Gas-Liquid Nucleation in Two Dimensional System. *Journal of Chemical Physics* **129**, 234704 (2008).

Index of Figures

Index of Tables

Appendix 1

A.1. Characterization methods for ablation products

A.1.1. In-line methods

Inductively Coupled Plasma Mass Spectrometry (ICP-MS): The main components of the ICPMS instrument used (Agilent 7500ce) for monitoring the PLD plume are shown in Figure 52. The inductively coupled plasma (ICP) is generated in a stream of argon (Ar) in a quartz tube (torch), which is placed in a cooled copper coil. A high power, high frequency electric current, produced by a radio frequency (RF) generator, is applied to the coil to create a magnetic field, which causes collisions between free electrons and Ar atoms. These collisions produce more free electrons and ions, until a plasma is formed. Because of the very high plasma temperature, the particles in the PLD plume are rapidly vaporized, atomized, ionized and the positively charged ions are then extracted from the atmospheric pressure of the plasma into the vacuum system of the mass spectrometer (MS) via a pair of interface (sample and skimmer) cones.

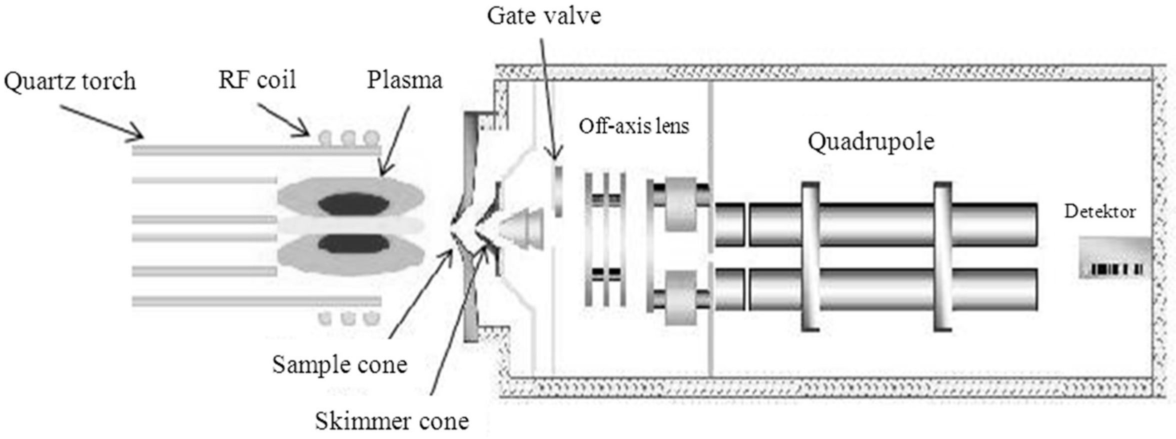

Figure 52: Schematic diagram of the Agilent 7500 series ICP-MS instrument.

A vacuum better than 0.1 Pa is created behind the cones by a turbomolecular pump to reduce the background and scattering effects caused by the residual gas molecules. The ions pass to the mass spectrometer (MS) and then to the detector through the electrostatic off-axis lenses, which focus the ions in a compact “ion beam” and separate them from the photons and neutral particles, which will increase random background noise if they reach the detector. The quadrupole mass analyzer comprises four cylindrical rods, arranged in a square on the axis of the ion beam and separates ions based on their mass (m) to charge (z) ratio, using a combination of DC (direct current) and AC (alternating current) electrical fields. Mass selection is achieved by varying the AC and DC fields, keeping the ratio between them constant. Depending on the voltage, only one mass per charge is stable and passes the length of the quadrupole. Since the voltage can be adjusted very rapidly, the whole mass spectrum, for all elements and their isotopes, can be scanned continuously. It is also possible to measure only masses of interest, jumping between each measured mass (peak jumping), saving a lot of acquisition time.

After the separation, the ions are counted in a so-called electron multiplier, yielding a signal (in cps) for each mass to charge ratio (m/z) and creating a mass spectrum. The spectrum provides accurate quantitative information about the sample; the magnitude of each peak is proportional to the elemental concentration in the sample. Calibration with dedicated (matrix-matched) standards is essential to convert cps into concentration units.

Cascade impactor: A cascade impactor is a multi-stage sampling device designed for determining the particle size distribution of ambient and industrial aerosols. Aerosol particles flow into the cascade impactor where they impinge upon a sequence of solids discs (or stages). The impactor contains flow chambers connected in a vertical arrangement, where the solids discs are placed. The velocity of the particles increases for each successive disc, implying that the largest particles will be captured on the first disc and successively smaller particles on the next discs. The principle of operation of an impactor is based on accelerating an aerosol particle through a nozzle with the output stream directed against a flat plate. The flat plate (impaction plate) deflects the flow to form a sudden 90° bend in the streamlines. Particles with sufficient inertia are unable to follow the streamlines and impact on the flat plate, while smaller particles are able to follow the streamlines and avoid hitting the impaction plate. Particles with the largest aerodynamic size are removed from the air stream during the first stage, while smaller particles travel through the impactor and deposit at a stage, which corresponds to their aerodynamic size. Often ten stages are used in a cascade impactor to divide the size distribution into an equivalent number of portions. Details of the impactor and its application for size-segregation of laser ablation-generated aerosol particles are given in Figure 53.

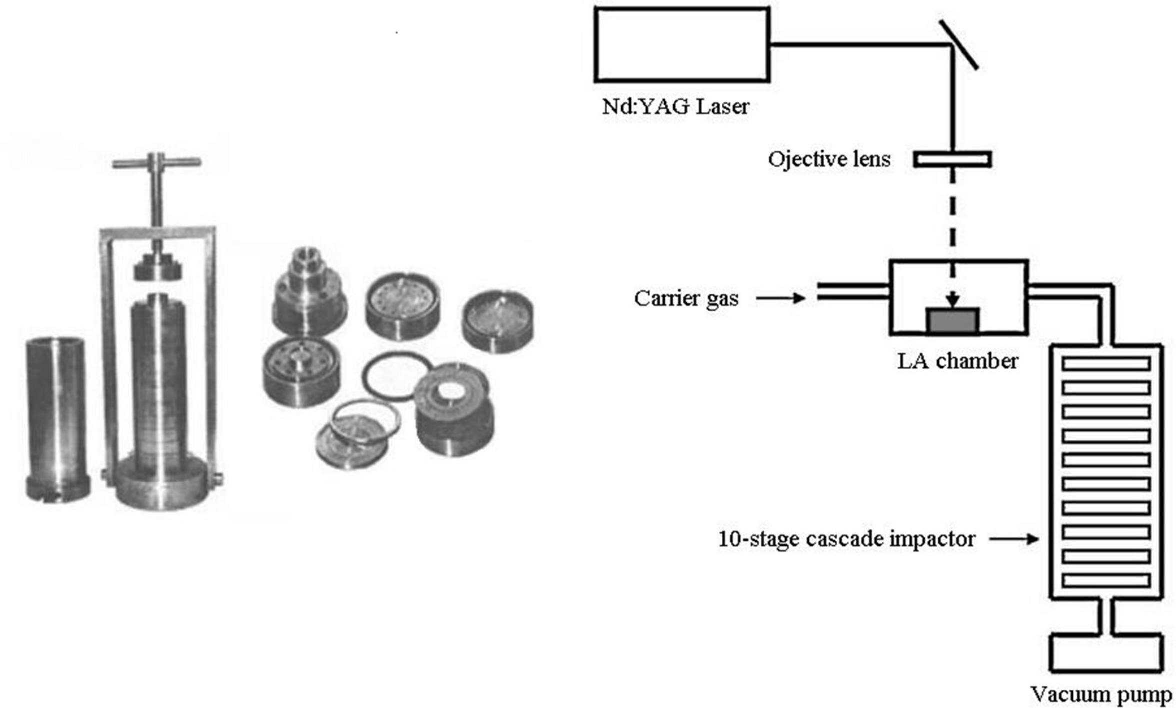

Figure 53: Berner ten-stage low-pressure cascade impactor (left) and a schematic diagram of the experimental setup (right).

A.1.2. Off-line methods

Scanning electron microscopy: A scanning electron microscope (SEM) is an instrument that uses a high-energy focused electron beam, which may be swept in a raster scan pattern across the surface of the sample to form an image. When the electrons strike the sample, electron and photon signals are emitted which contain compositional, topographical and electrical information about the sample. All signals that are produced by the SEM include secondary electrons, back-scattered electrons (BSE), characteristic X-rays, light (cathodoluminescence) and specimen current and transmitted electrons, but not all of them are detected and used for information. The signals most commonly used are the secondary electrons, back-scattered electrons and X-rays. The secondary and back-scattered electrons are imaging signals of the greatest interest, because they primarily vary due to differences in surface topography. The secondary electron emission for certain choices of beam and energy enable images to be obtained at a resolution approximating the size of the focused electron beam.

The SEM has a large depth of field, enabling a better understanding of the surface structure of the sample by yielding a characteristic three-dimensional appearance of the images. The three-dimensional appearance of the sample images is also due to the shadow relief effect of the secondary and back-scattered electron contrast. Back-scattered electrons (BSE) are reflected or back-scattered by elastic scattering interactions with sample atoms and BSE images can provide information about the distribution of different elements in the sample. Characteristic X-rays are emitted as a result of electron bombardment and yield information on the composition, measuring the abundance of elements in the sample. This elemental analysis is carried out using an on-line energy-dispersive X-ray spectrometer (EDXS). For conventional imaging using an SEM, samples must be electrically conductive. Metals require little preparation; cleaning and mounting on a specimen stub and nonconductive samples are usually coated with an ultra thin coating of electrically-conducting material, commonly gold or graphite. The coating prevents the accumulation of static electric charge on the sample during electron irradiation. An exploded view of a SEM is shown in Figure 54.

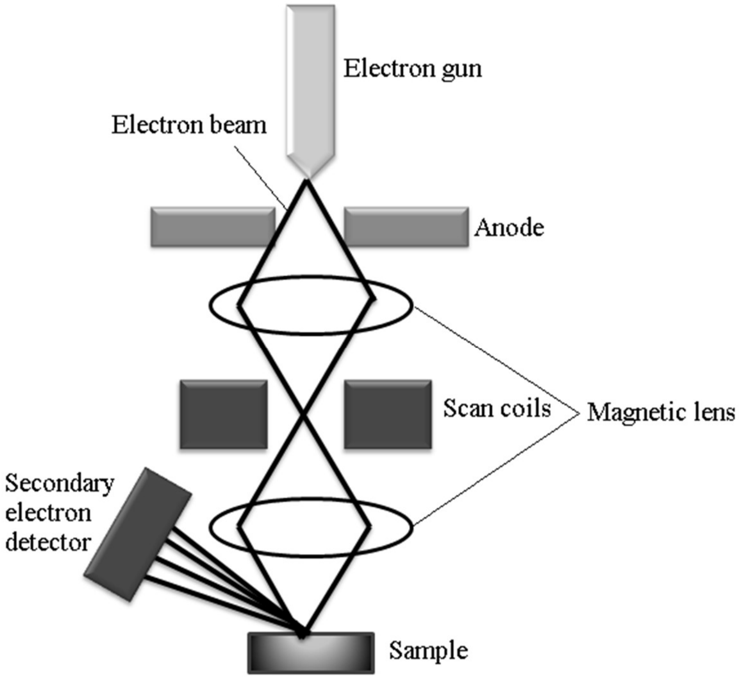

Figure 54: Diagram of a scanning electron microscope.

Transmission electron microscopy: A transmission electron microscope (TEM) is an instrument that uses a beam of electrons to scrutinize a specimen at very fine resolutions. The beam of electrons interacts with the sample as it passes through and a magnified image is formed using a set of lenses. This image is focused onto a fluorescent screen, a CCD camera or a photographic plate. The electron beam can be transmitted or scattered. If the transmitted and diffracted beam is focused onto an imaging device, the resultant image is called a bright-field and dark-field image, respectively. Because of the TEM capability of imaging at a significantly higher resolution, atomic arrangements in crystalline structures can be imaged and crystallographic information from thin films, bulk materials as well as nanometer sized particles can be obtained in detail. The components of TEM are schematically represented in Figure 55.

As a result of the interaction of the electron beam with the sample, some energy is transferred from the electrons to the sample. Excitation and de-excitation of atoms and molecules enable chemical analysis. The combination of scanning transmission electron microscopy (STEM), a mode in which a strongly focused beam scans a selected area of the sample, with chemical analysis techniques such as electron energy loss spectroscopy (EELS) and energy dispersive X-Ray spectroscopy analysis (EDXS) enables mapping of the lateral distribution of elements with high spatial resolution.

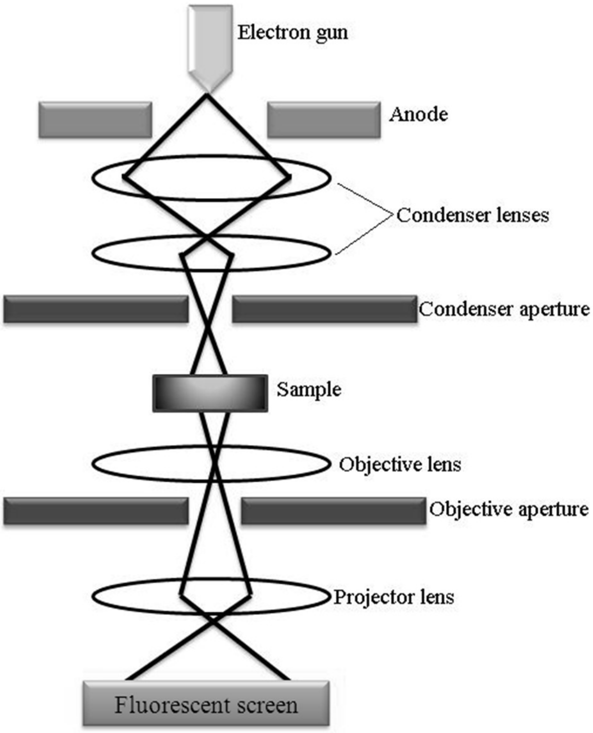

Figure 55: Diagram of a transmission electron microscope.

Atomic Force Microscopy (AFM): Atomic force microscopy (AFM) is a form of scanning probe microscopy (SPM) with a very high-resolution in the order of fractions of a nanometer. AFM is one of the most important instruments for imaging, measuring and manipulating matter at the nanoscale. The AFM instrument consists of a cantilever with a sharp tip (probe) at its end (Figure 56). Information is gathered from the mechanical probe's interaction with the surface. The probe scans the sample in a raster pattern across the surface to form a map of the measured property relative to the X-Y position and collects the physical, magnetic or chemical properties of the material.

The AFM probe has a very sharp tip, often less than 10 nm diameter. When the tip is brought into proximity of a sample surface, the forces between the tip and sample lead to a deflection of the cantilever according to Hooke's law, Equation 27.

$$F = -kx \tag{27}$$

where F is the force, k the stiffness of the lever and x the probe distance from the sample.

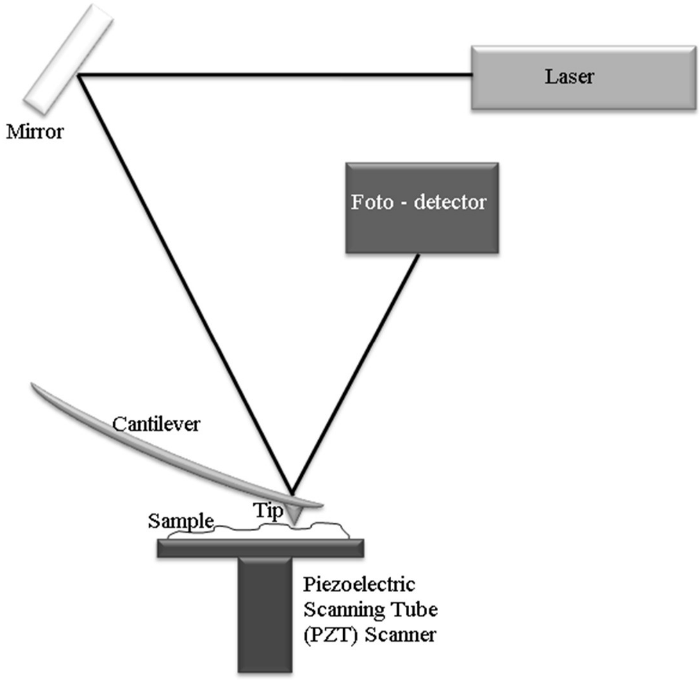

Figure 56: Diagram of atomic force microscope.

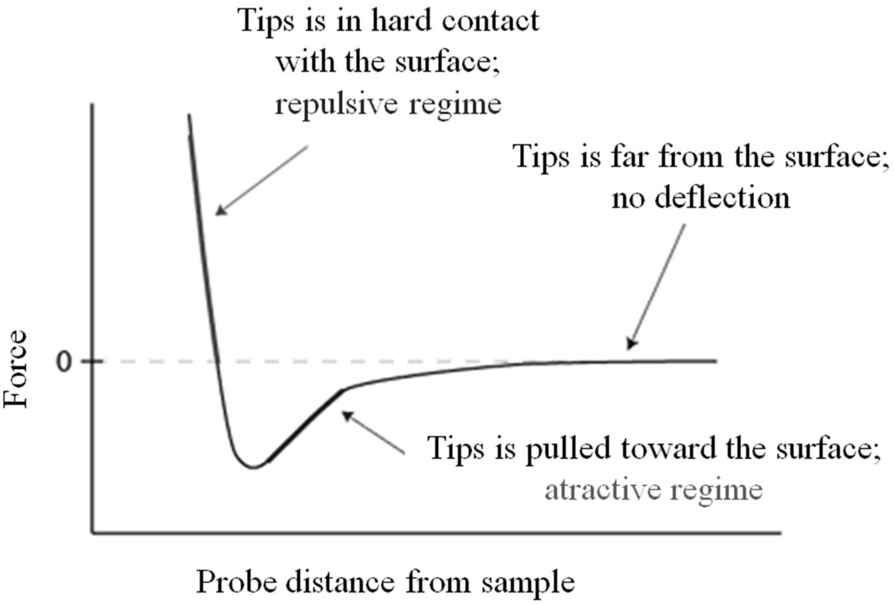

Figure 57: Van der Waals force vs. distance (http://www.nanoscience.com)

The force most commonly associated with atomic force microscopy is an interatomic force called the van der Waals force. The cantilever is held less than a few nanometers from the sample surface in the contact region and the interatomic force between the cantilever and sample is ***repulsive*** (Figure 57).

In the non-contact region, the cantilever is held in the order of 1−10 nm from the sample's surface and the interatomic force between the cantilever and the sample is ***attractive*** (Figure 57).

Interatomic forces between the probe tip and sample surface cause the cantilever to deflect as the sample's surface topography (or other properties) changes. A laser light reflected from the back of the cantilever measures the deflection of the cantilever. This information is fed back to a computer, which generates a topographical map and/or other properties of interest. Area as large as about 100 μm square to less than 100 nm square can be imaged.

X-Ray Diffraction (XRD): X-ray diffraction is a non-destructive technique that gives insight into the crystalline structure of natural and manufactured materials. When the monochromatic X-ray beam with wavelength λ irradiates a crystalline material at an angle θ, it diffracts into many specific directions. Because the crystal lattice is a regular three-dimensional distribution of atoms, the crystallographer can produce a three-dimensional picture of the density of electrons within the crystal, based on the angles and intensities of the diffracted beams.

X-ray diffraction can be explained by the Bragg model of diffraction, Equation 28:

$$n\lambda = 2d\sin\theta \tag{28}$$

where, λ is the wavelength of the X-rays, d the interlattice spacing, θ the incident angle and n an integer. Different crystal planes will have different diffraction angles. Angles are used to calculate the interplanar atomic d-spacings because every crystalline material will give a characteristic diffraction pattern and can act as a unique 'fingerprint'.

The planes are all parallel to each other and intersect the axes of the crystallographic unit cell. Any set of lattice planes can be indexed by an integer triple *hkl*, the so-called Miller indices. The Bragg equation describes the relationship between the lattice vectors and the scattering vector for an x-ray reflection to occur. The Bragg equation may be obtained geometrically as shown in Figure 58.

It should also be obvious that, while atoms on the planes diffract in phase, atoms *between* the planes will diffract out of phase. The phase shift will be proportional to how far the atom is from one plane, as a fraction of the distance to the next plane. So we can see that a single diffraction event tells us about the positions of atoms relative to these sets of planes.

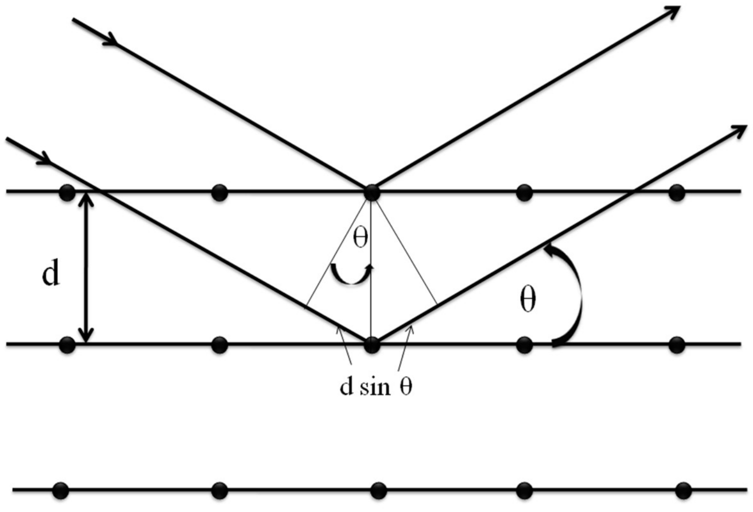

Figure 58: Bragg diffraction explained.

X-Ray Photon Electron Microscopy (XPS): X-ray photoelectron spectroscopy (XPS), also known as electron spectroscopy for chemical analysis (ESCA), is a quantitative spectroscopic technique which is used to determine the elemental composition, empirical formula, chemical state and electronic state of the elements existing within a material. It is a surface analysis technique with a sampling volume that extends from the surface to a depth of approximately 1−10 nm. Alternatively, XPS can be utilized for sputter depth profiling to characterize thin films by quantifying matrix-level elements as a function of depth.

XPS spectra are obtained by irradiating a material with a beam of X-rays. The sample is placed in an ultra high vacuum environment and exposed to a low-energy, monochromatic X-ray source. The incident X-rays cause the ejection of core-level electrons from sample atoms. The energy of a photoemitted core electron is a function of its binding energy and is characteristic of the element from which it was emitted. Energy analysis of the emitted photoelectrons is the primary data used for XPS.

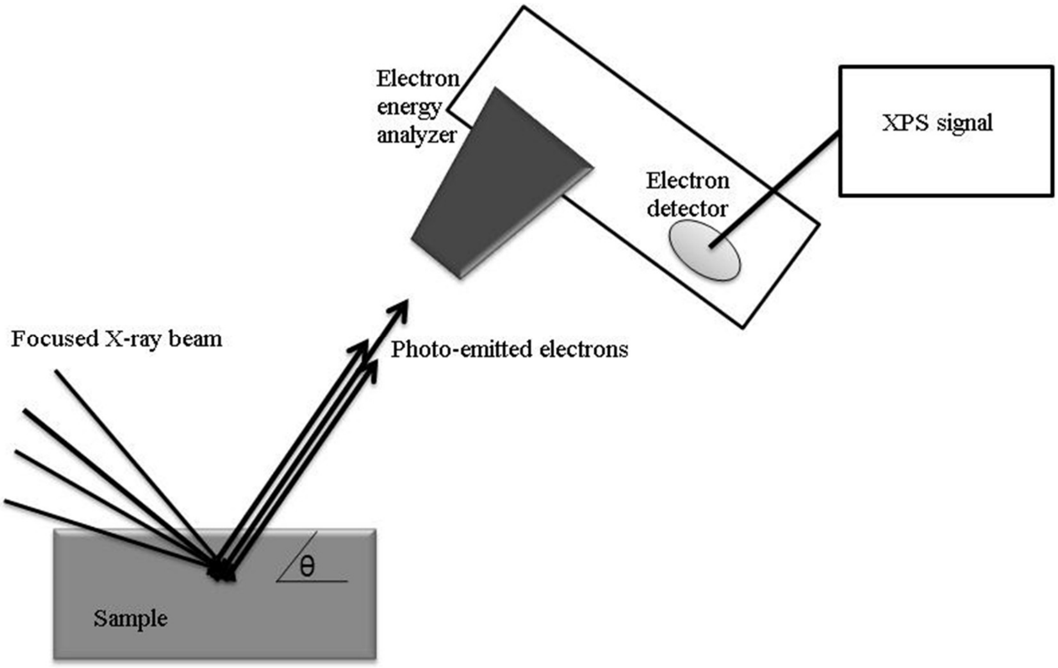

Figure 59: Basic components of a monochromatic XPS system.

Each element produces a characteristic set of XPS peaks at characteristic binding energy values that directly identify each element on the surface of the material. These characteristic peaks correspond to the electron configuration of the electrons within the atoms, e.g., 1s, 2s, 2p, 3s, etc. The number of detected electrons in each of the characteristic peaks is directly related to the amount of element within the area (volume) irradiated. The basic components of an XPS system are shown in Figure 59. In most applications, it is a non-destructive technique that measures the surface chemistry of a material.

Vibrating Sample Magnetometer (VSM): A vibrating sample magnetometer (VSM) is used to measure the magnetic moment of small samples in different applied fields. A vibrating sample magnetometer normally operates over a temperature range of 2 K to 1050 K and enables measurements of magnetic moments as small as $5\text{x}10^{-5}$ emu in magnetic fields from 0 T to 9 T. It works by detecting the voltage induced in a set of pick-up coils by the varying fields associated with the vibrating sample. In a VSM, the sample is fixed to a small holder located at the end of a sample rod attached to a vibration exciter, Figure 60.

The exciter moves the sample up and down at a set frequency, typically 85 Hz, and the sample vibrates along the vertical axis perpendicular to the magnetizing field. The alternating magnetic field will cause an electric field in the pick-up coils. The induction current is proportional to the magnetization of the sample and amplified by a lock-in amplifier. The various components are hooked up to a computer interface. Using controlling and monitoring software, the system can tell us how magnetized the sample is and how dependent its magnetization is on the strength of the constant magnetic field.

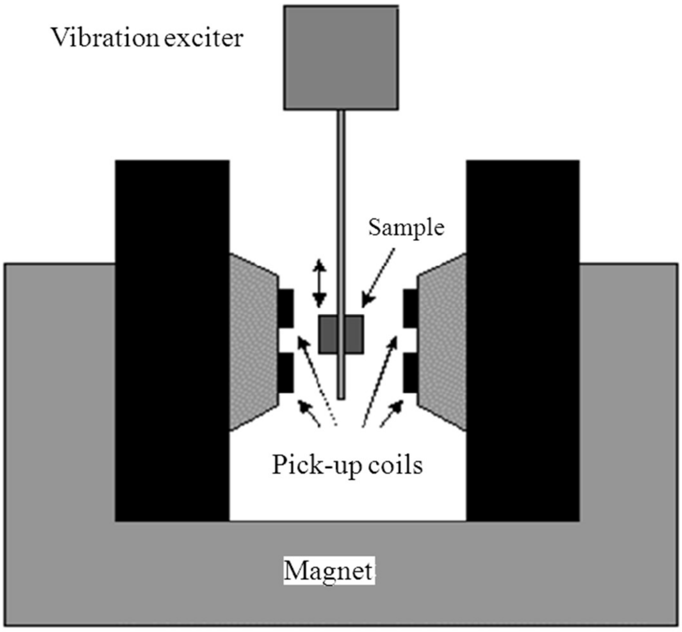

Figure 60: Schematic setup of a vibrating sample magnetometer (VSM).

Superconducting Quantum Interference Device (SQUID): A superconducting quantum interference device (SQUID) is a very sensitive tool for measuring extremely weak magnetic fields, using a device called a Josephson junction. A Josephson junction is made up of two superconductors, separated by a thin non-conducting barrier which electrons can pass through, resulting in a flow of a resistanceless current through the insulator. The flow of current between the superconductors in the absence of an applied voltage is called a *Josephson current*, and the movement of electrons across the barrier is known as *Josephson_tunneling*. If a voltage is applied, the current stops flowing and oscillates at a high frequency, proportional to the voltage.

SQUID (Figure 61) is used to magnetically characterize materials, when the highest detection sensitivity over a broad temperature range is needed. The central element of a SQUID is a ring of superconducting material with one or two Josephson junctions for the RF or the dc SQUID, respectively. Both junctions in the dc SQUID introduce the same phase difference when the magnetic flux (Φ) through the loop is a quantized value (a multiple of the flux quanta), resulting in constructive interference and introducing opposite phase difference when the flux is not an exact multiple of the flux quanta, which leads to destructive interference. This interference causes the critical current (I_C), which is so sensitive to the magnetic flux through the superconducting loop, that even very small magnetic moments can be measured. Commercial SQUIDs transform the modulation in the critical current to a voltage modulation, which is much easier to measure.

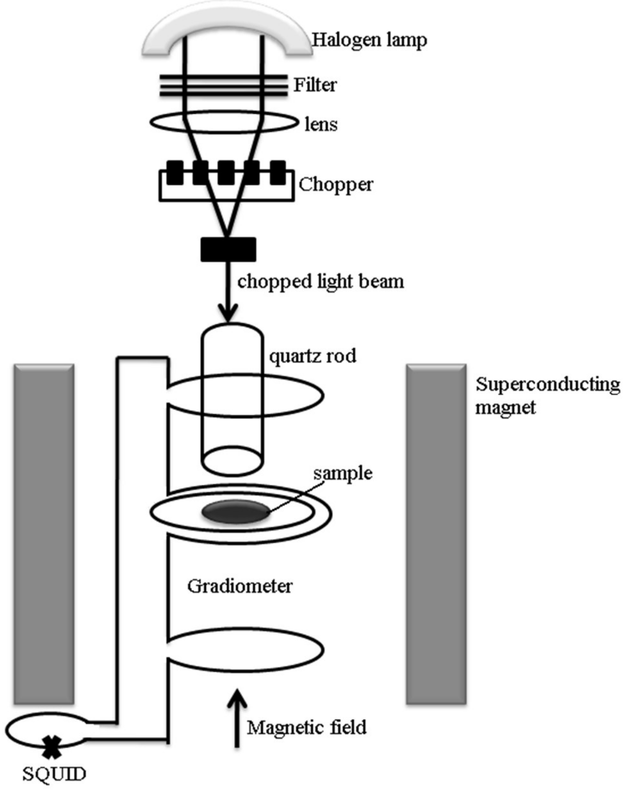

Figure 61: Superconducting quantum interference device - SQUID.

Instrumental Neutron Activation Analysis (INAA): Instrumental neutron activation analysis (INAA) is a highly sensitive method which involves the bombardment of a sample with neutrons to determine its elements and their concentrations. The sample is placed in a nuclear reactor where the neutrons interact with atoms, creating new radioactive isotopes (Figure 62). When these isotopes decay, they emit gamma rays whose energies are characteristic for each isotope and by comparing their intensity with the intensity of the gamma rays emitted by standard materials with known elemental concentrations, it is possible to determine which elements are present in the sample and their concentrations. Sensitivities are sufficient to measure certain elements in the order of parts per billion or better.

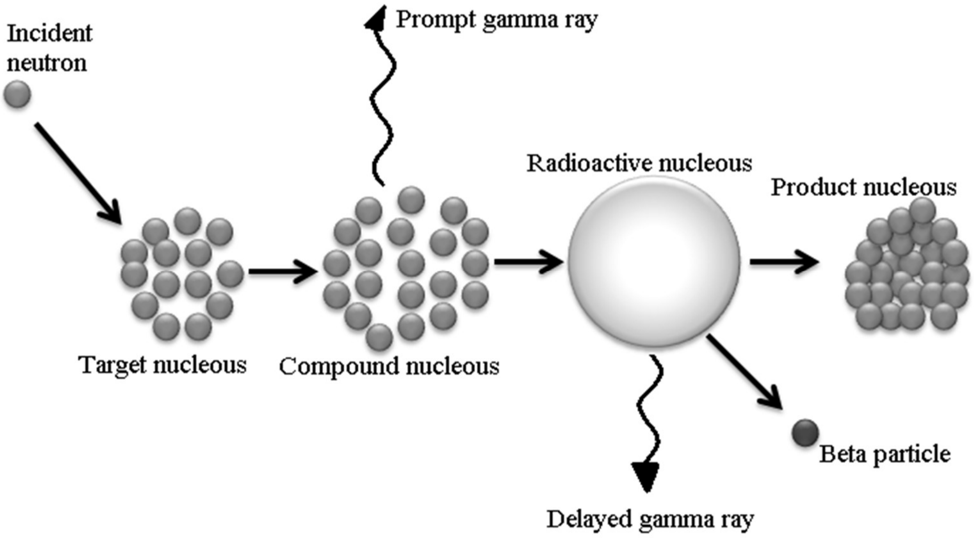

Figure 62: Schematic diagram illustrating neutron capture activation nalysis.

Bibliography

Articles

Azdejković, J. M.; Elteren, J.; Žužek, R. K.; Jaćimović, R.; Sarantopoulou, E.; Kobe, S.; Cefalas, A. C. Dual purpose laser ablation-inductively coupled plasma mass spectrometry for pulsed laser deposition and diagnostics of thin film fabrication: preliminary study. *Talanta* **79**, 583 (2009).

Cefalas, A. C.; Kobe, S.; Sarantopoulou, E.; Samardzija, Z.; Janeva, M.; Dražić, G.; Kollia, Z. Growth, clustering and morphology of intermetallic alloy core-shell nanodroplets. *Physica Status Solidi (a): Applications and Materials Science* **205**, 1465 (2008).

Kobe, S.; Sarantopoulou, E.; Dražić, G.; Kovač, J.; Janeva, M.; Kollia, Z.; Cefalas, A. C. Growth of crystalline/amorphous biphase Sm-Fe-Ta-N magnetic nanodroplets. *Applied Surface Science* **254**, 1027 (2007).

Conferences

Azdejković, J. M.; Elteren, J.; Žužek, R. K.; Jaćimović, R.; Sarantopoulou, E.; Kobe, S.; Cefalas, A. C. Optimization of PLD for Fe-Sm-based thin film fabrication using an analytical laser ablation system interfaced with an inductively coupled plasma mass spectrometer. *Hot nano topics 2008: incorporating SLONANO 2008, 3 overlapping workshops on current hot subjects in nanoscience, 23–30 May, Portorož, Slovenia : abstract book*. 245 (Ljubljana: [s. n.], 2008).

Azdejković, J. M.; Elteren, J. Dual purpose laser ablation ICP-MS for PLD synthesis and elemental analysis to rapidly optimize thin film fabrication. *15th Young Investigators' Seminar on Analytical Chemistry (YISAC), Ljubljana, Slovenia*, July 2–5, 2008. *Book of abstracts*. 111–112 (Ljubljana: Faculty of Chemistry and Chemical Technology, 2008).